QUARTERLY REPORT of RTRI

Feb. 2023 Vol. 64 No. 1

CONTENTS

RAILWAY TECHNICAL RESEARCH INSTITUTE

CONTENTS

Recent Trends in Design Technology for Railway Tunnels and Summary of Revisions in Design Standards for Railway Tunnels

Kazuhide YASHIRO

Tunnel Engineering Laboratory, Structures Technology Division

More than 20 years have passed since the three design standards for railway tunnels were published. In the meantime, design methods for structures other than tunnels have shifted to performance-verification design methods. Since 2014, a committee consisting of academic experts, railway operators has been set up to study the introduction of performance-based design, and as a result, in April 2022, the Ministry of Land, Infrastructure, Transport and Tourism issued the design standards for railway structures as a notification. This outlook commentary introduces trends in tunnel design technology for railways and an overview of new railway tunnel design standards based on performance-verification design methods.

Key words: *tunnel, design standard, performance-verification design method*

1. Introduction

Following the shift of the Ministerial Ordinance to Establish Technical Standards for Railways (Ministry of Land, Infrastructure, Transport and Tourism Ordinance No. 15 [1]) from specifications to performance codes in 2001, design standards for railway structures (henceforth, "design standards") that serve as interpretation standards have also shifted to performance-verification design methods. Since 2014, a committee that consists of academic experts, railway operators, and others, has been established to develop design standards for railway tunnels, and the introduction of a performance-verification design method has been investigated, then, in April 2021, the Railway Bureau of the Ministry of Land, Infrastructure, Transport and Tourism issued a notification to railway operators. In this outlook commentary, we introduce trends in railway design technologies and outline the new design standards for railway tunnels to which the performance-verification design method has been applied.

2. Trends in tunnel design technology

The performance-verification design method is attracting attention as a means of reducing construction costs and improving the degree of design freedom. Generally known advantages include (1) flexible responses to new technologies and individual circumstances are possible; (2) information on performance is disclosed and can be more easily understood by general users since the performance of structures is numerically indicated; and (3) evaluating performance not only during construction but also afterwards allow for applications to the evaluation of lifecycle costs. However, in addition to these advantages, there is also the benefit of contributing to the design of safer and longer-lasting structures by numerically or empirically directly examining performance items that correspond to the deformation or deterioration occurring in structures (e.g., subsidence → stability, material deterioration → durability, convergence → space retention).

Figure 1 shows the shift of design standards to the performance-verification design method. The standards for bridges were completed with the shift to steel-concrete hybrid structures standards in FY2017, and the standards for the ground structures were completed with the shift to the foundation and earth retaining structures standards in FY2012. Meanwhile, standards relating to tunnels include the following publications: for cut and cover tunnels, the Design Standards for Railway Structures and Commentary (Cut and

Cover Tunnel) (henceforth, "Cut and Cover Tunnel Standards"); for shield tunnels, Design Standards for Railway Structures and Commentary (Shield Tunnel) (henceforth, "Shield Tunnel Standards"); and for mountain tunnels, and specifically urban mountain tunnels, the Design Standards for Railway Structures and Commentary (Urban Mountain Tunnel) (henceforth, "Urban Mountain Tunnels Standards"). However, over 20 years have passed since even the most recently published Cut and Cover Tunnel Standards was published, and there is an urgent need for shifts.

Given this background, we decided to start by revising the Cut and Cover Tunnel Standards, which, of the three tunnel construction methods, was thought to be relatively easy to shift. In January 2014, we therefore established the Committee on the Design Standards for Railway Structures (Cut and Cover Tunnel) (committee chair: Yukinori Koyama, Visiting Professor at Ritsumeikan University). Afterwards, in January 2016, we established the Committee on the Design Standards for Railway Structures (Shield Tunnel) (committee chair: Hirokazu Akaki, Professor at Waseda University) and the Committee on the Design Standards for Railway Structures (Mountain Tunnel) (committee chair: Toshihiro Asakura, Emeritus Professor at Kyoto University). After three years of deliberation by each committee, each final committee had written a revised draft.
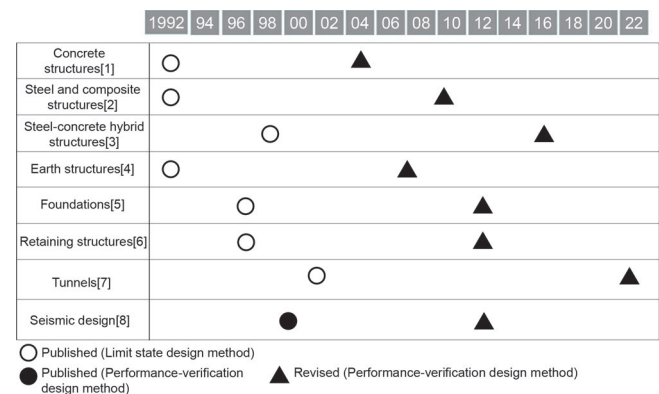

Fig. 1 Shift of design standards to performance-verification design method

3. Overview of new design standards

Figure 2 shows the railway tunnels that are covered by the newly enacted Design Standards for Railway Structures and Commentary (Tunnels) (henceforth, "Tunnel Standards"). Railway tunnels are railway structures covered by the Ministerial Ordinance to Establish Technical Standards for Railways that are underground structures through which trains run, as shown in Fig. 2(a), and these include tunnels between stations and underground stations as well as vertical shafts that are integrated with tunnels. Meanwhile, underground structures that support trains on the ground but do not allow trains to run inside, as shown in Fig. 2(b), are not included in this definition of railway tunnels. However, since trains that run on the ground need to do so safely while ensuring ride comfort, the Tunnel Standards can be applied with necessary changes.

As shown in Fig. 3, the Tunnel Standards consists of four volumes: Volume I defines the basic principles for surveys, structural plans, and performance verifications that cover all railway tunnels, regardless of construction methods or shape; and Volumes II-IV show standard methods among the specific methods that satisfy Volume I. The structure of the design standards as a booklet is such that the three representative construction methods are composed of Volume I and the corresponding Volumes II-IV, as shown in Fig. 3, in order to provide a user-friendly product.

Design standards for railway civil engineering structures include concrete structure standards, steel and composite standards, and steel-concrete hybrid standards. Figure 4 shows the relationship between the Tunnel Standards and other design standards, using the concrete structure standards, steel and composite standards, and steel-concrete hybrid standards as examples. These design standards describe all levels (material level, member level, structure level). However, for the Tunnel Standards, we describe items specific to tunnels (verification items, combinations of actions, calculation of response values) for the structure level, and we do not describe the same items as the standard we are citing and instead refer to related standards for the material level and member level. Similarly, we based the surveys and ground on the foundation standards, and the impact of earthquakes and verifications during earthquakes on the seismic design standards. This was done in order to avoid inconsistencies when the relevant design standards were revised.

The performance requirements for railway structures and the performance items for railway tunnels that are determined based on these must be the same for each railway line, regardless of not only the structure type but also the structural type and construction method. Table 1 shows examples of the required performance, performance items, and verification indices. It is important to maintain the inner space in railway tunnels, and the verification indices used are the displacement / deformation of the inner space for running safety, and water leakage for watertightness.

As with other design methods, the performance verification involves setting a limit state that is equivalent to the performance requirements and performance items, verifies that the railway tunnel has not reached the limit state, and generally confirm that Eq. (1) is satisfied.

$$\gamma_i \cdot I_{Rd}/I_{Ld} \leqq 1.0 \qquad (1)$$

I_{Rd}: design response value, I_{Ld}: design limit value, γ_i: structural coefficient

When using pre-verified designs, or when the assumptions are well-defined, then confirming these assumptions can result in the performance items can be deemed satisfied, and the specific handling of these performance items is shown in Volumes II-IV. Table 2 shows the table of contents for each volume.

(a) Railway tunnels   (b) Non-railway tunnel
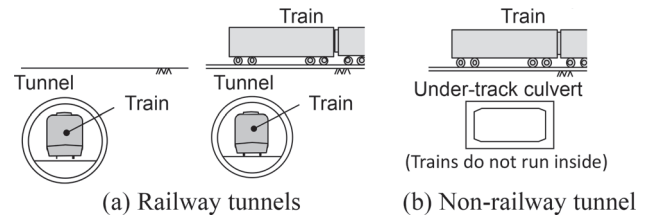
Fig. 2 Target railway tunnels
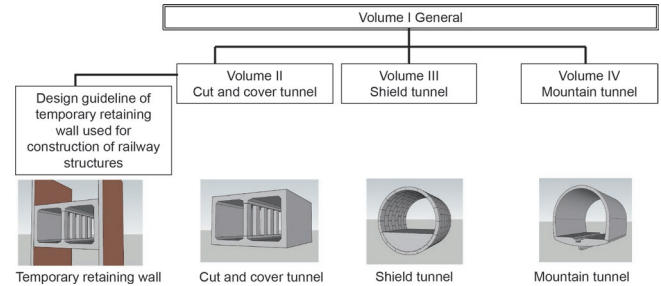
Fig. 3 Compositions of Tunnel Standards volumes
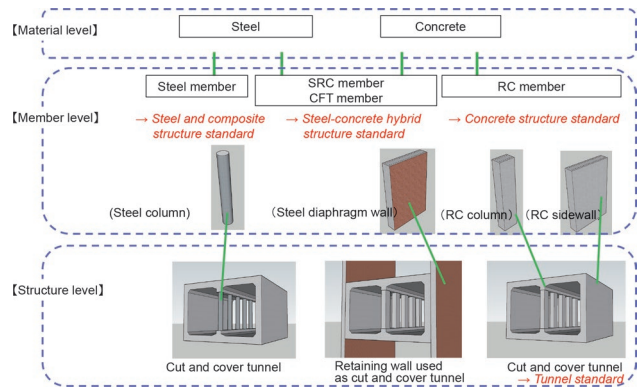
Fig. 4 Relationship between Tunnel Standards and other design standards

Table 1 Examples of performance requirements and performance items / verification indices

Required Performance	Performance Item		Verification Indices
Safety	Failure		Force, displacement/deformation
	Fatigue failure		Force, stress intensity, number of repeats
	Stability		Force, displacement/deformation
	Running safety		Displacement/deformation
	Public safety		Displacement/deformation
Serviceability	Aesthetic appearance		Crack width, stress
	Watertightness		Crack width, stress intensity
	Bearing capacity		Force, displacement/deformation
	Riding comfort		Displacement/Deformation
	Noises/vibration		Noise level, vibration level
Restorability	Damage	Member	Displacement/deformation, force, stress intensity
		Track	Displacement/Deformation
	Residual displacement		Force, displacement/deformation

4. Summary of revisions of Cut and cover tunnel [9]

As shown in Fig. 3, the booklet of design standards for the cut

Table 2 Table of contents of each volume

Volume I Tunnel general	Volume II Cut and cover tunnel	Volume II Cut and cover tunnel	Volume III Mountain tunnel

Chap.1 General principles
Chap.2 Basis of design
Chap.3 Structural plan
Chap.4 Required performance
    and performance verification
	Chap.1 General principles
	Chap.2 Basis of design
	Chap.3 Structural plan
	Chap.4 Required performance
	    and performance verification
		Chap.1 General principles
		Chap.2 Basis of design
		Chap.3 Structural plan
		Chap.4 Required performance
		    and performance verification
			Chap.1 General principles
			Chap.2 Basis of design
			Chap.3 Structural plan
			Chap.4 Consideration
			    on ground stability
			Chap.5 Required performance
			    and performance verification

	Chap.5 Action
	Chap.6 Material and ground
	Chap.7 Performance verification
	    of cut and cover tunnel
	Chap.8 Performance verification
	    of cut and cover tunnel
	    using earth retaining wall
	    as main structure
	Chap.9 Performance verification
	    of shaft
	Chap.10 Cut-and-cover tunnel
	    with special design
	    conditions
		Chap.5 Action
		Chap.6 Material and ground
		Chap.7 Performance verification
		    of shield tunnel
		Chap.8 Shield tunnel
		    with special design
		    conditions
		Chap.9 Structural details and
		    production of segments
			Chap.6 Action
			Chap.7 Material and ground
			Chap.8 Performance verification
			    of lining and invert
			Chap.9 Performance verification
			    of portal
			Chap.10 Mountain tunnel
			    with special design
			    conditions

and cover tunnel after revisions (Design Standards for Railway Structures and Commentary (Tunnel / Cut and Cover Volume)) consists of Volumes I and II. The Tunnel Standards / Cut and Cover Volume includes excavation earth retaining work design guidelines used in the construction of railway structures.

As previously mentioned, a pillar of the revisions was the introduction of the performance-verification design method into the design of the cut and cover tunnel body in order to enable a more flexible design; and with regards to the specific handling of each performance item as well as the calculation of specific response values and setting of limit values, we enhanced methods that could consider construction and environmental conditions that are specific to cut and cover tunnels as well as methods that can respond to various structural and ground conditions.

Below, the outline of the revision of the cut and cover tunnel is introduced.

4.1 Enhancement of descriptions based on maintenance

The design bending crack width and design cover of the reinforced concrete members can be set according to other design methods, and specific setting methods are illustrated based on case analysis.

For example, bending cracks in cut and cover tunnels are affected not only by concrete shrinkage and creep but also by fluctuations in earth and water pressure during service. As previously mentioned, these effects are calculated according to the concrete structure standards after considering the construction conditions and underground environment of the cut and cover tunnel; simultaneously, it was decided that the factor $k4$, which takes into consideration the variation in the width of bending cracks, may be considered. The cover of reinforced concrete members was also set according to the concrete structure standards except for the case of direct casting into the soil.

Regarding chloride ions that cause steel corrosion, in the case of cut and cover tunnels, when excluding the impact of initially contained chloride ions during construction, then the chloride ions in the groundwater are thought to be the main cause. Therefore, we reference the German standards for evaluating the concentration of water components (Deutsches Institut für Normung (DIN)) and the water quality standards for tap water, if the chloride ion concentration in the groundwater at the construction site is 200 mg/L or less, then we generally decided to omit its investigation. From the survey results of the actual structure and the seepage flow analysis results, it was shown that the area within 100 m from the landfill or tidal river was assumed to be the place where the chloride ion concentration of the
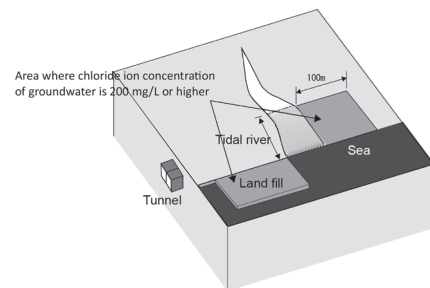
Fig. 5 Range where high chloride ion concentration was confirmed in water leakage investigation
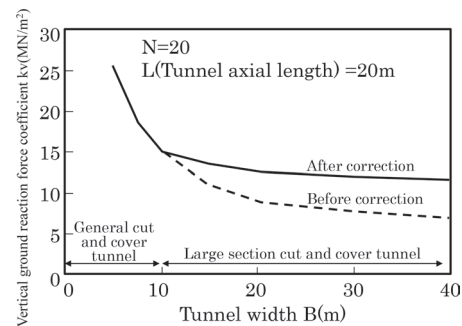
Fig. 6 Example of ground reaction force coefficient [11]

groundwater was 200 mg/L or more (Fig. 5) [10]. In such places, we set as acceptable the consideration of other countermeasures such as using epoxy resin-coated reinforcing bars as necessary.

4.2 Reconsideration of calculation method for response values in large-scale underground train stations

Cut and cover tunnel design generally involves modeling the ground using springs, but calculation of the ground reaction force coefficient considers the loading width dependency, with a larger loading width decreasing the coefficient. Large-scale underground train stations have been increasing in recent years, and the ground reaction force coefficient that is calculated in these cases becomes smaller. Here, the actual ground tends to have a smaller ground reaction force coefficient as the displacement level increases. However, considering that the weight of the tunnel members is smaller than the weight of the excavated soil in a general cut and cover tunnel, and that the stiffness of the member is ensured according to the di-

Fig. 7　Concept of quasi-integrated analysis [12]

Fig. 8　Soil-cement type steel continuous underground wall [10]

Fig. 9　Two-ring beam spring model

Fig. 10　General action in shield tunnel design

Table 3　Comparison of lateral earth pressure coefficient (λ)

Type of soil		Approx. N value	Before revision		After revision	
			λ	Soil and water	λ	Soil and water
Sandy soil	Extremely dense	30≦N	0.45	Separated	0.45	Separated
	Dense	15≦N<30	0.45～0.50		0.45～0.50	
	Moderate, loose	N<15	0.50～0.60		0.50～0.60	
Cohesive soil	Consolidated	25≦N	—	—	0.45	Separated
	Hard	8≦N<25	0.40～0.50	Combined	0.45～0.50	
	Moderate	4≦N<8	0.50～0.60		0.50～0.60	
	Soft	2≦N<4	0.60～0.70		0.60～0.65	Combined
	Extremely soft	N<2	0.70～0.80		0.65～0.70	
					0.70	

Red numbers: Changes

mensions of the tunnel, we decided to introduce the ground correction coefficient ρ_{gk} and correct the ground reaction force coefficient in large-section cut and cover tunnels with a width exceeding the general cut and cover tunnel width of 10 m in order to avoid underestimating the ground reaction force coefficient when the displacement level is small. Figure 6 shows an example of the correction.

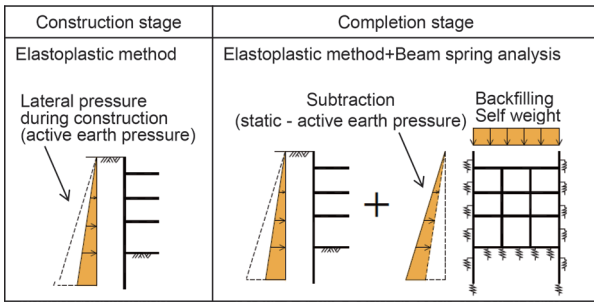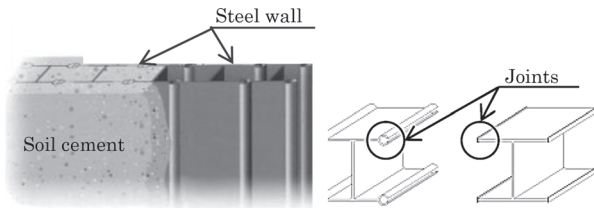**4.3　Performance verification method when using continuous underground wall as main structure**

In the design of cut and cover tunnels that use a continuous underground wall as the main structure, there are many examples of the application of a separate calculation method where the design during construction and design of the main structure are conducted separately. However, considering the fact that the main structure is constructed as a structure while receiving the stress during construction, it is difficult to say that this calculation method is necessarily the method that corresponds to actual circumstances. Meanwhile, the integrated calculation method, which is a method of conducting a series of analyses from construction to completion, can consider the construction process but has disadvantages like a complicated calculation and the need for calculations according to the construction procedure. Therefore, we made it possible so that a quasi-integrated analysis (Fig. 7) can be applied, where the residual stress during construction can be considered, calculation results that are close to the integrated calculation method are obtained, and where the calculations do not become too complicated [12]. At the same time, a specific and standard method of performance verification was presented for the soil-cement type continuous underground steel wall (Fig. 8), which has recently been adopted in railways.

5.　Summary of revisions of shield tunnel

The booklet of design standards for the shield tunnel after revisions (Design Standards for Railway Structures and Commentary (Tunnel / Shield volume)) consists of Volumes I and III, as shown in Fig. 3.

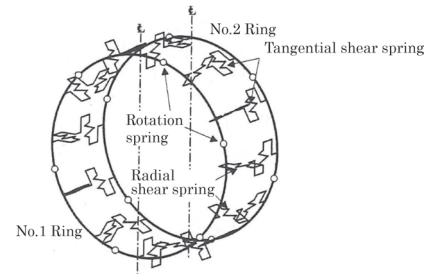Currently, the design of the shield tunnel is conducted by the shield tunnel standards established in 1997. The shield tunnel standards introduced a beam-spring model (Fig. 9) in which the segments, circumferential joints, axial joints, and ground are modeled with a beam, rotational spring, shear spring, and ground spring. The bilinear model and trilinear model have been proposed for the rotational spring characteristics of circumferential joints (the relationship between joint rotation angle and moment); and methods for calculating the joint spring properties using structural models, finite element method, and joint bending tests are presented. In addition, the concept of the calculation of the action of earth and water pressure, ground reaction force coefficient, etc., was also determined according to the full-circumference spring model.

Here, when introducing the performance-verification design method to the design of the shield tunnel, we decided to inherit aspects from the shield tunnel standards for the above-mentioned structural model and conducted additional investigations that are needed for the introduction of the performance-verification design method. Regarding the specific handling of each performance item as well as the calculation of specific response values and the setting of limit values, we considered the construction and environmental conditions that are unique to shield tunnels and enhanced the descriptions of methods that can deal with various structural and ground conditions. Below, we introduce a summary of the revisions of the shield tunnel.

5.1　Reconsideration of lateral earth pressure coefficient

The design of shield tunnels considers the actions of vertical earth pressure (loosening earth pressure / total earth pressure, etc.), lateral earth pressure, water pressure, etc. (Fig. 10). Here, the lateral

Fig. 11 Example of ground reaction coefficient correction [13]

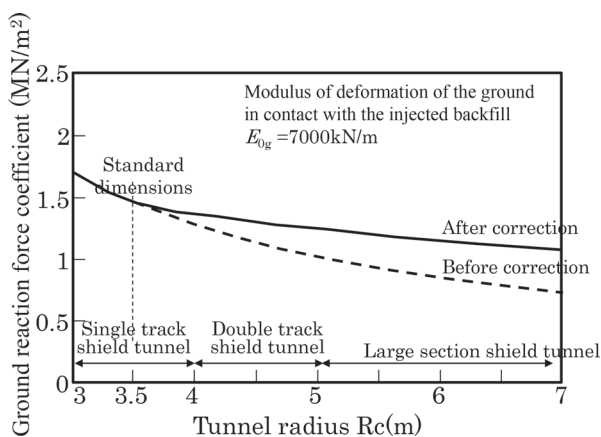earth pressure is obtained by multiplying the vertical earth pressure by the lateral earth pressure coefficient λ, which is determined by the N value of the ground. However, the lateral earth pressure coefficient was partially reconsidered based on past design examples and construction results. Furthermore, no guidelines for the lateral earth pressure coefficient have been presented to date in the case of hard and good cohesive soil, but a new guideline (Table 3) was presented this time so that the lateral earth pressure can be set appropriately. This is expected to lead to the optimization of the lining design.

5.2 Reconsideration of calculation method for response value in large-section tunnel

In shield tunnel design, the interaction between the ground and tunnel is modeled using ground springs. The radial ground reaction force coefficient in the shield tunnel is calculated using the Muir Wood theoretical equation, which sets the coefficient as inversely proportional to the radius of the tunnel after considering the deformation characteristics of the two-layer system of backfilling and the surrounding ground with different deformation coefficients. In recent years, the number of large-section shield tunnels has been increasing, and the calculated ground reaction force coefficient becomes smaller in these cases. Meanwhile, the presence of linings is thought to suppress deformation even in large-section shield tunnels. Therefore, we introduced a ground correction coefficient ρ_{gk} and corrected the ground reaction force coefficient for large-section shield tunnels exceeding the general shield tunnel width of 10 m (radius of 5 m) in order to avoid underestimating the ground reaction force coefficient when the displacement level is small. Figure 11 shows an example of the correction. We expect that the response value will be optimized by correcting the ground reaction force coefficient, and the scope of the RC segment will be expanded.

6. Summary of revisions of mountain tunnel

The booklet of design standards for the mountain tunnel after revisions (Design Standards for Railway Structures and Commentary (Tunnel / Mountain volume)) consists of Volumes I and IV, as shown in Fig. 3. Below, we introduce a summary of revisions of the mountain tunnel.

6.1 Expanding scope of design standards

Currently, the design of mountain tunnel linings and inverts is conducted according to the mountain tunnel standards that were established in March 2002 only for tunnels constructed in urban areas.

Tunnels in urban areas are often constructed in unconsolidated or low-consolidation sediment ground with relatively small overburden, and construction work near the tunnel may have an impact. Considering these factors, the lining and inverts are to be designed as waterproof RC structures.

Meanwhile, mountain tunnels do not have any design standards; and tunnel linings and inverts, with the exception of tunnel sections nearby portals where design calculations are conducted as RC structures or cases of special ground where this cannot be applied, involve the application of a standard design that is a predetermined specification.

A railway system is a linear system composed of various types of structures, and it is thought that the performance of structures should be specified in a quantitative manner, and that the standards for evaluating performance should be the same. In this revision, mountain tunnels were also included in the scope of Design Standards for Railway Structures and Commentary (Tunnel) Volume IV.

Currently, most mountain tunnels are constructed by NATM. NATM is characterized by the use of steel supports, shotcrete, and rock bolts; and the construction of tunnels by actively utilizing the support ability of the ground. Excavation methods and support work are essential for the stability of the tunnel, but at the same time, it is difficult to directly verify the ground, and there are currently no methods for setting performance items and limit values for support work that contribute to the stability of the ground, nor are there any methods to verify them. In practice, we verified excavation methods and support work based on proven specifications, and observation and measurements during excavation and support work confirmed that (1) deformation was mostly settled, and (2) the support work was not severely fractured, and (3) excessive deformation did not occur, these confirmations ensured safety. Therefore, in the tunnel standards / Mountain Volume, the stability of the natural ground was treated as a premise of the lining and invert inspection, and the excavation method and support work specifications were presented as construction conditions. Furthermore, the premise for lining and invert verification was deemed satisfied by confirming the above-mentioned items (1), (2) and (3) through observation and measurement. In response, as shown in Table 2, Volume IV adds a verification on ground stability in Chapter 4, which was not included in Volume II or III.

6.2 Establishment of pre-verified specifications [14]

Figure 12 shows the lining and invert structures and design methods for different ground conditions. It is thought that these can be broadly divided into three categories: condition 1, cases where external forces other than the dead weight are assumed; condition 2, cases where it is assumed that displacement from the ground will occur after completion; and condition 3, cases other than the above. Specific examples of each condition include the following: condition 1, portal, small overburden (including urban areas); condition 2, squeezing ground; and condition 3, sufficiently stable ground after entering the portal and where there is less impact by weathered surface layers.

In condition 1, it is thought that the RC structure can be designed based on the performance verification by conducting frame analysis that applies loosening earth pressure, total earth pressure, etc. In condition 2, it is thought that performance verification can be conducted using methods shown in Reference [15], for example, in cases where ground displacement is expected after completion. In condition 3, it is thought that confirming the absence of problems with the dead weight of the plain concrete was sufficient, but since many sections of rail-
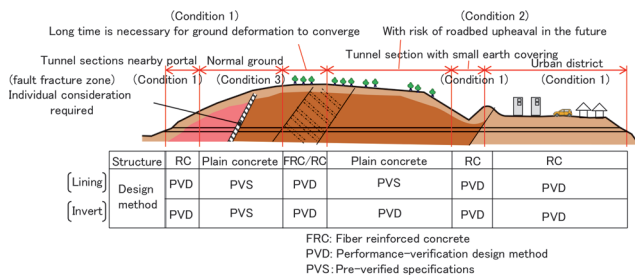
Fig. 12 Classification of lining and invert design methods

way mountain tunnels are thought to fall under condition 3, it was thought that it was simpler to define these as "pre-verified specifications," and to make the design using these specifications.

The standard design of linings and inverts is used in most sections of mountain tunnels of the current Shinkansen tunnels that fall under condition 3. Considering this point and also to be consistent with previous designs, the standard design was established as pre-verified specifications. The lining pre-verified specifications can be applied in the previously mentioned case of condition 3. Additionally, construction of the lining after the settling of the natural ground deformation is a prerequisite for its application. The invert pre-verified specifications can be applied in cases where, in addition to the above-mentioned items, when there is no risk of track surface upheaval or track surface subsidence. Details on the pre-verified specifications are given in Reference [14].

6.3 Miscellaneous

Mountain tunnels are generally thought to be less affected by earthquakes, but this impact should be taken into account if it affects tunnels after completion, such tunnel sections as nearby tunnel portal. To that end, conditions that are susceptible to earthquake impacts were shown, and seismic design methods were described in Chapter 10, "Mountain tunnels with special design conditions." Surface fault displacement and fault fracture zones are separately considered in structural planning.

7. Conclusions

In this outlook summary, we introduced trends in railway tunnel design technology and outlined new design standards for railway tunnels. We hope that these new design standards will promote the introduction of new technologies and result in the construction of durable tunnels that are also easy to maintain.

Acknowledgement

References

[1] *Design Standards for Railway Structures and Commentary (Concrete Structures),* Maruzen, 2004.

[2] *Design Standards for Railway Structures and Commentary (Steel and Composite Structures),* Maruzen, 2009.

[3] *Design Standards for Railway Structures and Commentary (Steel-Concrete Hybrid Structures),* Maruzen, 2016.

[4] *Design Standards for Railway Structures and Commentary (Earth Structures),* Maruzen, 2007.

[5] *Design Standards for Railway Structures and Commentary (Retaining Structures),* Maruzen, 2012.

[6] *Design Standards for Railway Structures and Commentary (Foundations),* Maruzen, 2012.

[7] *Design Standards for Railway Structures and Commentary (Cut and Cover Tunnels),* Maruzen, 2021.

[8] *Design Standards for Railway Structures and Commentary (Seismic Design*), Maruzen, 2012.

[9] Okano, N., Koda, M., "Recent Trends of Design Technology of Cut and Cover Tunnel for Railway," *RTRI Report,* Vol. 33, No. 4, pp. 1-4, 2019.

[10] Ushida, T., Nihei, T., Nakayama, T., "Durability Design Method of Cut and Cover Tunnels Based on the Field Data," *RTRI Report,* Vol. 33, No. 4, pp. 5-10, 2019.

[11] Nakayama, T., Nishiyama, K., Kobayashi, K., Nishioka, H., "Structural Analysis Method of Cut and Cover Tunnels under Special Design Conditions," *RTRI Report,* Vol. 33, No. 4, pp. 23-28, 2019.

[12] Nakajima, T., Kobayashi, K., Toda, K., Kojima, K., "Simple Analysis Method of Considering Construction Process at the Time of the Design of Cut and Cover Tunnels with Diaphragm Walls," *RTRI Report,* Vol. 33, No. 4, pp. 17-22, 2019.

[13] Tsuno, K., Nakayama, T., Fujita, K., Funakoshi, K., Kinoshita, K., "Examination of Ground Reaction Force Coefficient in Large Section Shield Tunnel," presented at the *2018 Japan Society of Civil Engineers National Convention,* Kyoto, Japan, Sept. 12-16, 2018. III-569.

[14] Shimamoto, K., Kawagoe, K., Yashiro, K., Hikari, U., "Proposal of Pre-verified Specification for Mountain Tunnel Lining and Invert," *RTRI Report,* Vol. 36, No. 5, pp. 21-27, 2022.

[15] Shimamoto, K., Yashiro, K., Okano, N., "Performance Verification Design Method of Plain Concrete Lining and Invert Assuming Ground Displacement after Completion," *RTRI Report,* Vol. 36, No. 5, pp. 29-35, 2022.

Author

Kazuhide YASHIRO, Dr. Eng.
Senior Chief Researcher, Head of Tunnel Engineering Laboratory, Structure Technology Division
Research Areas: Mountain Tunnel

Recent Research and Development on Disaster Prevention Technology

Osamu NUNOKAWA

Disaster Prevention Technology Division

This paper provides an overview of the impact of climate change on Japan's weather and introduces some of the research being conducted by RTRI in this regard. In line with our research plan "RE-SEARCH2025," we are working on developing the following areas of research: a high precision operation control system applying observation data, and an evaluation method for the stability of slopes after heavy rain. We will develop technologies to improve the resilience of railways against disasters using a variety of types of digital information.

Key words: *severe disaster, real-time hazard map, operation control, early recovery*

1. Introduction

From August 2021, the three working groups of the Intergovernmental Panel on Climate Change (IPCC) began to publish their Sixth Assessment Report [1], which summarized its latest findings. The latest published report by Working Group I (The Physical Science Basis) predicts even more severe conditions than in the past as a "possible future climate." Such global climate change will directly affect railways by increasing the risk of intense heavy rain and strong winds, so developing technologies to prepare for increasingly severe weather disasters is an urgent issue. Therefore, in this report, we first provide a broad overview of climate change in Japan, then introduce an overview of the research and development that the Railway Technical Research Institute (RTRI) is conducting in this context, before providing an outlook for future disaster prevention technologies.

2. Impact of climate change in Japan

The recently published IPCC Sixth Assessment Report (December 2021) is a report on the physical scientific basis for climate change compiled by Working Group I. This report presents various findings regarding the current climate and possible future climates based on the results of analyzing past meteorological data. It is stated in this report that future climates will involve an increase in the frequency and intensity of heavy rainfall and an increase in the proportion of strong tropical cyclones, which will expand in direct relation with progressive global warming.

Figure 1 shows the data related to this description. This figure shows changes in the number of short-term heavy rainfall events of at least 80 mm per hour as observed by the Japan Meteorological Agency at approximately 1,300 AMeDAS stations across Japan from 1976 to 2021 [2]. As shown in the figure, there is a clear increase in short-term heavy rainfall events, and this trend supports the above-mentioned IPCC report.

Figure 2 shows a graph that summarizes the changes in typhoon strength over time based on the best-track data of typhoons that were published by the Tokyo Center of the Regional Special Meteorological Center (RSMC) (finalized values of observation data that underwent examination and scrutiny after the fact). The top graph shows the changes in the average minimum atmospheric pressure of typhoons that occur each year, and the bottom graph shows the changes in the percentage of typhoons with a maximum wind speed of at least 100 knot (= 51.44 m/s) among the number of typhoons

that occur each year. Both have an increasing tendency, albeit slightly, while repeatedly fluctuating. These data do not clearly show a tendency of "increased percentages of strong tropical cyclones." Meanwhile, when considering the magnitude of damage caused by strong typhoons, like Typhoon Hagibis in 2019, we cannot drop our guard against strong tropical cyclones.
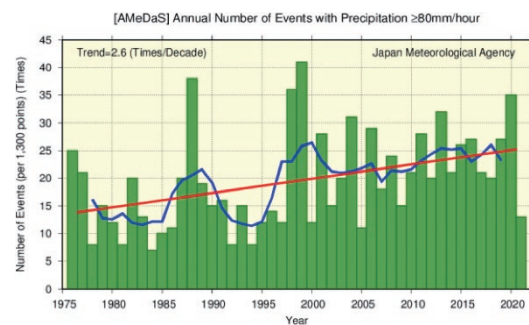
Fig. 1   Changes in the number of rainfall events with at least 80 mm per hour [2]
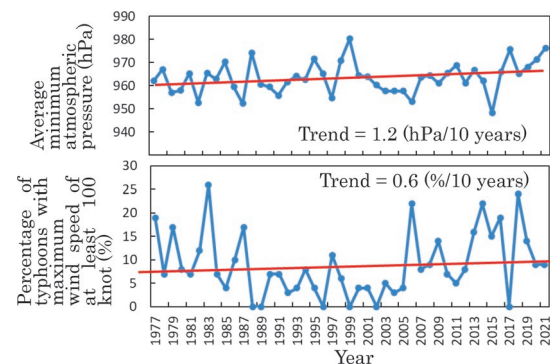
Fig. 2   (Top) average minimum atmospheric pressures of typhoons that occurred in each year and (bottom) percentage of typhoons with maximum wind speed of at least 100 knot

3. Technology development relating to disaster prevention

We describe research issues that should be addressed as disaster prevention technologies, assuming the intensification of weather as shown in the previous section.

The number of planned train operation suspensions have increased in recent years in anticipation of large-scale damage in order to avoid confusion from unplanned last-minute suspensions. Planned suspensions are thought to be highly effective in order to prevent excessive disruption, particularly when major rain or snow events are expected in metropolitan areas. Meanwhile, these suspensions do impact transportation stability, so making sound decisions is essential to avoid excessive suspensions and to know when to end the suspensions.

Additionally, a common factor of severe weather events is disaster-like conditions over a wide-area. Figure 3 shows the points where maximum values have been observed and updated with the heavy rains which fell in July 2018, as well as the JR Line areas that were affected by these heavy rains along with the date. If there is an unprecedented heavy rain event over a wide area, as in this case of severe weather, then there is the possibility that many disasters occur over a wide area in a short period of time. In such cases, even getting a grasp of the situation takes a long time. Furthermore, due to the high-alert situation, the number of personnel able to implement necessary measures is limited, and determining the response for each weather-damaged area may require even more time. Therefore, it is critical to obtain sufficient information for multiple disaster sites spread over a wide area in a short period of time as well as rapidly determine measures that are suited for each disaster situation.
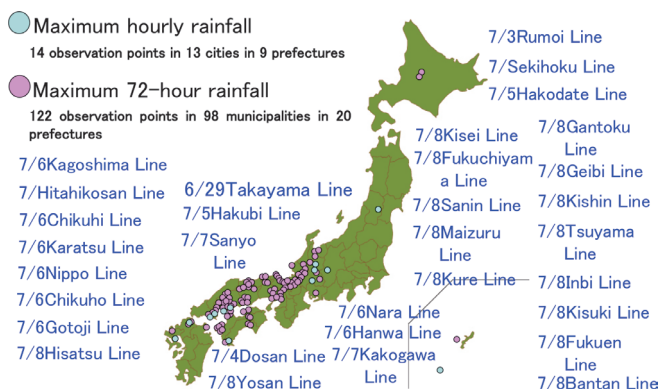

Fig. 3 Distribution of points where maximum values were observed and updated with the heavy rains of July 2018, along with affected JR Lines

Another major problem faced not only by railways, but also Japan as a whole, is the shrinking labor force due to declining birth-rates and the aging of social infrastructure. When considering the impacts of these problems only from the perspective of railway disaster prevention, this raises issues not only about emergency responses in the event of disasters but also the increased efficiency of inspections during normal times. One major question which arises when addressing this issue is how to efficiently advance maintenance and replacement: it is thought that there is a major need for technical development of maintenance that contributes to disaster prevention.

We believe that the introduction of digital technologies is essential in order to solve the above issues, and how each type of information is used will be key.

4. Efforts for resolving issues

4.1 Sophistication of operation control the case of rainfall

RTRI's basic plan RESEARCH2025, which began in FY2020, aims to develop more sophisticated technologies for operation control in the case of heavy rainfall and severe wind events as a way of preparing for severe weather events. Both these technologies seek to ensure safety and reduce downtime by utilizing existing sensing data in real-time as operating information for trains.

In the case of operational management in case of rainfall, advanced methods are being developed that reflect changes slope stability due to rainfall after taking into account terrain and geology. This method involves using numerical terrain information and geological information in order to sequentially calculate changes in water content in the ground due to rainfall to obtain slope stability [3]. There are limitations on computational resources in implementing sequential computations of stability for the large number of slopes along a single railway line. Practical use requires narrowing down the items to be monitored for changes in stability along the railway line, and calculating stability in selected locations. Therefore, we are developing a method for selecting places where safety should be monitored during rainfall along railway lines using numerical terrain information. Figure 4 shows an example of the visualization of a catchment range using the method under development. We are working on the development of a method for selecting locations to be monitored by understanding which parts of the track are affected by the catchment range of the slopes along the track and adding information on slopes and track facilities to such information. We believe that sequentially evaluating the stability of slopes for locations that are selected with this method will lead to higher accuracy in operation control in case of rainfall.
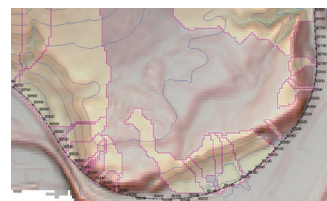
Fig. 4 Selection of evaluation target points by topographical analysis (visualization of catchment range is shown in pale yellow)

4.2 Sophistication of operation control in the case of strong winds

Regarding operation control under strong winds, we are developing methods to regulate operations that sequentially evaluate high-density two-dimensional wind speed distributions and use this information to replace operation control based on anemometers installed in a discrete manner along railway lines. As we develop these methods, we are working on creating a system that conducts weather analysis considering topographical information and building information along the railway line, analyzes the weather data measured at observation points along the railway line in real time, interpolates the wind speeds between observation points, and shows the wind speed distributions on a map like that in Fig. 5. Furthermore, we are working on creating a system that collects and analyzes previous high wind disaster data, associates the wind strength with the types of damage that can occur, and indicates what types of

damage are likely to occur in which areas of the map. It is thought that using this high-density and dynamic information on wind speed distribution will enable more accurate operation control in the case of high winds and lead to shorter downtimes.

We are also researching how to determine when winds are likely to subside. Unlike with rainfall, where ebb and flow can be predicted to some extent by following the movement of rain clouds with meteorological radar tools, there are limits to judging when high winds will subside from observation data alone. Therefore, we are developing a method for predicting when high winds are likely to drop by analyzing the rise and fall patterns of strong winds for each meteorological event, such as the passage of typhoons and fronts. We hope to reduce downtime by combining real-time strong wind hazard maps and methods for predicting the end of strong winds.

In addition, we are researching a method for introducing probabilistic risk assessment into the investigations of operation regulation thresholds. It is thought that advancing this series of technological developments will contribute to the realization of highly accurate and effective operation control.

4.3 Facility condition evaluation

In parallel with technical work to develop more sophisticated operational regulations, we are researching and developing ways to evaluate the condition of railway installations. Here, we introduce technologies for evaluating the condition of embankments that have been damaged by rain, and technologies to evaluate safety in the event of scouring of ground around pier foundations during abnormally high-water levels.
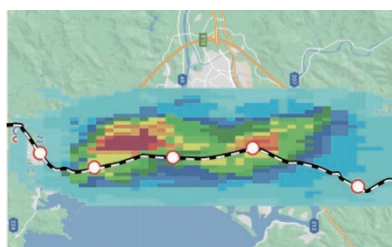

Fig. 5 Real-time strong wind hazard map (image) (wind speed distributions indicated with contours)

4.3.1 Judging performance of damaged slopes

There are several types of rain damage to embankment but the most common type is the collapse of the toe of the embankment slope. The scale of this damage can vary from a large collapse from the toe of the slope to the shoulder to where only the toe of the slope collapses. Here, we can clarify the scale of the damage that can support the load of the train in order to make quick judgments on a technical basis as to whether emergency train operations can be conducted on the damaged embankment. Therefore, we are working to clarify the relationship between the scale of damage and stability of the embankment. Figure 6 shows an experiment which involved the preparation of a full-scale model embankment that was sprinkled with water simulating rainfall and where part of the embankment collapsed due to a rise in groundwater level and increase in the degree of saturation, on top of which a train load was applied in order to clarify the relationship between the scale of collapse and the residual strength of the embankment. We are also aiming to generalize stability evaluations of damaged embankments by clarifying the

analysis method that reproduces the results of such model experiments and analyzing the relationship between the scale of collapse and the yield strength of the embankment under various conditions.

Furthermore, we are working on the development of reinforcement measures for the emergency resumption of operations on embankments that are judged to have an insufficient yield strength and are approaching the level of collapse. This series of technologies is expected to be used in cases where multiple disasters occur over a wide area, such as in the heavy rains of July 2018. For example, it is thought that the possibility of emergency resumption of operations or the selection of necessary reinforcement work can be rapidly determined by using drones to conduct inspections along railway lines in a short period of time and grasping the damage situation from the acquired images. This technology is thought to contribute to the reduction of downtime by making it possible to save labor during inspections and quickly create recovery plans after a disaster.
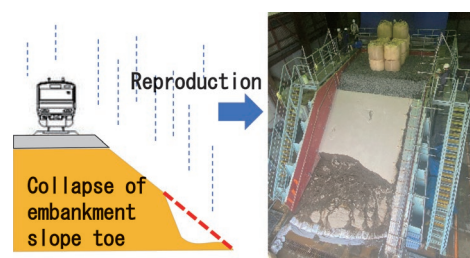

Fig. 6 Collapse experiment using full-scale model embankment

4.3.2 Monitoring of scouring of bridge piers during flooding

Disasters caused by heavy rain include not only slope failures but also damage and outflow of bridges due to abnormally high water levels in rivers. The heavy rainfall that occurred from the meteorological front in August 2021 also damaged several bridges in the Chubu and Kyushu regions. Such damage to bridges can be broadly classified into two types: cases where the river water rises to the height of the girders and sweeps them away by the water flow; and scouring, where the foundation ground of the bridge piers is washed away by the water flow, and the piers topple over or collapse. The latter involves cases where there is no significant deformation to the piers such as tilting even after the occurrence of scouring, and it was difficult to confirm while the water level was high whether stability for train loads was maintained. Therefore, RTRI has developed a system that monitors the stability of bridge piers based on changes in the natural frequency obtained from the microtremors of piers when the water level rises. Figure 7 shows a model experiment that was conducted in order to verify the ability of the developed system to identify the natural frequency. Here, obtaining the natural frequency of the pier using the microtremors measured by the sensors that are installed on the pier requires removing a component of the vibration transmitted from the ground that is contained in the measurement data as disturbance, and extracting the vibration of the pier itself. As shown in Fig. 7, the developed system measures microtremors at two points on the top of the bridge pier and uses the data to isolate ground vibrations.

This scouring monitoring system can be used to continuously confirm the stability of bridge piers from the full range of normal times to abnormal water level rises, and it is thought that safety evaluations that can be conducted without waiting for the lower river water levels can allow for rapid judgment of the early resumption of operations or a decision about which necessary measures should be taken.

Model pier
(simulation of scouring
of foundation)

Yellow circle:
microtremor sensor
(installed at two locations on
top end of bridge pier)

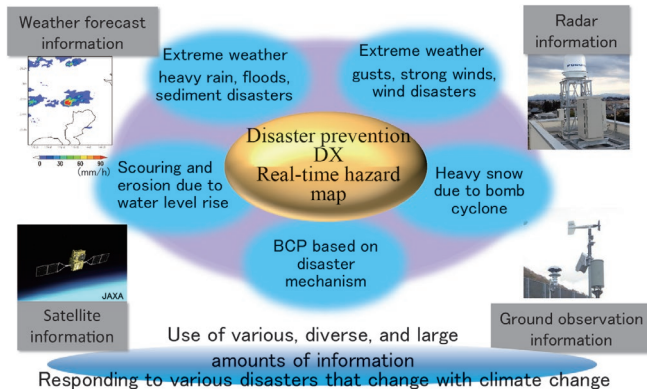**Fig. 7 Verification experiment of scouring monitoring system**

Fig. 8 The future of disaster prevention information system

5. Technological development for safer and more stable transportation

So far we have introduced research and development aimed at developing more sophisticated operational control and evaluating the condition of installations, among the technical developments which can contribute to improving the resilience of railways in response to increasingly severe weather events. All these technological developments have in common the aim of utilizing sensing data for safe and stable railway transportation. Recent advances in communication technology have enabled large volumes of sensing data to be obtained at high speed. Furthermore, a wide variety of information from outside railway companies has become easier to obtain

through the internet. As shown in Fig. 8, it is thought that combining this external information with existing internal information and utilizing it will enable the creation of a real-time hazard maps as part of an even more effective disaster prevention information system.

As an example of RTRI's forward-facing effort to use such digital data, themes relating to the use of satellite information are being advanced. In future, assuming that a large number of small satellites will be launched making data easier to obtain, we are conducting research on how to utilize such data for railway disaster prevention.

6. Conclusions

In this article, we introduced current research and development aimed at improving the resilience of railways against increasingly severe weather events. In addition to this, we also are widely involved in the development of evaluation techniques related to disaster prevention, such as methods for evaluating debris flow hazard areas, development of survey methods for evaluating the safety of aged slopes, elucidation of rock deterioration mechanisms, methods for evaluating snowfall distribution using meteorological radar, and methods for estimating the amount of falling snow. We hope to continue contributing to improving the resilience of railways through this research and development.

References

[1] IPCC, "AR6 Climate Change 2021: The Physical Science Basis," https://www.ipcc.ch/report/ar6/wg1/ (accessed 2021-12-06).
[2] Japan Meteorological Agency, "CLIMATE CHANGE MONITORING REPORT 2021," https://www.jma.go.jp/jma/en/NMHS/ccmr/ccmr2021.pdf/ (accessed 2022-09-27).
[3] Osamu NUNOKAWA, Naoyuki OTA, "Risk Evaluation of Debris Flow using a Digital Terrain Model," *QR of RTRI*, Vol. 55, No. 3, 2014.

Author

Osamu NUNOKAWA, Dr. Eng.
Director, Disaster Prevention Technology
Division
Research Areas: Slope Disaster

Maglev Technology and Research Trends on Superconductivity

Masaru TOMITA

Maglev Systems Technology Division

Railway Technical Research Institute has conducted research and development of superconducting Maglev and superconductivity. In this paper, we introduce ground coil evaluation technology, wireless power transfer technology and linear rail brake technology as applied Maglev technology. In addition, we introduce outlines of our recent research such as the science of high-temperature superconductors, superconducting feeder cables, and superconducting magnetic energy storage.

Key words: *maglev, superconducting magnet, high-temperature superconductivity, feeder cable, power storage*

1. Introduction

At the Railway Technical Research Institute, we are conducting research on superconducting magnetic levitation railways (maglev) by evaluating ground coils as a basic technology as well as its applications, for example, to linear rail brakes and contactless power supply technologies that do not require overhead wires. Furthermore, with regards to superconducting technologies, we have focused our efforts on a wide range of research and development that is not limited to maglev. There is a long history of high-temperature superconductivity research at the Railway Technical Research Institute [1]. On this front, we have been working on basic research such as superconducting material production, evaluation technology, winding technology, and coiling technology. This research has then been applied to railways such as power transmission, energy storage, and power converters. Superconductivity research and development is becoming more competitive as a global energy strategy, and the technology of the Railway Technical Research Institute is also attracting attention in the field of superconducting power transmission development (Fig. 1).

2. Maglev technology

The first maglev on the premises of the Railway Technical Research Institute was operated in 1972, and following basic running experiments on the Miyazaki test center, running tests have been conducted on the Yamanashi test center jointly with JR Central since 1997. Currently, we are working on basic research on ground coils and car motion on maglev, as well as applied research such as linear rail brakes and contactless power supply for conventional railways using knowledge obtained from the research and development of maglev (Fig. 2).

2.1 Ground coil

The durability of ground coils that are installed in guideways are important in maglev. The electromagnetic vibration test device is a device that vibrates with an electromagnetic force that is almost equivalent to that during the running of a train, which occurs by installing the ground coil to be evaluated in front of the superconducting magnet and energizing an alternating current in the magnetic field. Durability against actual vibration can be evaluated using this. We are also aiming to contribute to maintenance work by clarifying failure sign detection methods, and remaining lifespan estimation

Fig. 1 Global trends in high-temperature superconductivity research (From IEA annual report [2]. For Japan, the development status of superconducting power transmission by the Railway Technical Research Institute is shown)
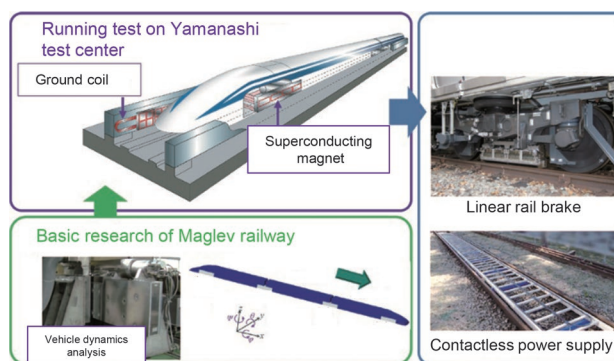

Fig. 2 Maglev technology

methods by conducting various durability tests such as environmental tests and high voltage tests.

2.2 Linear rail brake

We are working on the development of a linear rail brake that does not depend on adhesive force by applying linear motor technology with the objective of securing a braking force in the high-speed range [3]. Conventional eddy current-based rail brakes rely on direct current excitation and cannot be used in the event of a power failure. Thus, there was the issue of the kinetic energy during the train running turning into Joule heat due to eddy currents and raising the temperature of the rail during operation. Therefore, we devised a linear rail brake that applies the dynamic braking principle of a linear induction motor (LIM) and are currently conducting research and development on this. A feature of this system is that the power required for braking is self-generated by the device itself, and the increase in rail temperature can be suppressed. However, cost has been a problem because an inverter is required. In order to solve this problem, we proposed an inverter-less excitation method that reduces this cost by applying capacitor self-excitation. The practical applicability of this method was confirmed its practicality and is expected to reduce costs significantly.

2.3 Contactless power supply system

We are working on the development of a transformer type contactless power supply system as a form of intermittent power supply method for railway cars that are equipped with running batteries, similar to recently introduced diesel hybrid cars and battery-equipped cars that can run on non-electrified sections [4]. This power supply is contactless and wear-free compared to pantographs and other power supply systems, which makes it easier to maintain, and the lack of exposure of the charging parts makes it safer. Additionally, if the power density can be increased then the capacity of the battery that is installed in the vehicle can be reduced, which has the advantage of contributing to weight reduction. To date, we have designed and prototyped current-collecting coils mounted on railway cars and power supply coils that are installed between rails, and we confirmed a current collecting power density of 150 kW/m^2.

3. Superconductivity research and development

3.1 Basic research on superconductivity

Superconductivity is a phenomenon in which electrical resistance is brought to zero by cooling below a certain temperature. Electrons in ordinary materials are scattered by the vibration of atomic nuclei and impurities, and this becomes electrical resistance. In the superconducting state, two electron pairs form a pair (i.e., Cooper pair). When the electron moves, it attracts the nucleus, but the nucleus does not return to its original position immediately after the electron flies away. As a result, a positively charged area is created after the electron flies off, which then attracts another electron to form a pair (Fig. 3). When viewed as a pair, there is nothing that hinders the movement of the Cooper pair, which signifies current, and the electrical resistance is zero. In ordinary materials, the interaction between the nuclei and electrons is too strong in order to form Cooper pairs; however, in specific materials, cooling weakens the interactions, thereby allowing formation of a Cooper pair and developing superconductivity. This perfect conductivity is the only way

to solve the issues caused by electrical resistance to date, and here at the Railway Technical Research Institute, we have conducted research on materials that would maximize these characteristics. These achievements enable the achievement of revolutionary improvements in the characteristics and efficiency of equipment.

Typical forms of high-temperature superconducting materials include columnar bulk materials for magnetic field applications and longitudinally elongated tapes for power transmission applications. Their respective shapes very, but the materials used and the processes of mixing / pressing / sintering raw material powders are the same. Therefore, even when developing high-temperature superconducting tapes, bulk materials need to be manufactured and their characteristics evaluated. Figure 4 shows the crystal structure of the main high-temperature superconducting materials. Here, since the superconducting current flows through the CuO$_2$ plane, it is extremely important to align the crystal orientation. Bulk materials are produced by filling powder into a molding machine, molding it into a disk shape using a press, and sintering it in an electric furnace. The single crystal is grown by the melt-solidification method in order to align the crystal orientation during sintering. This melt-solidification method involves aligning the crystal orientation in the circumferential direction from the single crystal that is placed in the center. Therefore, it is important to adjust the temperature and composition when increasing the size, and as shown in Fig. 5, we are researching the particle size of the synthesized powder, composition control, and the optimization of the temperature conditions when firing in an electric furnace.

The superconductivity performance is indicated by the critical current value as an index and corresponds to the current carrying capacity for tapes. However, the critical current value is calculated from the generated magnetic field for bulk materials. A strong magnetic field means that a large amount of current can flow through the material. To date, there has been fierce international competition for high magnetic field generation in high-temperature superconducting materials. Since 2000, Austria, Germany, and Japan have competed over this research field, and in 2003, the Railway Technical Re-
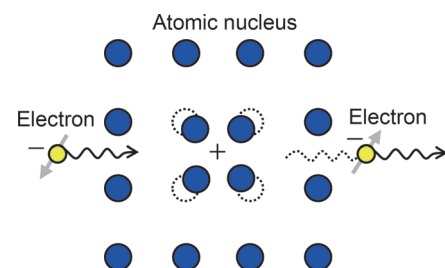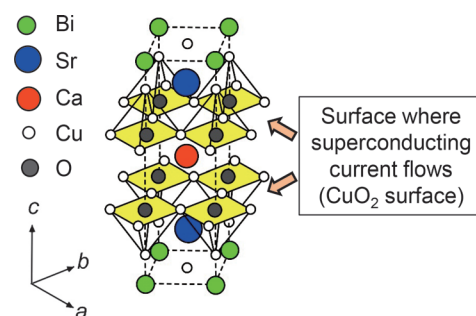

Fig. 3　Cooper pair

Fig. 4　Crystal structure of Bi-based superconducting material

search Institute achieved a world record of 17.24 T [1]. Increases in the generated magnetic field value also increase the electromagnetic force applied to the superconducting material, which in turn increases the load on material strength. Furthermore, under a high magnetic field, the heat that is generated when the magnetic flux moves reduces the current flowing through that section. We addressed these issues of mechanical strength and thermal instability and used a manufacturing method that uses low-melting-point metals and resins, thereby achieving the world's highest generated magnetic field. Over the next 11 years and five months, Japan maintained this record, but an international joint U.S.-U.K. team focused on this research and achieved a new world record of 17.6 T [5] (Fig. 6). It was shown that a current as high as 1000 A could be passed through a superconducting tape with a diameter of 1 mm by generating a magnetic field of 17 T. These results achieved a large current capacity, which opened the way to various applications of high-temperature superconductivity.

High-temperature superconducting tapes need to have their crystal orientation aligned in the longitudinal direction and are classified into sheath tapes and thin-film tapes. Here, we introduce research on the former. The crystal orientation of Bi-based superconducting materials can be aligned by packing powder into a metal pipe and stretching it linearly with a rolling mill. Figure 7 shows the
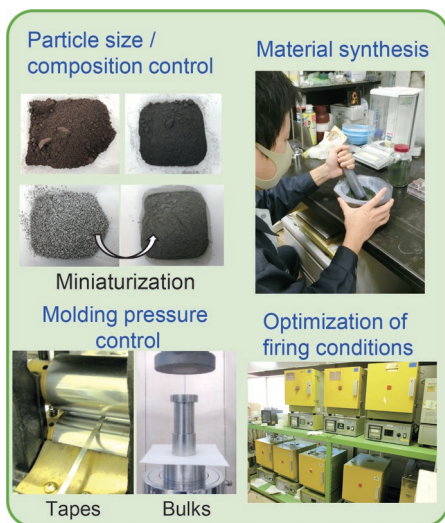
microstructure of the Bi-based superconducting tape that is observed with a scanning electron microscope. The linear contrast running to the left and right is that of the Bi-based crystal, and the direction of the Bi-based crystal plane corresponds to the longitudinal direction. The crystal plane is gently curved or interrupted in some places. Granular contrast is observed at the locations indicated by the arrows in the figure, and the orientation of the Bi-based crystals changes locally. Around impurity A, the crystal bends gently as if to surround the impurity; whereas on the left and right and right of impurity B, the Bi-based crystal is clearly cut off. A break in the crystal plane cuts off the superconducting flow path, so the formation of such impurity phases need to be suppressed. Therefore, the impurity phase is reduced and the crystal orientation is controlled by adjusting the firing temperature and applied pressure. We analyze and evaluate the fabricated materials in this way in order to achieve high-performance materials.

3.2 Applied research on superconductivity

We are advancing development through evaluation technology and winding / coiling technology (Fig. 8) based on the materials and other results obtained from basic research. We are conducting evaluation tests in refrigerant using prototyped cables and coils, with the aim of achieving superconducting equipment for railway applications such as power transmission and energy storage.

3.2.1 Superconducting feeding system

Transmission loss and voltage drops occur in electric railways due to the electrical resistance of transmission lines that send electricity from the substation to the train. Substations are positioned so as to secure the power needed for operation, and many are installed particularly on metropolitan railway lines. We are developing a superconducting feeding system in order to address these issues caused by electrical resistance. Transmitting power using superconductivity, which involves zero electrical resistance, is expected to

Fig. 5 Fabrication of high-temperature superconducting material

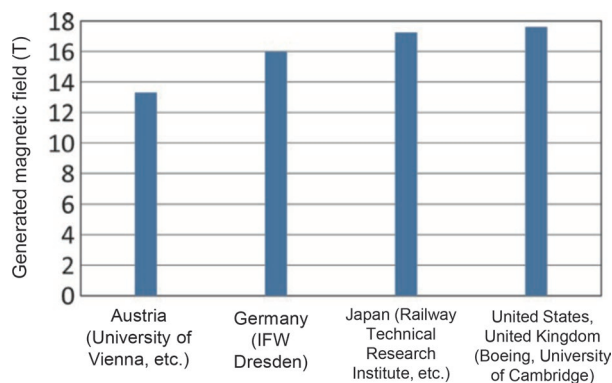**Fig. 6 International competition in high-temperature superconductivity research (Magnetic field generated by bulk magnet)**
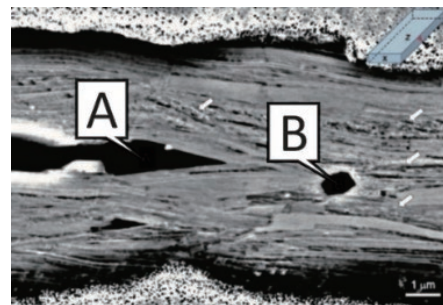

Fig. 7 Observation of microstructure of high-temperature superconducting tape
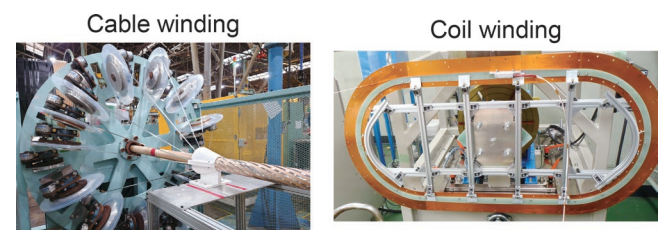

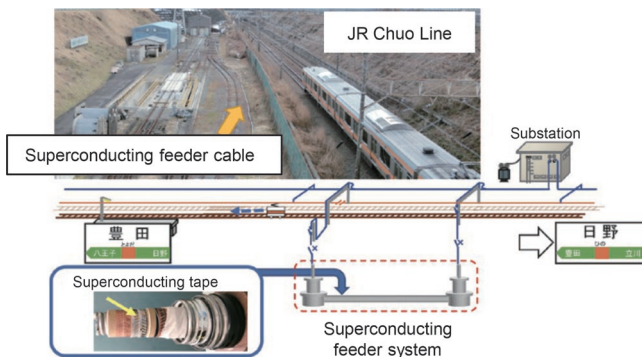**Fig. 8 Winding (coiling) of high-temperature superconducting material**

Fig. 9 Development of 408 m long superconducting feeding system

Fig. 10 Development of long-distance superconducting feeding system

Fig. 11 Superconducting magnetic energy storage system

ficult to charge and discharge them rapidly. Furthermore, the number of times they can be charged or discharged is limited. Therefore, we are working on the development of a superconducting magnetic energy storage system that stores electricity directly in coils made of superconducting materials. Such systems have many advantages over conventional batteries: for example, they can directly extract the electricity flowing through the superconducting coil, allowing it to charge and discharge quickly; and not generating heat even with large current flows, allowing for repeated charging and discharging multiple times and a long service life. We are also conducting research and development on next-generation superconducting coils using magnesium diboride (MgB_2) wires that do not require liquid helium for cooling [7] (Fig. 11). The MgB_2 coil can be cooled only by conduction cooling with a refrigerator without using a refrigerant, and it can also be cooled using liquid hydrogen, so this is compatible with a future hydrogen society that does not emit carbon dioxide.

4. Conclusions

We introduced recent research and development efforts and results of superconducting maglev and superconducting technology. We will continue to advance the basic technology of maglev, and in the superconductivity fields, we are utilizing the results of high-temperature superconductivity that have been cultivated to date and aim for technological innovation in the railway fields by promoting integrated and efficient research, ranging from basic research to applied research as well as demonstrations.

achieve energy-saving effects such as reduction of power transmission loss, improvement of regeneration efficiency, and integration of substations [6]. This system consists of a superconducting feeder cable for power transmission, a cooling device for cooling those cables, and a protection circuit that is needed for connection to the railway. To date, we started with research on high-temperature superconducting materials. Afterwards, we conducted demonstrations on the test line in our Institute through optimization of the cable structure and system experiments. We then connected the 408-m superconducting feeder cable that we developed to part of the railway line between Hino Station and Toyota Station on the JR Chuo Line, ran the E233-series train car (10-car train), and confirmed that the voltage drop on the actual railway line was suppressed (Fig. 9). In addition to the experiment on this railway line, power transmission tests for superconducting feeder cables were implemented on the Izuhakone Railway Sunzu Line (3000-series train), Toden Arakawa Line (8900-series train), and the Tokyo Metro Marunouchi Line (02-series train). Furthermore, we have proceeded with the construction of a long-distance (km-class) system whose introduction is assumed to be between substations at the Miyazaki test Center, which was a former Maglev experimental line, and we are conducting research and development that aims to achieve a practical system (Fig. 10).

3.2.2 Superconducting magnetic energy storage

When introducing power storage into railway lines, a high input / output and long service life are needed to handle the railway load. Conventional batteries rely on chemical reactions, so it is dif-

References

[1] Tomita, M. and Murakami, M., "High-temperature superconductor bulk magnets that can trap magnetic fields of over 17 tesla at 29K," *Nature*, Vol. 421, pp. 517-520, 2003.

[2] International Energy Agency, "IEA Technology Collaboration Programme on High Temperature Superconductivity 2020 Annual Report," https://ieahts.org/downloads/2020-HTS-TCP-Annual-Report-Final.pdf

[3] Sakamoto, Y., Ukita, K. and Sasakawa, T., "State Monitoring Method for a Linear-Motor-Type Rail Brake using an Excitation Inverter," *RTRI Report*, Vol. 34, No. 11, pp. 25-30, 2020 (in

Japanese).

[4] Yoda, H., Sakamoto, Y., Kashiwagi, T. and Sasakawa, T., "Design Study Aiming at Increasing Transfer Power per Unit Area of the Coil for the Wireless Power Transfer System of Railway Vehicles," *RTRI Report*, Vol. 33, No. 5, pp. 17-22, 2019 (in Japanese).

[5] Durrell, J.H. et al., "A trapped field of 17.6T in melt-processed, bulk Gd-Ba-Cu-O reinforced with shrink-fit steel," *Supercond. Sci. Technol.* 27, 2014082001, 2017.

[6] Superconductors drive trains, *Nature*, Vol. 542, p. 275, 2017.

[7] Onji, T., Ishihara, A., Kobayashi, Y., Fukumoto, Y., Tomita, M. and Hamajima, T., "Fundamental Study of MgB_2 Super Conducting Coil for Storage," *RTRI Report*, Vol. 32, No. 10, pp. 41-46, 2018 (in Japanese).

Author

Masaru TOMITA, Dr. Eng.
Director, Head of Maglev Systems
Technology Division
Research Areas: Superconducting Technology

Performance Verification of Design Method for Plain Concrete Linings and Inverts Assuming Ground Displacement after Completion

Keisuke SHIMAMOTO   Kazuhide YASHIRO

Tunnel Laboratory, Structures Technology Division

Noriyuki OKANO

Tunnel Laboratory, Structures Technology Division (Former)

There are various structures in railway systems. These structures including tunnels need to have the same level of performance and their performance should be verified quantitatively. Therefore, we proposed a method for verifying the performance of plain concrete linings and inverts, and developed a trial design assuming a mountain tunnel receiving ground deformation after completion. In the trial design, we imposed the displacement to the lining and invert using a ground deterioration model. As a result, it was found that the performance can be verified using the proposed method, and that the required performance can be satisfied by adopting strong invert structures against floor heave.

1. Introduction

ISO2394 [1] and Eurocode 0 [2] have been issued as comprehensive design codes that define the basics and systems of structural design, and performance-based design methods are common in the world. Even though mountain tunnels are the least suitable structures for performance-based design methods, they were introduced for the first time in Japan in 2022 as the design standard for railway tunnels [3].

As shown in Fig. 1, the above design standards indicate that the structure and design concept for mountain tunnel linings and inverts should be selected according to the following three conditions:

Condition 1: When a constant external force other than self-weight is assumed

Condition 2: When displacement from the ground is expected after tunnel completion

Condition 3: Other than the above

In the case of condition 1, it is sufficient to design a reinforced concrete structure based on a framework analysis that applies loose earth pressure, total earth pressure, or ground displacement during an earthquake. Since condition 3 is considered to act only on its own weight, it is sufficient to confirm that there is no problem with its own weight as a plain concrete structure. In Japan, after ensuring the convergence of ground deformation with strong supports, in many cases condition 2 is treated as condition 3 where linings and inverts are made of plain concrete.

However, in the case of condition 2, it may be necessary for a railway company to prepare for actualization of deformation after service. Examples of such cases include cases where linings and inverts need to be cast before confirming reliable convergence of ground deformation, and cases where the geology is quite bad. Since there have been several cases in recent years of mountain tunnels in Japan in which floor heave has been a problem after the completion of the tunnel [4], it may be necessary to conduct a performance verification of the invert structure to deal with floor heave.

In the following, an example of performance verification of plain concrete linings and inverts is shown for special conditions where numerical verification is required in the case of condition 2.

2. Performance verification using ground deterioration method

2.1 Overview

In this study, it was assumed that linings and inverts would be placed in a state where it takes a long time for ground deformation to converge after excavation and a slight displacement rate remains. The action of ground pressure is expressed by the ground degrada-
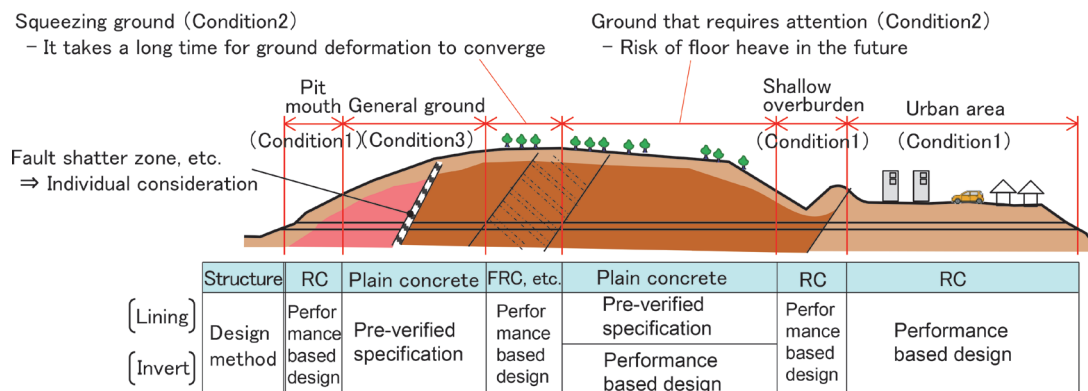

Fig. 1 Classification of lining and invert design methods for railway mountain tunnels

tion method [5].

The ground deterioration method is characterized by expressing the ground pressure action on lining and invert by stress redistribution that accompanies plasticity due to a decrease in ground strength [6].

Figure 2 shows the flow of the performance verification using the ground deterioration method, and Fig. 3 shows the analysis model of the ground deterioration method.

First, the excavation stage is analyzed, and then the strength reduction stage is analyzed. In stage 1 of the strength reduction stage, the strength of ground without installing linings or inverts is reduced until a predetermined tunnel displacement (residual displacement) is achieved. Next, in stage 2, the strength of the ground with linings and inverts installed is reduced by the same amount as in stage 1. At this time, the stresses generated in the lining and inverts are verified.

2.2 Conditions of verification

Table 1 shows the physical properties used in the analysis. In order to express squeezing ground, the physical properties of the ground were set assuming low-strength soft rock. Assuming rock mass grade I_s, which is specified in the design and construction

standards for Shinkansen tunnels in Japan, various physical property values were set so that a horizontal displacement of about 100 mm would occur during excavation. Specifically, the uniaxial compressive strength of the ground was set to 2.0 MPa so that the ground strength ratio was 0.5. Other physical properties were set based on the correlation between the unconfined compressive strength of soft rock and various physical properties shown by

Table 1 Physical properties used in the analysis

	Physical property		unit	Value
Ground	Overburden	h	m	200
	Uniaxial compressive strength	q_u	MPa	2.0
	Ground strength ratio	C_f	—	0.5
	Specific weight	γ	kN/m³	20
	Elastic modulus	E	MPa	206※
	Poisson's ratio	ν	-	0.36
	Cohesion	c	kPa	580※
	Internal friction angle	φ	°	31
	Dilation angle	λ	°	10
	Lateral pressure coefficient	K_0	—	1.0
Lining Invert	Elastic modulus	E	MPa	22,000
	Poisson's ratio	ν	-	0.20
	Specific weight	γ	kN/m³	23.5
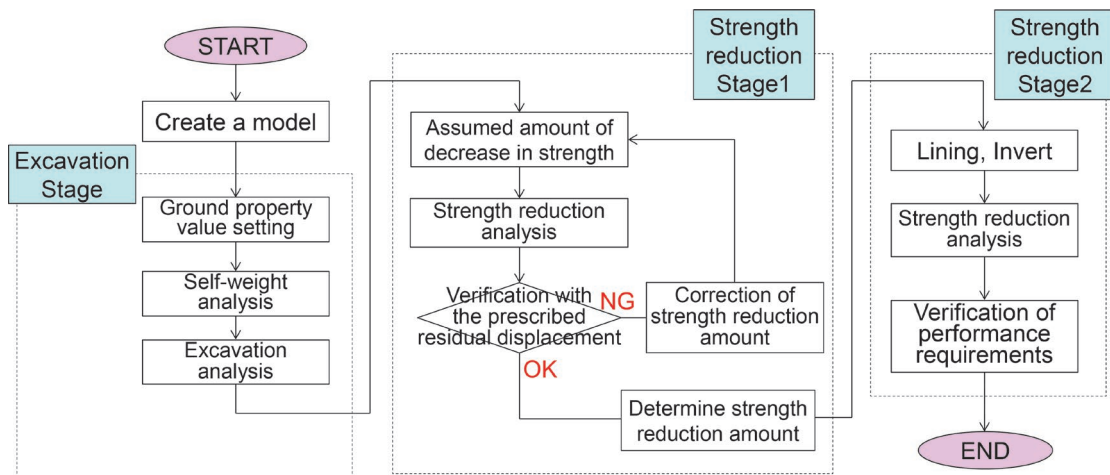
Fig. 2 Flow of the performance verification using the ground deterioration method

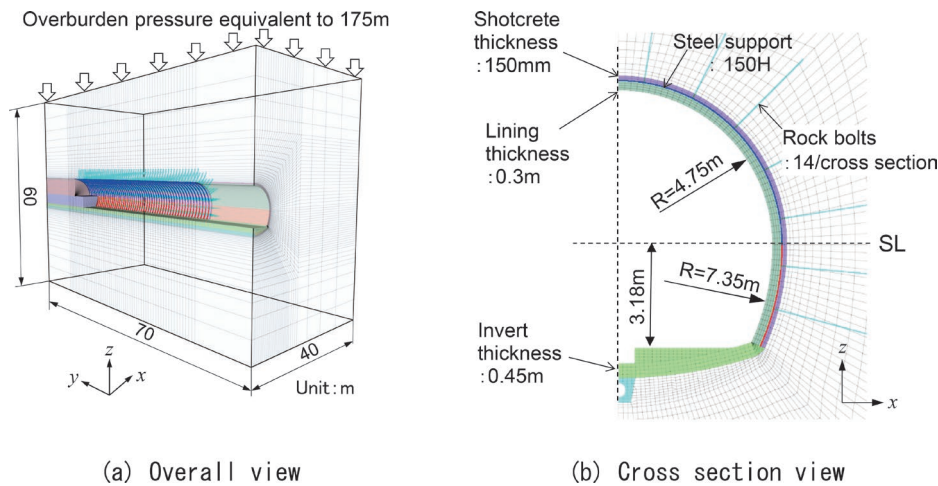(a) Overall view

(b) Cross section view

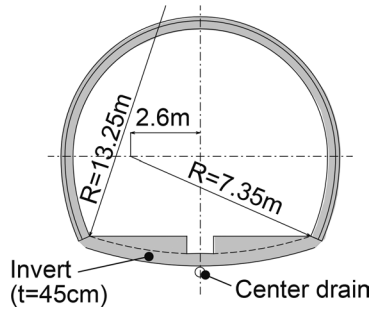Fig. 3 Analysis model of the ground deterioration method

Fig. 4　Cross section used for analysis

Aidan et al. [7] and Jiang et al. [8].

The ground was modeled as elastic-perfectly plastic Mohr-Coulomb yield criterion.

The target tunnel for analysis was the Shinkansen standard cross section (Fig. 4). The lining is made of plain concrete with a thickness of t = 30 cm, and the invert is made of plain concrete with a thickness of t = 45 cm (called I_N invert).

The support (shotcrete, rock bolt, steel support) was modeled as a standard support pattern for rock class I_S.

2.3　Performance requirement

Regarding the serviceability of mountain tunnel linings and inverts, according to the past construction results, there have been no problems in use if proper construction has been carried out. In other words, serviceability is considered to be satisfied when waterproofing and drainage works whose performance has been confirmed by past records are used. Therefore, we decided to take up safety (failure) here as the required performance.

The basic principle of safety (failure) inspection is to confirm that linings and inverts will not be failed. However, evaluation methods for lining and invert failure in plain concrete have not been established. Therefore, as a safe side evaluation, it was decided to confirm that no tensile cracks occurred in the lining and invert, that is, the verification value obtained by dividing the tensile stress by the design tensile strength was less than 1.

Table 2 shows the safety factors used in the design. Although no established safety factors have been presented for the performance verification of plain concrete, the safety factors for the performance verification of RC structures are applied correspondingly here.

2.4　Excavation analysis

In the analysis model shown in Fig. 3, excavation is represented by removing elements, and installation of supports (steel shoring, shotcrete, rock bolts) is represented by adding structural elements.

Excavation and support were carried out according to the progress of the face, expressing the stepwise excavation of the tunnel. Figure 5 shows the analysis results of the excavation stage. It can be seen that the horizontal convergence displacement during excavation is about 100 mm. Here, the horizontal convergence displacement is taken as the value at SL + 1.5 m height, which is the place where the measurement starts immediately after the upper half face passes. Since the convergence displacement is about 100 mm, it was judged to be appropriate as a physical property value expressing the ground of I_S ground grade.

Table 2　Safety factors used in the design

Performance requirement	Action factor	Structural analysis factor	Material factor	Member factor	Structure factor
Safety	γ_f	γ_a	γ_m	γ_b	γ_i
	1.1	1.0	1.3	1.1	1.2

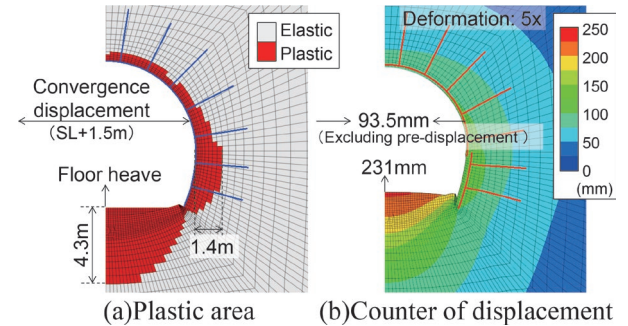　　　(a)Plastic area　　　(b)Counter of displacement

Fig. 5　Result of tunnel excavation

2.5　Action

In this performance review, it is assumed that the lining and the invert are placed with a slight displacement rate remaining. At this time, ground pressure due to residual displacement acts on the tunnel. For this action, lining and inverting are verified not to reach critical conditions. As a slight displacement speed, we assume 1 mm/month, which is a guideline for judging whether lining can be placed. In this study, it was assumed that the horizontal displacement progressed according to the Voigt model of (1).

$$u = u_0(1 - \exp(-\alpha t)) \tag{1}$$

Here,

u : Horizontal displacement (mm)
u_0: Final horizontal displacement (mm)
α : Convergence factor (1/day)
t : Elapsed days from the start of measurement (days)

The displacement velocity is given by equation (2).

$$\frac{du}{dt} = u_0 \cdot \alpha \cdot \exp(-\alpha t) \tag{2}$$

Elapsed days t_1 when the displacement rate is 1 mm/month (=1/30 mm/day) or less is given by (4) obtained from (3).

$$u_0 \cdot \alpha \cdot \exp(-\alpha t_1) \leq \frac{1}{30} \tag{3}$$

$$t_1 \geq \frac{1}{\alpha} \ln(30 \cdot \alpha \cdot u_0) \tag{4}$$

The displacement (residual displacement) u_{res} that occurs after the elapsed days t_1 is expressed by (5).

$$u_{res} = u_0 - u_1 = \frac{1}{30\alpha} \tag{5}$$

Here,

u_1: Horizontal displacement at elapsed days t_1

The convergence coefficient α was set based on past cases. Figure 6 shows actual measurement data of horizontal displacement during excavation at a location where a floor heave occurred after

the completion of construction in the past. When the data indicated in Fig. 6 is fitted by the least-squares method using α in equation (1) as a parameter, $u_0 = 117.7$ and $\alpha = 0.065$ are obtained in this example, and the residual displacement u_{res} at this time is 0.51 mm. As shown in Table 2, the coefficient of action $\gamma_f = 1.1$, so the target residual displacement in the analysis was $0.51 \times 1.1 = 0.56$ mm.

Based on the above concept, as the strength reduction stage 1, the cohesion of the ground was reduced after the upper and lower half excavation and before excavating the invert.

Here, when the ground cohesion c was decreased by 0.61% from the initial value, the shrinkage displacement reached 0.56 mm. Figure 7 shows the plastic region and displacement contour when the ground cohesion is reduced by 0.61% as a result of strength reduction stage 1.

Finally, the analysis of strength reduction stage 2 was performed. That is, when the cohesion of the ground was reduced by 0.61% after excavating the invert and placing the lining and invert, the stress generated in the lining and invert was calculated.

2.6 Performance verification

The stresses obtained in the previous section are checked. Table 3 shows the verification cases. Response values were calculat-
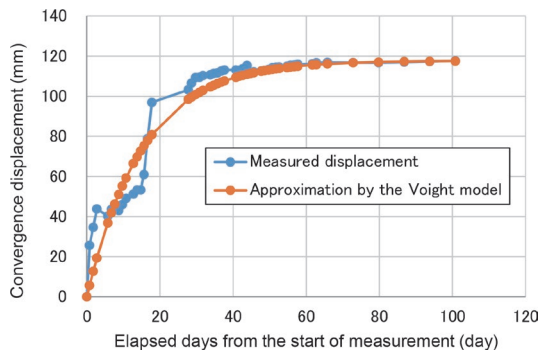

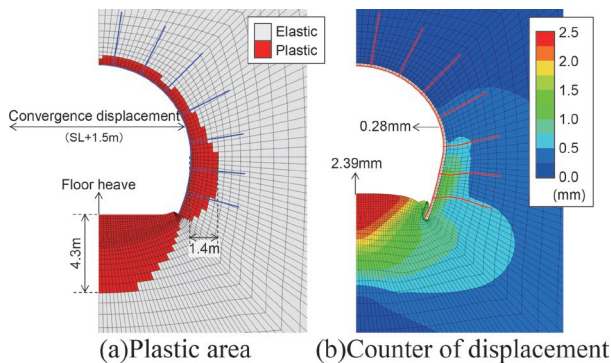**Fig. 6 An example of a Voigt model approximation of actual measured displacement**

(a)Plastic area   (b)Counter of displacement

Fig. 7 Plastic area and Counter of displacement (Strength reduction stage 1, displayed as displacement at the time of tunnel completion = 0)

Table 3 Verification cases

	Invert	Lining	Remarks
Case0	Unexcavated	Without	Strength reduction stage 1
Case1	With	Without	Strength reduction stage 2
Case2	With	With	

ed and verified for two cases: Case 1 with only invert and Case 2 with both lining and invert. In general, the lining is constructed after a certain period of time after the invert is constructed, but here, the lining is assumed to be cast at the same time as the invert.

The verification value (ratio of response value and limit value) was arranged for each element of lining and invert. The safety factors shown in Table 2 are used to calculate response values and limit values. Figure 8 shows the verification values (ratio of tensile stress to tensile strength). As shown in Fig. 8, since the verification value was less than 1, no cracks occurred, and the required performance was satisfied.

As a reference, Fig. 9 shows the amount of displacement when the cohesion of the ground decreased by 0.61%. In Case 0, the horizontal displacement is 0.56 mm $\fallingdotseq 0.6$ mm, while the floor heave is 2.4 mm. On the other hand, in both Cases 1 and 2, little the displacement and floor heave occurred.

3. Effects of differences in ground conditions

3.1 Conditions of the verification

The verification example shown in Chapter 2 was for a case where the deformation of the ground was relatively small, and the result was that no cracks occurred in the lining or invert. However, if the ground conditions are worse, the residual displacement may be larger than the results obtained in Chapter 2.

In this chapter, we will attempt to verify the case in which a relatively large residual displacement acts using a similar method. Here, the performance verification was performed by assuming that the residual displacement was increased from 0.56 mm to 3 mm. Note that a residual displacement of 3 mm corresponds to a reduction rate of 3% in the cohesion of the ground.

In addition, since the generated stress is considered to be larger, we also examined the "invert structure to cope with floor heave" shown in Fig. 10. Table 4 shows the verification cases.

The safety factor, numerical analysis model, analysis input values, and analysis flow are the same as in Chapter 2. The calculation of the action is the same as in Chapter 2, except that the reduc-
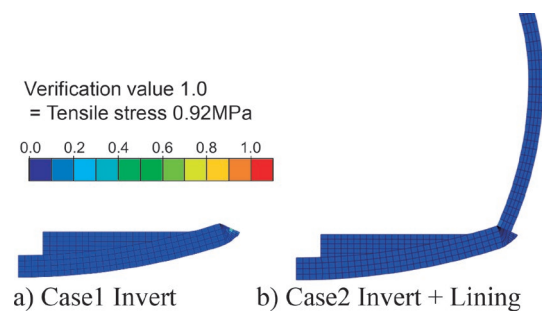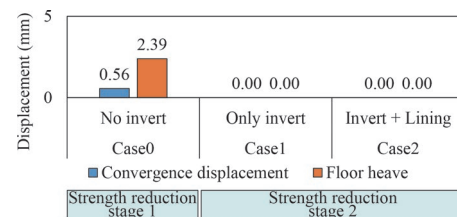

a) Case1 Invert   b) Case2 Invert + Lining

Fig. 8 Verification value (Tensile stress)

Fig. 9 Displacement when cohesion decreases by 0.61%

(a) I_NAiP invert
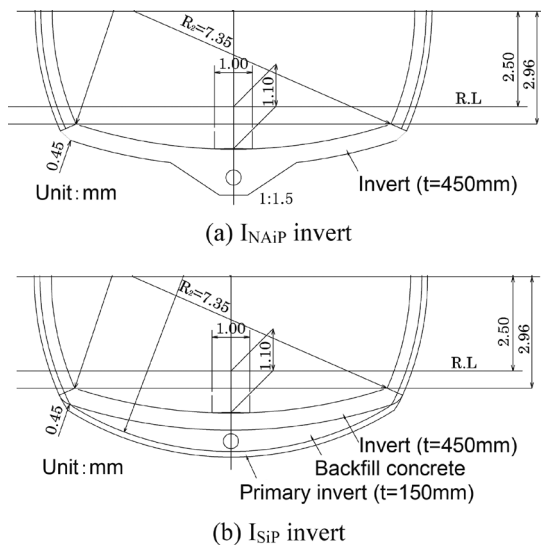
(b) I_SiP invert

Fig. 10   Invert structures to cope with floor heave

Table 4   Verification cases

	Invert	Lining	Remarks
Case10	Without	Without	Strength reduction stage 1
Case11	I_N invert	Without	
Case12	I_{NAiP} invert	Without	
Case13	I_{SiP} invert	Without	Strength reduction stage 2
Case14	I_N invert	With	
Case15	I_{NAiP} invert	With	
Case16	I_{SiP} invert	With	

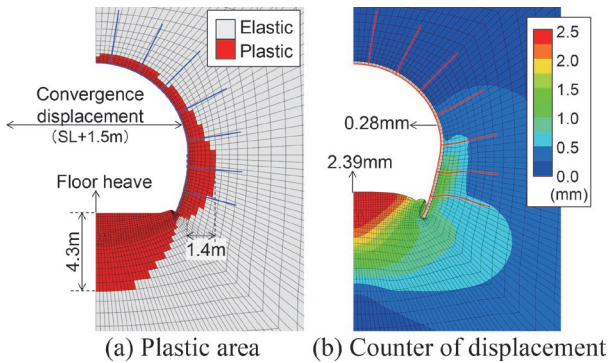(a) Plastic area   (b) Counter of displacement

Fig. 11   Plastic area and Counter of displacement (Residual displacement of 3 mm is applied) (Strength reduction stage 1, displayed as displacement at the time of tunnel completion = 0)

tion rate of the ground cohesion increases from 0.61% to 3.0% and the residual displacement increases from 0.56 mm to 3 mm.

Figure 11 shows the plastic region and the displacement contour when the cohesion of the ground is reduced by 3.0% as a result of the strength reduction stage 1.

3.2   Results of verification

As in Chapter 2, the verification values (the ratio of the response value to the limit value) of the tensile stress were arranged for each element of the lining and the invert. Figure 12 shows the verification values (tensile stress) for Cases 11 to 13 with invert only. Figure 12 shows the following for each case.
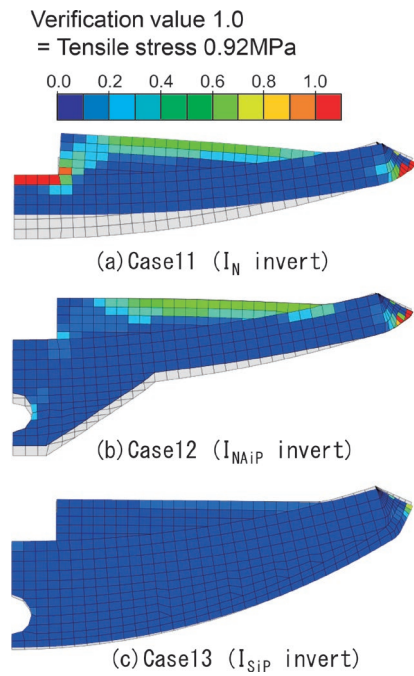

(a) Case11 (I_N invert)

(b) Case12 (I_{NAiP} invert)

(c) Case13 (I_{SiP} invert)

Fig. 12   Verification value (Case11~13) (Display deformation by 200 times)

(a) Case14
(I_N invert+Lining)

(b) Case15
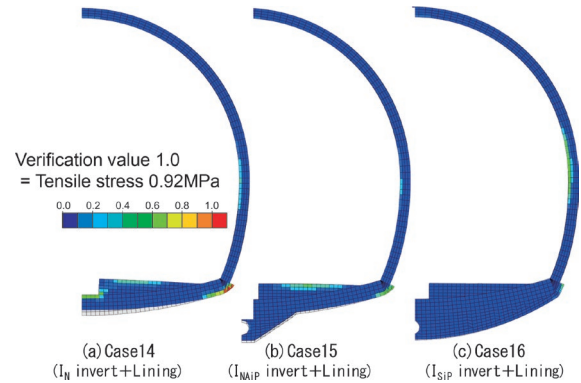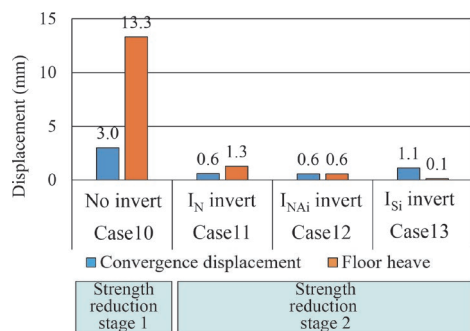(I_{NAiP} invert+Lining)

(c) Case16
(I_{SiP} invert+Lining)

Fig. 13   Verification value (Case14~16) (Display deformation by 200 times)

· In the case of Case 11 (I_N invert), an area where the verification value exceeds 1 (area where tensile cracks occur) occurred in the central passage. In addition, an area where the verification value exceeds 1 also occurs in the joint between the shotcrete and the invert. This is presumed to be due to the fact that the area of the joint is small and stress concentration occurs locally.

· In Case 12 (I_{NAiP} invert), the area where the reference value exceeds 1 in the central passage is no longer seen. However, for the same reasons as in Case 11, there are regions where the verification value exceeds 1 at the joints with the shotcrete.

· In Case 13 (I_{SiP} invert), both the central passage and the joints with the shotcrete satisfied the verification.

Figure 13 shows the verification values (tensile stress) for Cases 14 to 16 of invert and lining. In the case of constructing lining in addition to invert, the verification value becomes smaller overall. However, in Case 14, there are areas where the verification value exceeds 1 at the joint between the lining/shotcrete and the invert. On

(a)Case11〜13 : Only invert
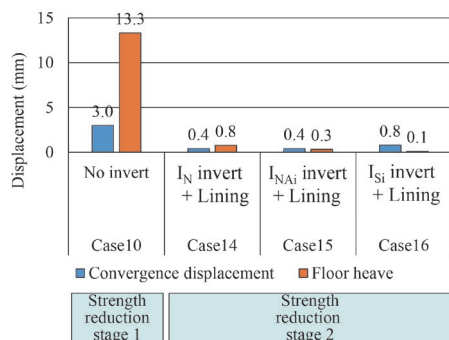
(b)Case14〜16 : Invert + Lining

Fig. 14　Displacement when cohesion decreases by 3.0%

the other hand, in Cases 15 and 16, there is no region where the reference value exceeds 1, so that the effect of invert structure to cope with floor heave can be seen.

As a reference, Fig. 14 shows the amount of displacement when the cohesion of the ground decreased by 3.0%. From Fig. 14, it can be confirmed that floor heave can be greatly suppressed by invert. In addition, it can be confirmed that floor heave can be further suppressed by adopting I_{NAiP} invert and I_{SiP} invert. However, since the I_{SiP} invert causes a large excavation of the roadbed during excavation, loosening of the ground behind the side wall occurs, and the convergence displacement becomes larger. A similar trend can be confirmed for the case of invert and lining.

4.　Conclusion

We presented an example of the performance verification method for plain concrete lining and invert as part of a study to examine the shift to a performance verification design method for mountain tunnel. The action is obtained assuming that the tunnel receives residual displacement from the ground after the completion of the tunnel. The obtained results of this study are summarized below.

　1) A numerical analysis method was presented to apply an action equivalent to residual displacement by lowering the ground strength. By using this method, the lining and the invert can be verified.

　2) It was confirmed that the standard invert (I_N invert) satisfies the performance when the residual displacement is set to 0.56 mm, which corresponds to the horizontal displacement rate of 1 mm/month.

　3) When 3.0 mm is set as a relatively large residual displacement, it was confirmed that performance was satisfied by adopting an invert structure (I_{NAiP} invert or I_{SiP} invert) that copes with floor heave.

References

[1] ISO2394, "General Principles on Reliability For Structure," 3rd Edition, June 1998.

[2] Eurocode, BS EN 1990 'Eurocode: Basis of structural design,' 1990.

[3] *Design Standards for Railway Structures and Commentary (Mountain tunnels)*, 2022.

[4] Shimamoto, K., Yashiro, K., Kawagoe, T., Floor Heave Mechanism and Effect of Countermeasures for Mountain Tunnels, *Quarterly Report of RTRI*, 2022, Volume 63, Issue 2, Pages 115-120, 2022.

[5] Shimamoto, K., Yashiro, K., Kojima, Y. and Asakura, T., "Prediction Method of Tunnel Deformation Using Time-dependent Ground Deterioration Model," *Quarterly Report of RTRI*, Vol. 50, No. 2, pp. 81-88, 2009.

[6] Shimamoto, K., Yashiro, K., "New rockbolting methods for reinforcing tunnels against deformation," *International Journal of Rock Mechanics and Mining Sciences*, Volume 147, 2021.

[7] Aydan, Ö., Dalgıç, S. and Kawamoto, T., "Prediction of squeezing potential of rocks in tunnelling through a combination of an analytical method and rock mass classifications," *Italian Geotechnical Journal*, 34: pp. 41-45, 2000.

[8] Jiang, Y., Ezaki, T., Yokota, Y. and Kamuro, K., Quantitative Analysis of the Ground Characteristic Curve in Tunneling, *Proceedings of the 9th Japan Symposium on Rock Mechanics*, pp. 767-772, 1994 (in Japanese).

Authors

Keisuke SHIMAMOTO, Dr. Eng.
Senior Researcher, Tunnel Laboratory,
Structure Technology Division
Research Areas: Tunnel, Mountain Tunnel,
Tunnel Maintenance

Kazuhide YASHIRO, Dr. Eng.
Senior Chief Researcher, Head of Tunnel
Laboratory, Structure Technology Division
Research Areas: Tunnel, Mountain Tunnel,
Tunnel Maintenance

Noriyuki OKANO, Dr. Eng.
Head of Geology Laboratory, Disaster
Prevention Technology Division (Former)
Research Areas: Tunnel, Mountain Tunnel,
Urban Tunnel

Trend Analysis of Segments and Tunnel Boring Machines for Railway Shield Tunnels

Kiwamu TSUNO
Structures Technology Division

Koji FUNAKOSHI   **Kiichi FUJITA**
Tunnel Engineering Laboratory, Structures Technology Division (Former)

Trends in railway tunnels constructed with the shield method were analyzed based on a database which contains 388 construction cases spanning the period 1964 to 2013. This research investigated the thickness and width of segments, number of divided segments and intervals between ring joints. Trends in parts related to shield machines were also described such as types of TBM, tail clearances between shield skin plates and segments, thickness of shield skin plates and backfill grouting.

***Key words**: shield tunnel, segment, shield machine, trend analysis*

1. Introduction

Railway shield tunnels were designed until now according to the "Design Standards for Railway Structure and commentary (Shield Tunnels)," which was published in 1997 and based on allowable stress design method. However, a revised design standard for railway shield tunnels was published in 2022. This new standard entitled "Design Standards for Railway Structure and commentary (Tunnels)" consists of four parts, namely, "Part 1 General tunneling," "Part 2 Cut-and-cover tunnel," "Part 3 Shield tunnel" and "Part 4 Mountain tunnel," and is based on a performance-based design method. The three required performances of safety, serviceability and restorability are verified in the performance-based design method, in the same way as other railway structures. The performance items for railway tunnels are listed in Table 1.

In the design of railway shield tunnels, it is required to determine parameters regarding the configuration of a tunnel cross-section, such as thickness of segments, tail clearance, thickness of skin plate of shield machines and other items as shown in Fig. 1. These values are generally investigated during a structural planning stage. The dimension of segments such as segment width, segment division and interval of ring joints and items regarding execution such as types of shield machines, a backfill grouting method and backfill grouting material are also determined during this stage. As these values are determined mainly on the basis of past experience and construction results, it is important to organize construction results according to the shape and dimension of segments and shield machines.

Consequently, this case study investigated segments and shield machines in railway shield tunnels and trends were identified [1-3]. The investigation covered 388 sections of railway shield tunnels constructed between 1964 and 2013. 6% of these sections were constructed in the 1960s, 20% in the 1970s, 15% in the 1980s, 32% in 1990s and 26% after the 2000s.

In some items, the investigation excluded 22 examples which had multi-circular or rectangular cross sections.

Table. 1 Required performance, performance items and examples of verification indices for railway tunnel

Required performance	Performance item	Verification indices
Safety	Failure	Force, displacement/deformation
	Fatigue failure	Stress intensity, force
	Stability	Force, displacement/deformation
	Running safety	Displacement/deformation of inner space, uneven displacement of track[*1], lateral vibration displacement[*1]
	Public safety	Carbonation depth, chloride ion content, types of bolts
Serviceability	Aesthetic appearance	Crack width, stress intensity
	Watertightness	Crack width, stress intensity, leakage water
	Bearing performance	Force, displacement/deformation
	Riding comfort	Uneven displacement of track[*1]
	Noise/vibration	Noise level, vibration level
Restorability	Damage	Displacement/deformation of member, Force, stress intensity, uneven displacement of track[*1], lateral vibration displacement[*1]
	Residual displacement	Force, displacement/deformation

[*1]: It is required to set this performance item in supporting trains passing on the ground.

2. Trend analysis in segment shape and dimension

2.1 Thickness of segment

The thickness of segments influences structural strength and is an important factor. While making segments thicker enlarges the structural strength, it also increases cost, weight, amount of excavated soil etc., therefore determining the most appropriate thickness is important. Figure 2 shows the relationship between the outer diameter of shield tunnels and the thickness of segments regarding flat types of RC segments. This figure also describes lines corresponding to the relationship in which the ratio of the segment thickness H to the outer diameter of tunnels D, namely H/D, is 3.5%, 4.0% and 4.5%. The thickness of segments, which is influenced by design
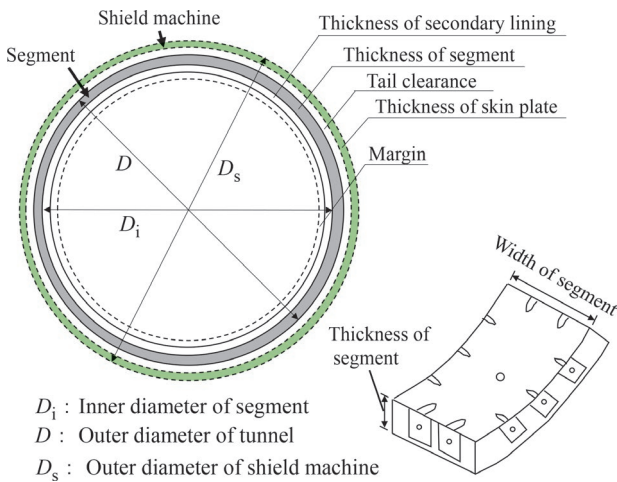
Fig. 1   Configuration of tunnel cross-section

load and varies, ranges from 250 mm to 550 mm and increases with the tunnel diameter.
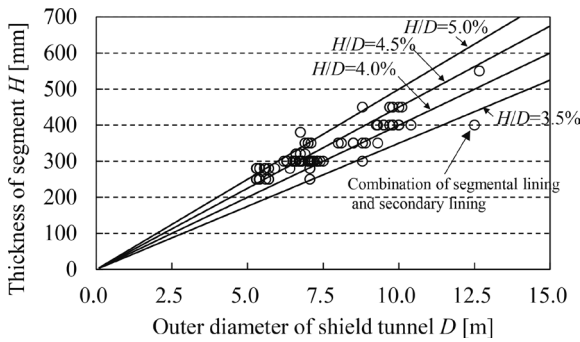

Fig. 2   Relationship between the outer diameter and segment thickness (flat type RC segment) [1]

Figure 3 shows the relationship between the outer diameter and the values of H/D and reveals that the values of H/D range from 3.4% to 5.6%, excluding the one case where the secondary lining is integrated with the segmental lining. Some values of H/D exceed 5.0% when the outer diameter is less than 7.5 m, while they below 4.5% in case of outer diameters over 10 m.
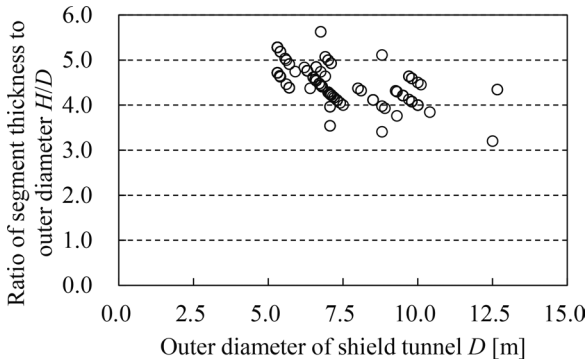

Fig. 3   Ratio of segment thickness to outer diameter (flat type RC segment) [1]

2.2 Width of segment

The larger the segment width, the more costs can be cut by reducing the number of ring joints, and the faster the construction speed. However, this also increases the weight of segments and may cause contact to occur between shield machines and segments in curved sections. Therefore, it is important to appropriately determine the width of segments.

Figure 4 shows the relationship between the outer diameter of shield tunnels and the segments width. The segment width of flat type RC segments, box type RC segments, ductile case iron segments and composite segments range from 780 to 1600 mm, from 650 to 1200 mm, from 600 to 1300 mm and from 800 to 1200 mm, respectively. Figure 5 shows the relationship between the outer diameter and the ratio of the segment width to the segment thickness (B/H) for flat type RC segments, per decade. Results show that the values of B/H tended to be larger and segment thickness relative to segment width lower, after the 2000s.
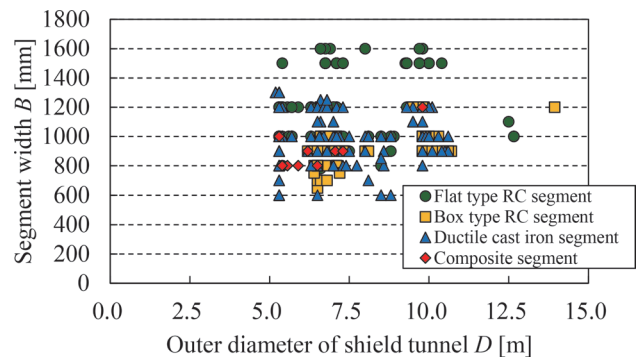
Fig. 4   Relationship between the outer diameter and segment width [1]
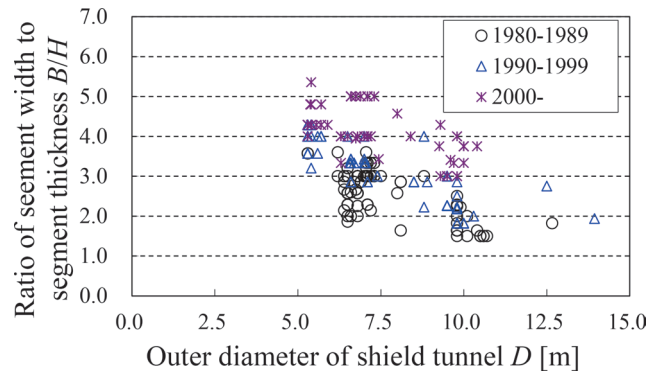
Fig. 5   Ratio of segment width to segment thickness (RC segment) [1]

2.3 Number of segment division

Figure 6 shows the relationship between the outer diameter of shield tunnels and the number of segment divisions. It shows that the number of segment divisions ranges from 5 to 13 and that of RC segment and others ranges from 6 to 13 and from 5 to 12, respectively. Results also show that the number of segments rises when the outer diameter increases.

Fig. 6 Relationship between outer diameter and number of segment divisions [2]

2.4 Interval between ring joints

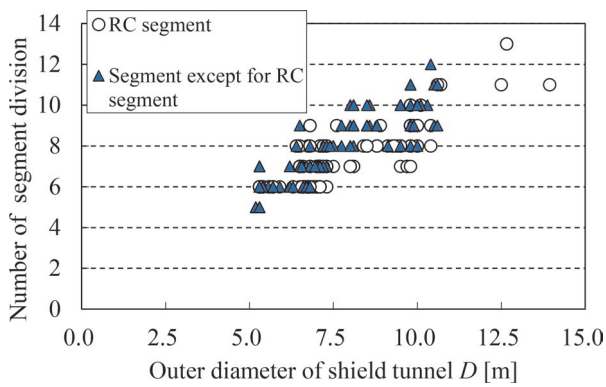Figure 7 shows the relationship between the outer diameter of shield tunnels and the interval of ring joints. The interval between ring joints in RC segments ranges from 400 to 1300 mm, concentrating in the range 800 to 1000 mm. No differences in trend were observed between flat type and box-type RC segments and there is no clear relationship with the outer diameter. The interval between ring joints in segments other than RC segments ranges from 200 to 1200 mm with 80% of data concentrated in the range 300 to 500 mm.
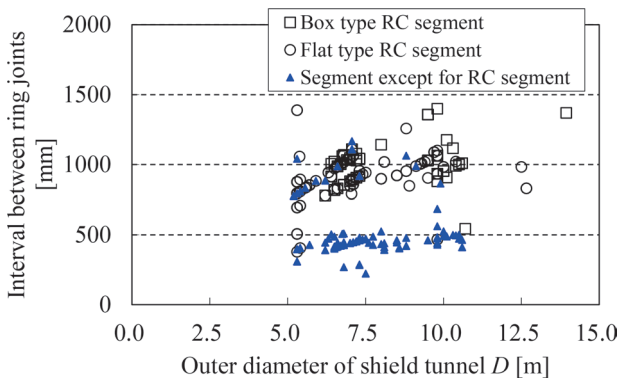

Fig. 7 Relationship between outer diameter and interval between ring joints [2]

2.5 Secondary lining

Figure 8 shows the situation with secondary linings, including the presence of secondary lining, material, and thickness, per decade except for the period 2000-2013. The percentage of installed secondary lining is comparatively high before the 1980s, while it is omitted in approximately 50% and 85% of cases in the 1990s and 2000s, respectively. In other ward, omitting secondary linings has become the norm in 2000s. Both plain concrete without reinforcing bars and RC are used in the secondary lining. The rates of plain concrete and RC were almost same before 1990s, while almost all secondary linings were made from RC in 2000s. The thickness of secondary linings is mostly 250 to 300 mm in case of secondary linings with plain concrete, while it widely varies from less than 200 mm to more than 300 mm when RC is used.
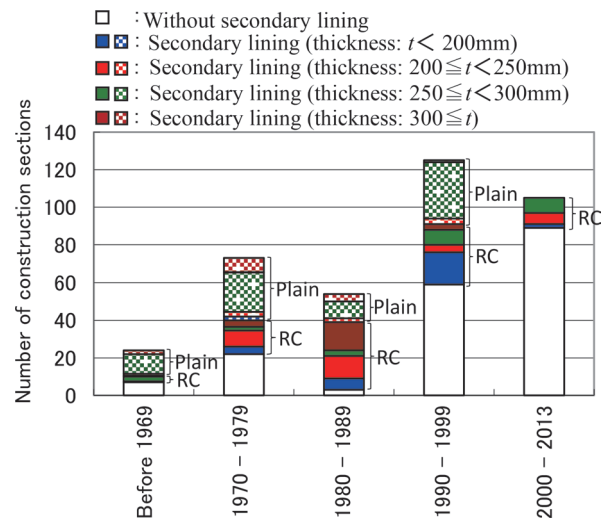
Fig. 8 Secondary lining results [3]

3. Trend analysis in shield machines

3.1 Type of shield machine

Figure 9 shows the number of every type of shield machine used in railway shield tunnels, per decade except for the period 2000-2013. Manual excavation type shield machines were mainly used before 1970s, and mechanical and blind types were used in 1970s. However, closed-face shield machines, such as slurry and earth pressure balanced ones, have been dominant since the 1980s. Slurry type shield machines were the main type of machine used in the 1980s, while earth pressure balanced shield machines dominated after the 1990s.

Fig. 9 Type of shield machine [3]

3.2 Tail clearance

Tail clearance is the space between skin plates of shield machines and segments as shown in Fig. 10 and is determined during

the structural planning stage. Figure 11 shows the relationship between the outer diameter of shield machines and the tail clearance and reveals that the tail clearance does not clearly relate to the outer diameter and ranges from 25 to 40 mm.

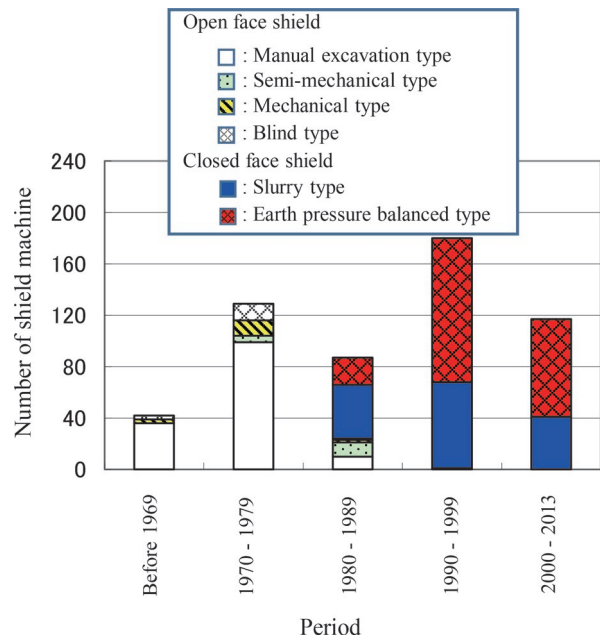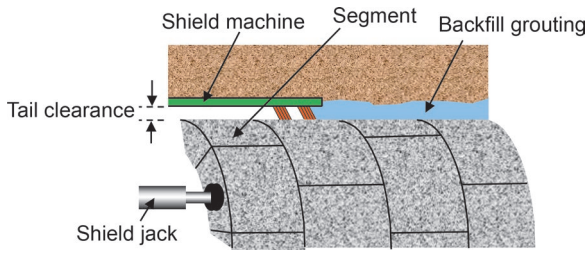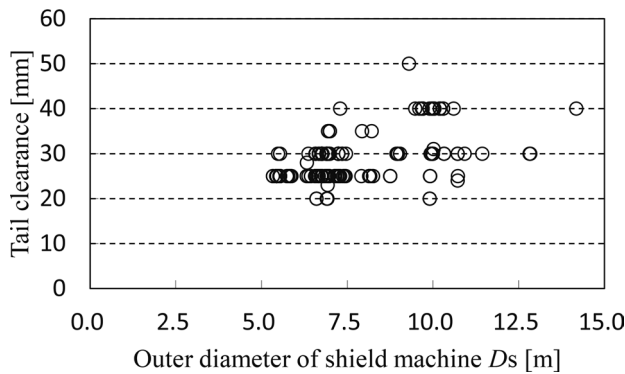**Fig. 10 Tail clearance**

Fig. 11 Relationship between outer diameter of shield machines and tail clearance [2]

3.3 Thickness of skin plate of shield machine

Skin plate thickness influences excavation cross sections and is therefore an item required to be determined during the structural planning stage. Figure 12 shows the relationship between the outer diameter of shield machines and the skin plate thickness. It ranges from 25 to 80 mm and tends to rise as the outer diameter increases.
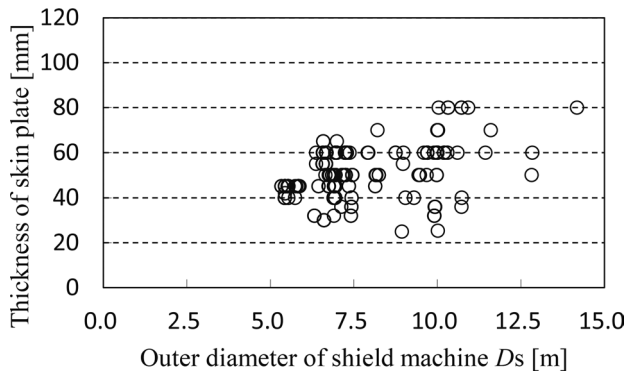

Fig. 12 Relationship between outer diameter of shield machine and skin plate thickness [2]

3.4 Backfill grouting

Backfill grouting is one of the important procedures in the shield tunnel method, where the space between segments and the

ground is filled with backfill grouting material. The method of backfill grouting is categorized into simultaneous grouting, semi-simultaneous, immediate grouting, etc. Figure 13 shows the percentage of each grouting method utilized in railway shield tunnels. In the 1980s, the rate of immediate grouting is dominant with 37%, while simultaneous and semi-simultaneous grouting appear each at a rate of approximately 20%. The rate of simultaneous grouting, which allows the tail void to be filled rapidly, is highest, accounting for 64% and 78% of cases in 1990s and 2000s, respectively.

Figure 14 classifies the backfill grouting material into one-liquid type (suspension), two-liquid type with air, two-liquid type without air and others and shows the ratio of each type per decade except for the period 2000-2013. The one-liquid type (suspension), which mainly consists of cement, accounts for 95% of the total in the 1970s, but has not been used since the 1990s. On the other hand, the two-liquid type with and without air started to be used in the 1980s and became dominant. The two-liquid type without air in particular accounts for 28% of cases in the 1980s, a rate which grows to 67% and 70% in 1990s and 2000s, respectively.
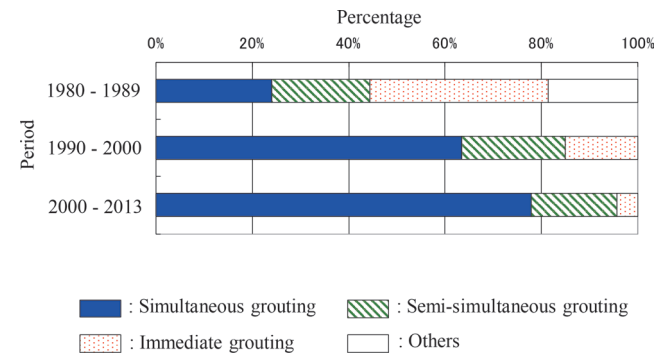
Fig. 13 Ratio of type of grout injection by time period [3]
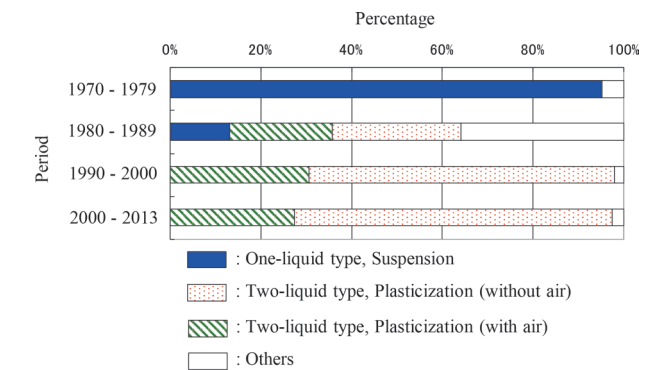
Fig. 14 Ratio of used grouting materials by time period [2]

4. Conclusions

Case studies were carried out on segments and shield machines in railway shield tunnels and to identify trends. The following results were obtained:

(1) In terms of segment shape and dimensions, the thickness of segments grows as the outer diameter of tunnels increases, and H/D values range from 3.4% to 5.6%.
(2) In terms of joints, the number of segment divisions varies between 5 to 13 and intervals between ring joints are concentrated in

the range of 800 to 1000 mm.

(3) In terms of trends in type of machine used, the rate of earth pressure balanced shield machines grew after the 1990s, and tail clearances range from 25 to 40 mm.

(4) Finally in terms of backfill grouting, simultaneous grouting and two-liquid type grouting materials without air became dominant after the 1990s.

References

[1] Tsuno, K., Funakoshi, K., Fujita, K., and Kinoshita, K., "Trend Analysis of segments for railway shield tunnels," *Proceeding of the Japan national conference on geotechnical engineering*, Vol. 53, pp. 1605-1606, 2018 (in Japanese).

[2] Funakoshi, K., Kamada, K. and Tsuno, K., "Trend Analysis of railway shield tunnel (Part 2)," *Proceedings of the symposium on underground space,* Vol. 22, pp. 17-20, 2017 (in Japanese).

[3] Tsuno, K., Murai, T., Yakita, S. and Arai, Y., "Trend Analysis of railway shield tunnel," *Proceeding of 65th annual conference of the Japan society of civil engineers*, Part VI, pp. 493-494, 2010 (in Japanese).

Authors

Kiwamu TSUNO, Dr. Eng.
Senior Researcher, Structures Technology Division
Research Areas: Maintenance of Tunnels, Design of Shield Tunnels, Subway-induced Vibration
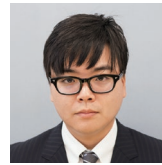
Koji FUNAKOSHI
Assistant Senior Researcher, Tunnel Engineering Laboratory, Structures Technology Division (Former)
Research Areas: Maintenance of Tunnels, Design of Shield Tunnels

Kiichi FUJITA
Researcher, Tunnel Engineering Laboratory, Structures Technology Division (Former)
Research Areas: Maintenance of Tunnels, Design of Shield Tunnels

Seismic Design Method for Shield Tunnels in Ground Conditions Subject to Change in the Longitudinal Direction

Kiwamu TSUNO
Structures Technology Division

Kiichi FUJITA   **Koji FUNAKOSHI**
Tunnel Engineering Laboratory, Structures Technology Division (Former)

The authors of this paper investigated the effect of seismic motion on shield tunnels that are located in areas with varying ground conditions. This research revealed that the larger the inclination angle of a boundary between a basic layer and a soft layer becomes, the larger the sectional forces, such as axial force, bending moment and shear force become. In addition, the sectional force obtained by an equivalent stiffness beam model was found to be larger than that obtained by a beam-spring model. This research also confirmed that results using a beam-spring model when the inclination angle is 5.9 degrees satisfy verification requirements.

1. Introduction

When shield tunnels are located in areas where the ground conditions vary in the longitudinal direction, there is a concern that they may be affected by differences of the ground displacement in the longitudinal direction during earthquakes. In this case, it is necessary to investigate the effect of seismic motion on shield tunnels. However, we have not found any cases where railway shield tunnels have been investigated on the basis of a performance-based design method. Therefore, this research created a seismic design concept for shield tunnels and investigated the effect of seismic motion on a single-track shield tunnel in the longitudinal direction. This research also examined the effects of the inclination angle of the ground boundary between basic /soft layers and structural analysis models [1].

2. Arrangement of seismic design concept for shield tunnels [2]

2.1 Shield tunnels susceptible to earthquakes

Since shield tunnels are arch-shaped structures surrounded by the ground and are thus unlikely to experience brittle failure, and behave in a way which is similar to the surrounding ground, the effect of inertial force is to be small. Therefore, the effect of earthquakes on shield tunnels is not considered to be significant. The design standard for railway structures and commentary (Tunnel, Shield) describes that performance verification required regarding shield tunnels that are susceptible to earthquakes like in locations where:

   1) Cross-section and stiffness significantly change in the tunnel longitudinal direction;
   2) Ground conditions change locally;
   3) Cover depth suddenly changes;
   4) There is a significantly steep curved section;
   5) There is soft ground and large displacement can be expected during earthquakes;
   6) Ground liquefaction may occur during earthquakes.

It is necessary to investigate the effect of seismic motion in the longitudinal direction for 1) to 4).

2.2 Required performance and performance verification

Table 1 shows whether each performance item requires direct verification or not, showed in the design standard for railway structures and commentary (Tunnel, Shield). Performance items for safety are failure, stability and running safety, while those for restorability are damage and residual displacement. Running safety (vibration displacement in the lateral direction, unequal track displacement) and residual displacement (floating) are deemed to be verified by checking other performance items. Therefore, three performance items namely safety (failure), running safety (displacement or deformation of inner space) and restorability (damage) are all that is required to be verified when there is no possibility of liquefaction. Performance items requiring direct verification are safety (failure) and running safety (displacement or deformation of inner space) when restorability is not set; they are restorability (damage) and running safety (displacement or deformation of inner space) when restorability is set.

Table 1 Example of verification for shield tunnels susceptible to earthquakes

Required performance	Performance items		Verification	
			○: Performance items requiring direct verification. △: Performance items that may be assumed to satisfy verification by satisfying preconditions etc.	
Safety	Failure		○	In case of bending failure: damage level 3 In case of shear failure: damage level 1
	Stability (floating)		△	Set when liquefaction may occur
	Running safety	Displacement or deformation of inner space	○	Deemed to be verified by checking that member does not yield against Level-1 earthquake motion
		Vibration displacement in lateral direction, Unequal track displacement	△	Deemed to be verified by checking the other required performance except for running safety under seismic motion
Restorability	Damage to members		○	In case of bending failure: damage level 2 In case of shear failure: damage level 1
	Residual displacement (floating)		△	Deemed to be verified by checking the verification of safety (stability) under seismic motion

2.3 Safety factor

Safety factors are determined based on the design standard for railway structures and commentary (Tunnel, Shield). Table 2 shows safety factors during earthquakes used in this research.

Table 2 Safety factor

Action factor γ_f	Structural analysis factor γ_a	Material factor γ_m		Member factor γ_b			Structure factor γ_i
		Segment γ_c	Reinforced bar γ_f	Bending	Shear		
					Segment	Re-bar	
1.0	1.0	1.2	1.0	1.0	1.3	1.1	1.0

3. Seismic studies in areas with changes in ground condition

Seismic studies in the tunnel longitudinal direction were carried out, assuming 2) of the six conditions listed in the section 2.1 applies.

3.1 Subject of investigation

The subject of investigation was a single-track shield tunnel (the outer diameter of tunnel: 6.6 m, the thickness of segment: 300 mm) located in an area where ground conditions change significantly. Table 3 shows the specifications of the subject shield tunnel. As shown in Fig. 1, the tunnel was supposed to be located on the ground whose condition changed from a bedrock layer (shear wave velocity $V_s = 400$ m/s) to a sandy layer (shear wave velocity $V_s = 230$ m/s), and three cases were set to be investigated in which the inclination angle of stratigraphic boundary is 5.9 degrees (1:10.0), 10.9 degrees (1:5.2) and 15.6 degrees (1:3.6). The depth of cover is 15 m.

Restorability was set as a performance requirement in addition to safety, under the assumption that there is no possibility of liquefaction. It was also assumed that the shield tunnel was confirmed to have members which would not yield to Level-1 earthquake motion, satisfying running safety (displacement or deformation of inner space). Therefore, subsequent performance verification was conducted only for restorability (damage).

In this case, the damage level must be kept within level 2 in the case of bending failure and within level 1 in the case of shear failure. Table 4 shows the repair methods for the corresponding damage levels.

Table 3 Specification of shield tunnel

Tunnel outer diameter D_o [m]	6.6
Segment thickness h [mm]	300
Segment width B [m]	1.2
Design standard strength f'_{ck} [N/mm^2]	48
Bolt of ring joints	M30 (8.8) 26pcs
Arrangement of reinforcing bars	D10 @ 166

3.2 Structural analysis model

The equivalent stiffness replacement beam model (Fig. 2) and the longitudinal beam-spring model (Fig. 3) are used in seismic studies in the tunnel longitudinal direction.

The equivalent stiffness replacement beam model (Fig. 2) is a model in which the beam is replaced by a beam with uniform stiffness equivalent to that of a shield tunnel in the longitudinal direction, taking into account the reduction in bending stiffness due to ring joints. The axial and bending stiffness are determined by means of equations (1) to (3) [2].
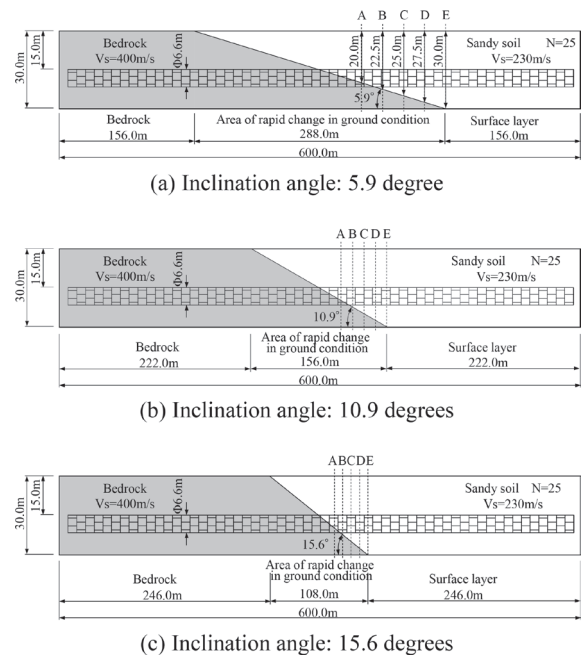

(a) Inclination angle: 5.9 degree

(b) Inclination angle: 10.9 degrees

(c) Inclination angle: 15.6 degrees

Fig. 1 Ground condition of investigation

Table 4 Image of repair method for corresponding damage levels

(a) Bending failure

	Damage level	Example of repair/ restoration method
Damage level 1	No damage	No repair (durability considered as necessary)
Damage level 2	Damage that may require repair depending on situation	Crack injection/ cross-section repair/ repair of joints, if necessary
Damage level 3	Damage requiring repair	Inner reinforcement with e.g., steel plates, additional secondary lining
Damage level 4	Damage requiring repair, and replacement of members depending on situation	Inner reinforcement with e. g. steel plates/ additional secondary lining/ replacement of members in case of significant tunnel deformation

(b) Shear failure

|	Damage level	Example of repair/ restoration method
Damage level 1	No damage	No repair (durability considered as necessary)
Damage level 4	Damage requiring repair, and replacement of members depending on situation	Crack injection/ inner reinforcement with e. g., steel plates/ additional secondary lining/ replacement of members in case of significant tunnel deformation
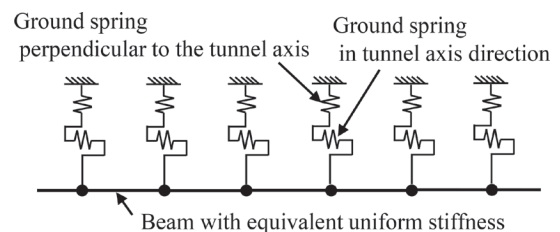
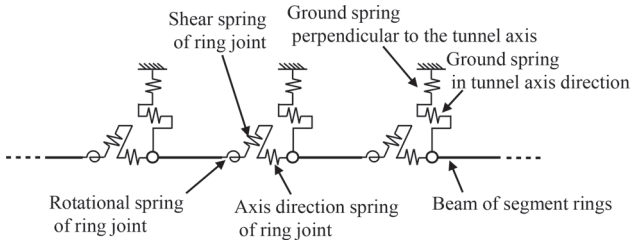**Fig. 2 Equivalent stiffness replacement beam model**

Fig. 3 Longitudinal beam-spring model

[Equivalent axial stiffness]

Compression: $(EA)_{eq}^c = EA$ (1)

Tension: $(EA)_{eq}^T = \dfrac{k_u}{k_u + EA / b} \times EA$ (2)

[Equivalent bending stiffness]

$$(EI)_{eq} = \frac{\cos^3\phi}{\cos\phi + (\pi / 2 + \phi)\sin\phi} \times EI \qquad (3)$$

where ϕ = factor satisfying the following equation

$$\frac{\cos\phi + \phi}{\pi} = \frac{1}{2} + \frac{k_u b}{EA}$$

A: $A = \dfrac{\pi(D_0^2 - D_1^2)}{4}$;

I: $I = \dfrac{\pi(D_0^4 - D_1^4)}{64}$;

  b: segment width;
D_0: outer diameter of segment ring;
D_1: inner diameter of segment ring;
 E: Young's modulus of segments; and
 k_u: spring constant of ring joint surface ($k_u = k_{ru} \times n_r$, k_{ru}: spring constant of one ring joint, n_r: number of ring joints for one ring).

On the other hand, the longitudinal beam-spring model (Fig. 3) models consists of segment rings as beams and ring joints as axial, rotation and shear springs, as shown in Fig. 3. The model can take into account the reduction of stiffness in the longitudinal direction caused by the ring joints and enables to obtain their sectional force and an amount of opening directly. This research proposed a method for modelling a shield tunnel in the longitudinal direction as shown in Table 5 [1]. Nonlinear characteristics of bending stiffness of segment rings were taken into account by assuming RC toroidal cross-sections regarding distributing bars as main bars.

Ring joints have axial stiffness (compression and tension), bending stiffness (rotational stiffness) and shear stiffness. Axial stiffness (compression) is assumed to be infinite, considering that compressive force is transferred between the concrete of adjacent segment rings. Axial stiffness (tension) and bending stiffness (rotational stiffness) are modeled, by regarding the ring joint as a structure consisting of a joint bolt and a joint plate as shown in Fig. 4, calculating the displacement-load relationship of a single joint and convoluting it on the number of joints. The axial stiffness (tension) is calculated by multiplying the displacement-load relationship of a

Table 5 Modeling of shield tunnel in longitudinal direction (Longitudinal beam-spring model)

Member	Stiffness		Beam-spring model in longitudinal direction
Segment ring	Stiffness in axis direction	Compression	EA
		Tensile	EA
	Bending stiffness		Non-linear $(M\text{-}\phi)$ ※1
Ring joint	Stiffness in axis direction	Compression	Rigid (∞)
		Tensile	Determine based on joint bolts and joint plates
	Bending stiffness (Rotational spring)		Determine based on joint bolts and joint plates
	Shear stiffness		Rigid (∞)

※1：Hypothetical RC circular cross-section regarding distributing re-bar as main re-bar

single joint by the number of joints. The bending stiffness (rotational stiffness) is calculated by adding up the moment of each joint, assuming that the opening between segments occurs at the edge of segments as shown in Fig. 5, taking into account that the displacement varies depending on the position of each joint. The axial stiffness (tension) and bending stiffness (rotational stiffness) are modeled using a bilinear model having the first and second gradient as shown in Fig. 6, in which nonlinear characteristics are considered by taking into account the yield and full-section plasticity of joints. The shear stiffness is assumed to be infinite, considering that the shear force is transferred by friction between the concrete of adjacent segment rings.

3.3 Interaction between ground and tunnel

The interaction between the ground and tunnels is modeled as the ground spring in both the equivalent stiffness replacement beam model and the longitudinal beam-spring model. The ground reaction coefficients are calculated with equations (4) and (5), using the calculation method of the ground reaction coefficient in the cross-sectional direction.

$$k_v = 1.7\alpha E_0 B_v^{-3/4} \qquad (4)$$

where k_v: vertical ground reaction coefficient in the upper and lower slab direction (kN/m³);
α : correction factor for calculation method of E_0 and loading condition;
E_0: deformation coefficient of ground (kN/m²); and
B_v: conversion width (m) in the upper and lower slab direction, and

$$k_{sv} = k_v / 3 \qquad (5)$$

where k_{sv}: shear ground reaction coefficient in the upper and lower slab direction (kN/m³)

The conversion width B_v is set to be $\sqrt{2}R$ (R: tunnel outer diameter) by assuming that the ground reaction distributes within 90 degrees from the center of the shield tunnel considering its circular shape.

The deformation coefficient of the ground E_0 is obtained from the results of the one-dimensional ground response analysis described below by converting from shear stiffness G when the ground response reaches a maximum and varies along the locations in the tunnel longitudinal direction.
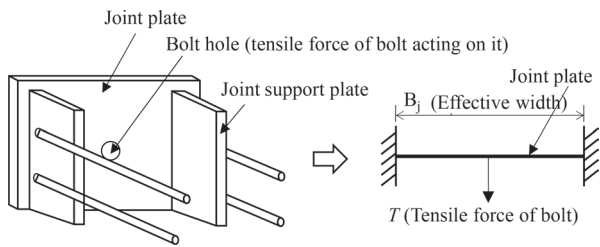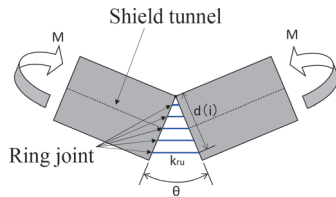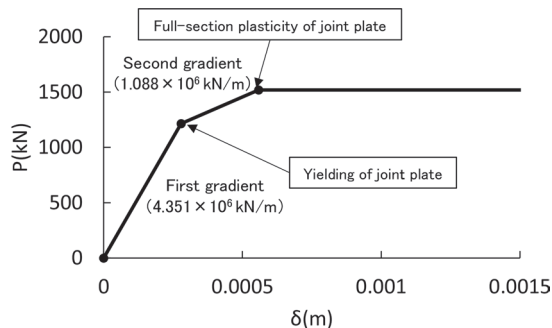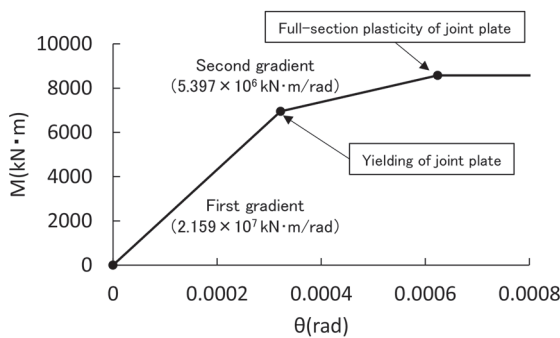
Fig. 4　Modeling of ring joint

Fig. 5　Concept of bending stiffness (rotational spring) setting

(a) Tensile characteristics

(b) Bending characteristics

Fig. 6　Spring characteristics of ring joint

3.4　Calculation of response value

A possible method for calculating response values is to perform dynamic analysis with a model that integrates the ground and the shield tunnel. However, it is difficult to conduct such dynamic analysis because shield tunnels have a lot of joints and the calculation model becomes very complicated in the seismic studies in the tunnel longitudinal direction. Therefore, this research applies the response displacement method, in which the ground displacement obtained by the one-dimensional ground response analysis is input to the structural analysis model via the ground springs.

3.4.1　One-dimensional ground response analysis

The one-dimensional ground response analysis (time history response analysis using the sequential analysis method) was performed for five cross sections A to E in Fig. 1 to calculate the ground displacement in the direction perpendicular to the tunnel axis at each tunnel location. A GHE-S model was used to take into account the nonlinear characteristics of the relationship between stress τ and strain γ of soil. The boundary condition between the surface layer and bedrock one was modeled as a dashpot. For design seismic motion, L2 Spectrum II (G1 ground) in the design standard for railway structures and commentary (seismic design) [3] was used. The maximum values of displacement in the direction perpendicular to the tunnel axis at the spring line (SL) were calculated from the results of the one-dimensional ground response analysis as shown in Fig. 7. The distribution of the ground displacement to be input was calculated based on the obtained maximum values of displacement as shown in Fig. 8.
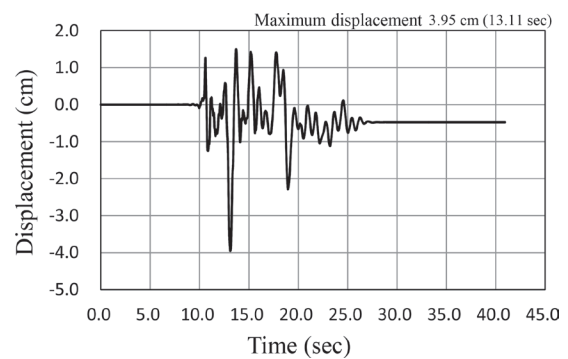
Fig. 7　Example of ground response analysis result (Section A)
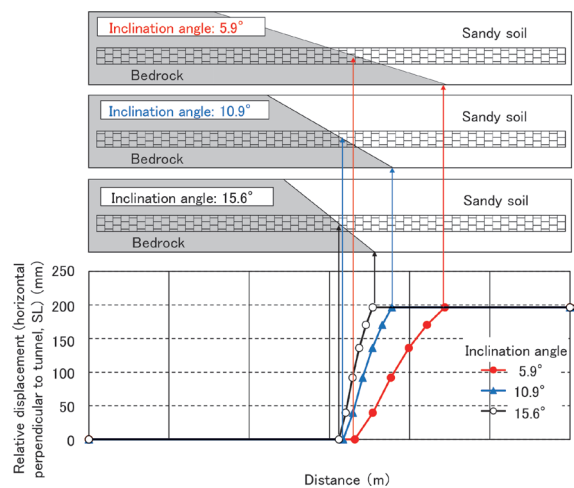
Fig. 8　Input ground displacement (Time: 14.2 s)

3.4.2　Structural analysis in longitudinal direction

The ground displacement obtained from the one-dimensional ground response analysis was input to the structural analysis model in the longitudinal direction, and the design response values during an earthquake were calculated. For the structural analysis model, the equivalent stiffness replacement beam model and the longitudinal beam-spring model shown in Section 3.2 were used, creating analytical models of 600 m in length. The ground displacement between each adjacent cross section from A to E was input by linearly inter-

polated data between the results of the adjacent cross sections.

3.4.3 Calculation result of response value

Figure 9 shows the axial force in the tunnel longitudinal direction obtained by the structural analysis. The maximum compressive axial force tends to be larger and the convex shape sharper as inclination angles become larger. The compressive axial force obtained by the longitudinal beam-spring model is almost the same as that by the equivalent stiffness replaceme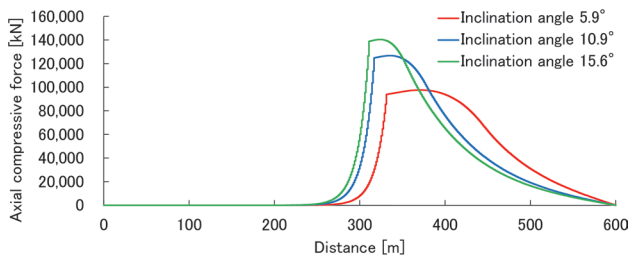nt beam model. This can be attributed to the fact that the segment main parts receive the compression force and the axial compressive stiffness of the segment main part is the same in both models.
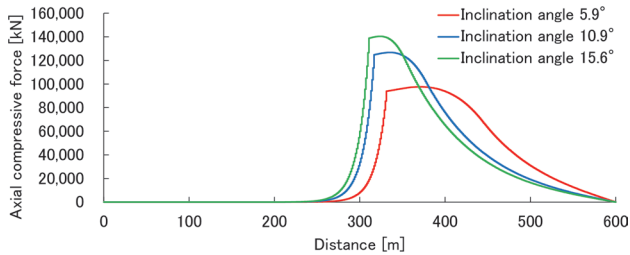
(a) Equivalent stiffness beam model

(b) Longitudinal beam-spring model

Fig. 9 Compressive axial force

The horizontal bending moment is shown in Fig. 10. It was found that the horizontal bending moment tends to be large near the area of rapid change in the ground condition and that the maximum bending moment becomes large with the inclination angle. The maximum values of horizontal bending moment obtained by the equivalent stiffness replacement beam model are 1.9 to 3.2 times larger than those obtained with the longitudinal beam-spring model.

The horizontal shear force is shown in Fig. 11. The horizontal shear force tends to be large with the inclination angle as with the horizontal bending moment. The maximum values of horizontal shear force obtained by the equivalent stiffness replacement beam model are 1.6 to 2.7 times larger than those obtained with the longitudinal beam-spring model.

As described above, it is ascertained that the horizontal bending moment and horizontal shear force obtained using the equivalent stiffness replacement beam model tend to be larger than those obtained using the longitudinal beam-spring model.

3.4.4 Verification result

Verification results obtained by the equivalent stiffness replacement beam model and the longitudinal beam-spring model are shown in Table 6 and Table 7, respectively. In this research, the
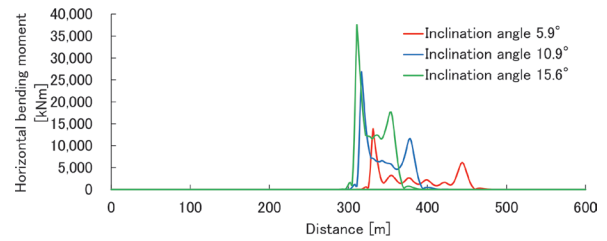
(a) Equivalent stiffness beam model
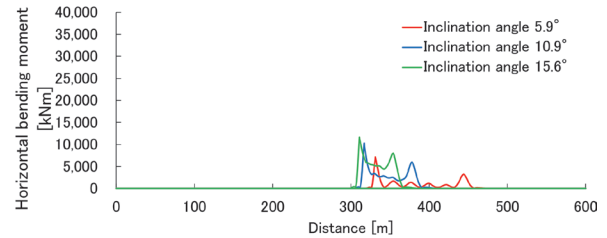
(b) Longitudinal beam-spring model

Fig. 10 Horizontal bending moment
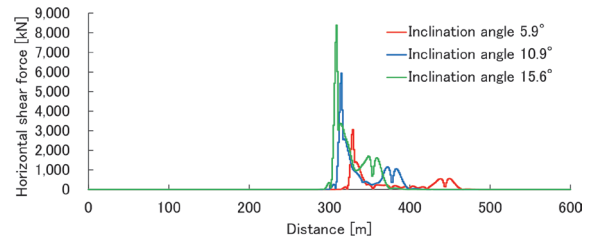
(a) Equivalent stiffness beam model
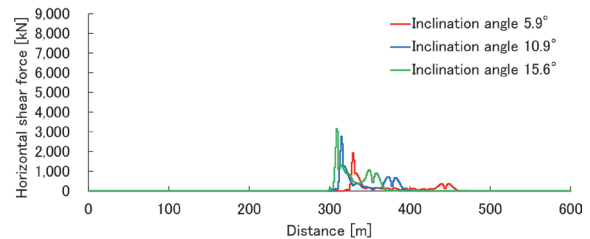
(b) Longitudinal beam-spring model

Fig. 11 Horizontal shear force

same joint parameters are used to compare the verification values for each case and verification item. In this case, the ring joint parameters are set to satisfy the verification using the beam-spring model for an inclination angle of 5.9°. Therefore, other cases do not satisfy the verification. The results show that the equivalent stiffness replacement beam model does not satisfy the verification for ring joints even when the inclination angle is 5.9°. On the other hand, when the longitudinal beam-spring model is used, the verification is satisfied at an inclination angle of 5.9°, and the ring joints did not satisfy the verification at larger inclination angles of 10.9° or 15.6°. It was found that the effect of the ground displacement increases when the inclination angle is steep, and that the use of the longitudinal beam-spring model may allow us to make a rational study.

Comparing each verification value for the longitudinal beam-spring model, the verification values for the horizontal bending

Table 6 Verification result (Equivalent stiffness beam model)

	Verification item		Inclination angle 5.9°	Inclination angle 10.9°	Inclination angle 15.6°
Segment	Axial compressive force N_{cmax}	(kN)	97,636	126,781	140,428
	Axial compressive bearing force N_{cu}	(kN)	201,878	201,878	201,878
	$\gamma \, i \cdot N_{cmax}/N_{cu}$	—	0.48	0.63	0.7
Ring joint	Axial tensile force N_{tmax}	(kN)	9,699	16,086	20,886
	Axial tensile bearing force N_{tu}	(kN)	7,501	7,501	7,501
	$\gamma \, i \cdot N_{tmax}/N_{tu}$	—	1.29	2.14	2.78
	Horizontal bending moment M_{hmax}	(kN·m)	13,830	26,849	37,556
	Bending bearing force M_{ud}	(kN·m)	8,579	8,579	8,579
	$\gamma \, i \cdot M_{hmax}/M_{ud}$	—	1.61	3.13	4.38
	Horizontal shear force S_{hmax}	(kN)	3,051	5,943	8,388
	Shear bearing force S_{u}	(kN)	4,812	4,812	4,812
	$\gamma \, i \cdot S_{hmax}/S_{u}$	—	0.63	1.24	1.74

Table 7 Verification result (Longitudinal beam-spring model)

	Verification item		Inclination angle 5.9°	Inclination angle 10.9°	Inclination angle 15.6°
Segment	Axial compressive force N_{cmax}	(kN)	97,636	126,781	140,428
	Axial compressive bearing force N_{cu}	(kN)	201,878	201,878	201,878
	$\gamma \, i \cdot N_{cmax}/N_{cu}$	—	0.48	0.63	0.7
Ring joint	Axial tensile force N_{tmax}	(kN)	3,844	5,972	7,754
	Axial tensile bearing force N_{tu}	(kN)	7,501	7,501	7,501
	$\gamma \, i \cdot N_{tmax}/N_{tu}$	—	0.51	0.80	1.03
	Horizontal bending moment M_{hmax}	(kN·m)	7,138	10,256	11,630
	Bending bearing force M_{ud}	(kN·m)	8,579	8,579	8,579
	$\gamma \, i \cdot M_{hmax}/M_{ud}$	—	0.83	1.20	1.36
	Horizontal shear force S_{hmax}	(kN)	1,926	2,772	3,154
	Shear bearing force S_{u}	(kN)	4,812	4,812	4,812
	$\gamma \, i \cdot S_{hmax}/S_{u}$	—	0.40	0.58	0.66

moment at the ring joint are larger.

4. Conclusions

This research developed a seismic design concept for shield tunnels and investigated the influence of seismic motion in the longitudinal direction on a single-track shield tunnel located in areas with changing the ground conditions by using the performance-based design method. The following results were obtained:

(1) Maximum values of compressive axial force, horizontal bending moment and horizontal shear force tend to be larger with the inclination angle of the boundary between the bedrock and surface layer for shield tunnels located in areas with changing ground condition.

(2) Horizontal bending moments and horizontal shear forces obtained by the equivalent stiffness replacement beam model tend to be larger than that by the longitudinal beam-spring model. The maximum values of horizontal bending moment and shear force obtained by the equivalent stiffness replacement beam model are 1.9 to 3.2 times and 1.6 to 2.7 times as large as those by the longitudinal beam-spring model, respectively. It was found that the use of the longitudinal beam-spring model may allow for a rational study.

References

[1] Funakoshi, K., Fujita, K., and Tsuno, K., "Seismic design of shield tunnel located in the ground change point in the longitudinal direction," *Proceeding of the Japan national conference on geotechnical engineering*, Vol. 54, pp. 1429-1430, 2019 (in Japanese).
[2] Ministry of Land, Infrastructure, Transport and Tourism and Railway Technical research institute, *Design Standards for Railway Structures and Commentary (Tunnel, shield)*, Maruzen Publishing Co., Ltd., pp. 235-236, 2022 (in Japanese).
[3] Ministry of Land, Infrastructure, Transport and Tourism and Railway Technical research institute, *Design Standards for Railway Structures and Commentary (Seismic Design)*, Maruzen Publishing Co., Ltd., p. 47, 2012 (in Japanese).

Authors

Kiwamu TSUNO, Dr. Eng.
Senior Researcher, Structures Technology Division
Research Areas: Maintenance of Tunnels, Design of Shield Tunnels, Subway-induced Vibration

Kiichi FUJITA
Researcher, Tunnel Engineering Laboratory, Structures Technology Division (Former)
Research Areas: Maintenance of Tunnels, Design of Shield Tunnels

Koji FUNAKOSHI
Assistant Senior Researcher, Tunnel engineering, Structures Technology Division (Former)
Research Areas: Maintenance of Tunnels, Design of Shield Tunnels

Improvement in Rapidness of Earthquake Early Warning Using Ocean Bottom Seismic Data

Shunta NODA   Naoyasu IWATA

Seismic Data Analysis Laboratory, Center for Railway Earthquake Engineering Research

This study proposes an earthquake early warning (EEW) method for ocean bottom seismic (OBS) data systems of railways. Because the conventional Shinkansen systems adopts only the S-wave alarm method for the OBS data, we demonstrate that the P-wave alarm method can estimate epicentral distance and magnitude using the OBS data but cannot accurately determine back azimuth. Considering this, we propose a concrete method for how to judge whether a warning is issued applying the OBS data. The proposed method enables us to improve the rapidness of EEW and the safety of railways during earthquakes.

***Key words**: ocean bottom seismic data, earthquake early warning, P-wave alarm*

1. Introduction

As a countermeasure for earthquakes, Japan's high-speed railways (Shinkansen) use an early earthquake warning (EEW) system [1]. Each railway company owns seismometers for this system, which can output an alarm to trains based on seismic source parameters (epicentral distance, back azimuth and magnitude) estimated from the initial P-wave data (hereinafter referred to as P-wave alarm) and an alarm when a measured seismic-intensity index value exceeds a threshold (hereinafter, S-wave alarm; the reason we use "S wave" is because the threshold is usually set high enough to be exceeded during S wave). The decision to suspend train operations is based on the two alarm methods. The system also employs EEW alerts published from the Japan Meteorological Agency (JMA) to enhance its redundancy [2]. Recently, to increase the rapidness of warnings for earthquakes that occur in offshore areas, the railway companies started to receive the ocean bottom seismic (OBS) data observed by the Seafloor Observation Network for Earthquakes and Tsunamis along the Japan Trench (S-net) and the Dense Ocean-floor Network System for Earthquakes and Tsunamis (DONET) from the National Research Institute for Earth Science and Disaster Resilience (NIED) [3, 4]. Figure 1 shows the distribution of S-net and DONET seismic stations.

Collaborating with the railway companies and the NIED to use the OBS data for issuing alerts to Shinkansen trains, Railway Technical Research Institute (RTRI) developed an alarm method and data transmission rules and updated the Shinkansen EEW system in order to receive and analyze the OBS data [5]. Because the number of records observed by the networks was limited at the time of the development, the method only used the S-wave alarm and not the P-wave alarm. It should be noted that the P-wave alarm method requires a detailed study based on a large amount of data. The current S-wave alarm method uses a method called fixed-section control. In this control procedure, when a large threshold exceedance is detected at a single station, a warning is output to a predefined range along the railway line close to that observation station. To increase the speed of the warning, it is effective to use a P-wave alarm method that utilizes information about P waves which propagate faster than S waves.

In this study, to increase the rapidity of the EEW methodology using seafloor seismometer information, we tested the P-wave alarm method using OBS data from a single station to propose a concrete technique for how to determine whether a warning is issued.
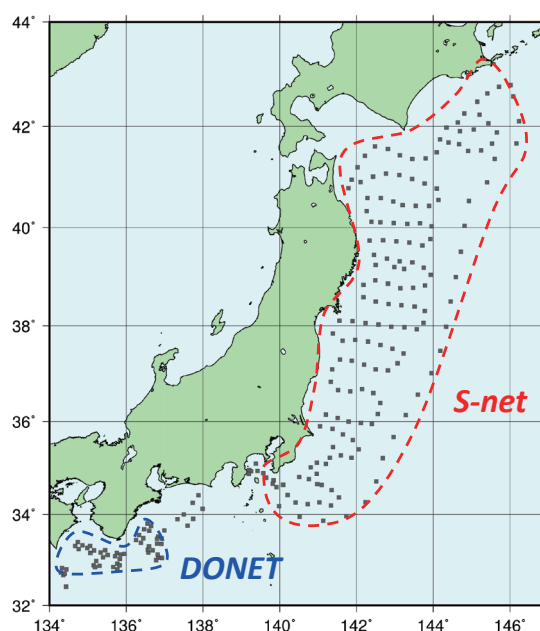

Fig. 1 **Distribution of the ocean bottom seismometers around Japan. S-net and DONET are denoted by the red and blue dashed lines, respectively.**

2. P-wave alarm method using ocean bottom seismic data

As mentioned in chapter 1, the conventional EEW system for Shinkansen does not use the P-wave alarm method in the warnings based on the OBS observation. Using OBS records, we therefore determine the parameters in the EEW algorithm that utilizes P-wave data and verify the estimation accuracy in Section 2.1. Then, we propose a practical technique for the P-wave warning in Section 2.2.

2.1 Estimation accuracy of seismic source parameters

The seismometers deployed on land for the Shinkansen EEW system estimate seismic source parameters analyzing observed seismograms immediately after the P-wave onset [6]. The source parameters are epicentral distance (Δ), back azimuth (θ) and magnitude (M), which are estimated using the C-Δ method [7], principal component analysis [8] and ground motion attenuation relation [9], respec-

tively. The train-control range is determined using the M-Δ diagram from the three source parameters [10]. We apply the three techniques for $\varDelta$, θ and M, which have been used so far for data observed on land, to OBS records to verify the estimation accuracies of the parameters. The dataset used here consists of 6,908 waveforms, in which the JMA magnitude (Mj) ranges from 4.1 to 7.4 and the epicentral distance is within 200 km, observed by S-net and DONET.

2.1.1 Back azimuth

Figure 2 shows the frequency distribution of errors in estimating back azimuth θ. Noda et al. demonstrated that the principal component analysis could provide the frequency of near 0 degrees with the highest in cases where data recorded on land were used [8]. On the other hand, Fig. 2 shows that the errors are distributed with comparable frequency, indicating that the accuracy derived from the OBS data is low. We consider that this may be because the seabed where the seafloor seismographs are installed is extremely soft, so that the incident angle of incoming seismic waves on the seismometers is nearly 0 degrees. In other words, it is hard to find sensitivity in back azimuth estimation using principal component analysis of particle motion in the horizontal direction. Therefore, in Section 2.2 we propose a technique which enables us to publish an earthquake alarm without back azimuth information.

2.1.2 Epicentral distance

Epicentral distance $\varDelta$ is determined using the C-Δ method which utilizes a negative correlation between $\varDelta$ and the parameter C representing the slope of the initial P-wave motion [6, 7]. Figure 3 in which Log represents the common logarithm showing the relationship between Log$\varDelta$ calculated from the JMA epicenter locations (horizontal axis) and Log$C$ (vertical axis) computed using the OBS records, demonstrating that the negative correlation can be found when Log$\varDelta$ is small. On the other hand, the significant correlation in the range of small Log$\varDelta$ disappears when $\varDelta$ is above approximately 100 km. Concretely, saying, the data is distributed parallel to the horizontal axis. Therefore, the upper limit for applying seafloor data to estimate epicentral distance is set at 100 km in the analysis shown below.

Odaka et al. found the negative correlation between Log$\varDelta$ and Log$B$ (another parameter of representing the initial P-wave slope) examining waveforms observed at stations on land of $\varDelta$ < about 150 km while the correlation was not observed at more distant stations [11]. In addition, Odaka et al. indicated that this was because the initial P-wave motion might be affected by head waves refracted from
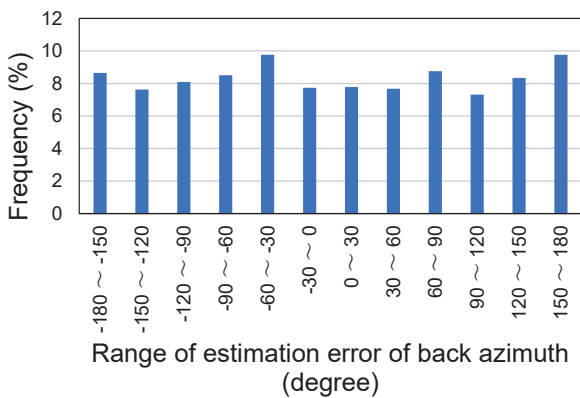
the Mohorovičić discontinuity at the stations of $\varDelta$ > about 150 km, rather than direct waves emitted from the source. The reason why this study finds 100 km the upper limit of the significant correlation can be that the crustal structures are different between land and sea areas. That is to say, the Mohorovičić discontinuity under the ocean floor is shallower than beneath the land, suggesting that the effects of head waves can be more apparent in the sea at shorter distances.

Figure 4 presents the distribution between Log$C$ and Log$\varDelta$ and a regression equation between the parameters (the blue dotted line) when the upper limit of the applied epicentral distance is 100 km. The regression equation obtained by the linear least squares method is;

$$LogC = -1.0 * Log\varDelta + 1.687 - 0.008819 * \varDelta \qquad (1)$$

The result obtained with the dataset of the ocean bottom seismographs for $\varDelta \leq 100$ km by (1) revealed that the root mean square of the estimation error in logarithm (RMSLE) is 0.299. This is almost equivalent with the one of which the records observed by the Kyoshin-NET (K-NET; installed on land) operated by the NIED are analyzed [6]. We conclude that the $\varDelta$ estimation from the OBS data of $\varDelta \leq 100$ km is sufficiently accurate for the use in EEW.
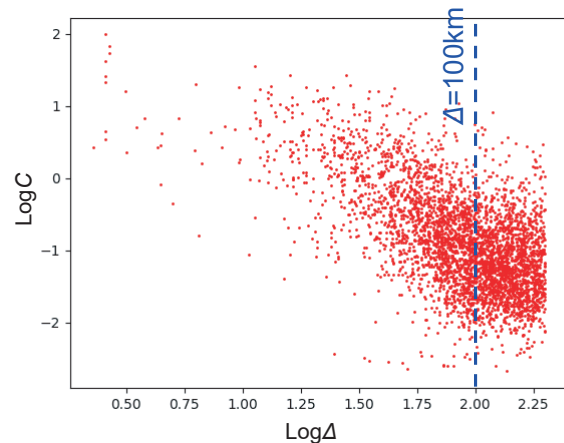
Fig. 3 Relationship between LogΔ (horizontal axis) and LogC (vertical axis) with the OBS data of Δ < 200 km.

Fig. 2 Frequency of estimation error for back azimuth θ using the OBS dataset.

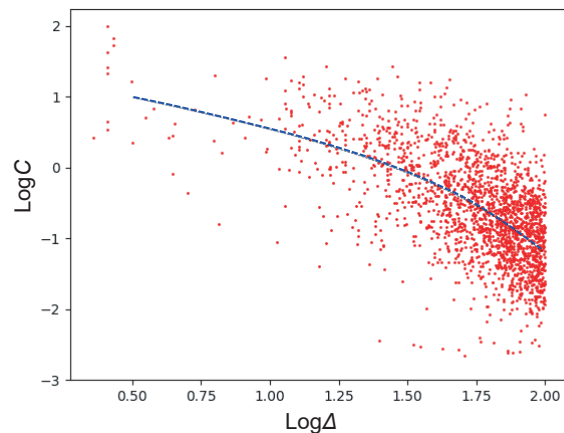**Fig. 4 Relationship between LogΔ (horizontal axis) and LogC (vertical axis) with the OBS data of Δ < 100 km. The blue dotted line shows equation (1).**

2.1.3 Magnitude

The conventional P-wave alarm method in the Shinkansen EEW system makes use of four kinds of ground motion attenuation relations to determine magnitude M [6]. The four relations are derived from four different peak amplitudes of ground motion intensities; P-wave acceleration, P-wave displacement, S-wave acceleration and S-wave displacement. A trade-off is found between the intensities, that is, using the acceleration measurements can produce a faster alert than that of displacements whereas the estimation from the displacements should be more accurate [6]. We develop ground motion attenuation relations from the linear least squares method to estimate M for using the OBS data;

$$M_{ap} = 0.6249 * \mathrm{Log}A_{u\max} + 0.3184 * \mathrm{Log}\varDelta + 4.195 + 0.006012 * \varDelta \qquad (2)$$

$$M_{dp} = 0.6008 * \mathrm{Log}D_{u\max} + 0.3696 * \mathrm{Log}\varDelta + 5.715 + 0.001972 * \varDelta \qquad (3)$$

$$M_{as} = 0.6500 * \mathrm{Log}A_{3\max} + 0.2703 * \mathrm{Log}\varDelta + 3.719 + 0.003947 * \varDelta \qquad (4)$$

$$M_{ds} = 0.6246 * \mathrm{Log}D_{3\max} + 0.3831 * \mathrm{Log}\varDelta + 5.074 + 0.0003323 * \varDelta \qquad (5)$$

where M_{ap}, M_{dp}, M_{as}, and M_{ds} are magnitudes of P-wave acceleration and displacement, S-wave acceleration and displacement, respectively, and $A_{u\max}$ $D_{u\max}$ $A_{3\max}$ and $D_{3\max}$ are the peak amplitudes in up-down component acceleration and displacement, three-component composite acceleration and displacement, respectively. Note that only the seafloor data of $\varDelta \leq 100$ km is used in the development of the equations.

The root mean squares of the estimation error (RMSEs) of M using the OBS waveforms of $\varDelta \leq 100$ km from (2) – (5) are 0.453, 0.389, 0.436, and 0.349, respectively, whereas the ones using the P-wave and S-wave data of $\varDelta \leq 200$ km recorded on land are 0.511 and 0.541, respectively [6]. This demonstrates that the estimates of M derived from the OBS data are comparable with or better than from the land observations in terms of accuracy, although the $\varDelta$ ranges used in the analysis are different. We conclude that the determination of M using the OBS data is useful for the P-wave alarm.

2.2 Proposal of P-wave alarm method for ocean bottom seismic data

As shown in Section 2.1, although the estimation of seismic source parameters using OBS data is less accurate in estimating back azimuth, the accuracies of estimating epicentral distance and magnitude in the range $\varDelta \leq 100$ km are equivalent with that using land seismograms. We consider that, it should not be a problem in the practical sense for EEW that the upper limit of the epicentral distance range is lower than land data, because the OBS networks is mainly designed to be a countermeasure against earthquakes that occur directly under or near the networks. In other words, before the OBS networks are installed, the EEW seismometers on land needed to target on events including the ones in the sea area (that is, the $\varDelta$ range should be longer); at present, however, the seismographs on land and seabed can respectively prepare against the earthquakes in each region, suggesting that the applicable range of $\varDelta$ for the OBS data can be shorter than the devices on land had to be. Therefore, we propose a concrete technique for the P-wave alarm without the back azimuth information using OBS data in the range of $\varDelta \leq 100$ km.

As mentioned in Chapter 1, the conventional Shinkansen EEW system employs only the S-wave alarm with fixed-section control for the OBS observations. Considering this, we propose that the P-wave alarm for the ocean-floor data adopt the fixed-section control method, suggesting that an alert can be issued more rapidly. The schematic illustration of this methodology is shown in Fig. 5. The three steps to judge if a warning is published are:

a) A seismometer in the OBS networks computes $\varDelta$ and M from P-wave data using the C-Δ method and the ground motion attenuation relations presented above, respectively;
b) The seismometer judges whether it is located inside or outside of the alarm area of the M-Δ diagram based on the estimated parameters $\varDelta$ and M [10];
c) Only if it is inside of the alarm area, the seismometer performs the fixed-section control as in the case of S-wave alarm.

The reason we can determine to issue the fixed-section control when the seismograph is located within the alarm area of the M-Δ diagram is that the diagram defines the area that has risks of damage to railway facilities (i.e., a strong ground motion will strike the M-Δ diagram area). That corresponds with the situation where the S-wave alarm is issued (that is, a shaking big enough to exceed the threshold is observed).

Importantly, the above three steps (a) – (c) do not require the estimates of back azimuth in the judgement but utilize only epicentral distance and magnitude. We conclude that the proposed method can improve the rapidness of EEW using OBS data and the safety of railways during earthquakes.

3. Conclusions

This study examined whether the P-wave alarm method, which estimates source parameters (epicentral distance $\varDelta$, back azimuth θ and magnitude M) and has been used in the conventional Shinkansen EEW system equipped with seismometers installed on land, is applicable to the OBS data to improve the rapidness of alerts for earthquakes. Our analysis demonstrated that $\varDelta$ and M estimated using the OBS records were equivalent in accuracy with that from the data observed on land, while θ could not be determined precisely enough. Considering this, we proposed a method for judging if a warning is published. The method monitors whether the seismograph that estimates the source parameters is located inside or outside of the alarm area defined by the M-Δ diagram, and then a stop signal for the fixed-section control is issued if it is inside. Because this can be judged only from $\varDelta$ and M, θ is not necessary to issue a warning. We conclude that it is useful for EEW based on the OBS data to increase the immediacy of alert information.

References

[1] Yamamoto, S., and Tomori, M., "Earthquake early warning system for railways and its performance," *Journal of Japan Society of Civil Engineers,* Vol. 1, pp. 322–328, 2013.
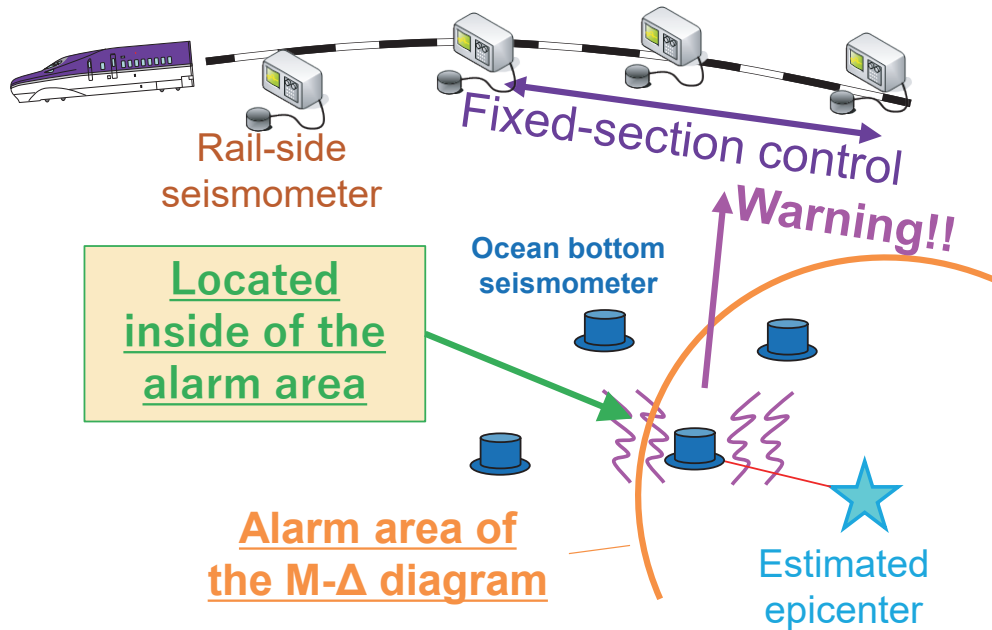[2] Ashiya, K., Sato, S., Iwata, N., Korenaga, M., and Nakamu-

Fig. 5 Schematic illustration of the P-wave alarm method applicable to OBS observation.

ra, H., "Application of earthquake early warning information to earthquake alarm systems in railways," *BUTSU-RI-TANSA*, Vol. 60, No. 5, pp. 387-397, 2007 (in Japanese).

[3] Korenaga, M., Yamamoto, S., Noda, S., and Aoi, S., "Earthquake Early Warning Using Ocean Bottom Seismic Data for Railways," *Quarterly Report of RTRI*, Vol. 60, No. 2, pp. 134-139, 2019.

[4] Aoi, S., Asano, Y., Kunugi T., Kimura, T., Uehira K., Takahashi, N., Ueda, H., Shiomi, K., Matsumoto, T., and Fujiwara H., "MOWLAS: NIED observation network for earthquake, tsunami and volcano," *Earth Planets Space*, Vol. 72, 126, https://doi.org/10.1186/s40623-020-01250-x, 2020.

[5] Miyakoshi, H., Yamamoto, S., Gion, A., Kamiyama, M., Taya, S., Watanabe, A., and Kunugi, T., "Data Processing for the Application of Ocean-bottomed Seismographs to the Earthquake Early Warning in the Railway Field," *RTRI Report*, Vol. 29, No. 1, pp. 35-40, 2015 (in Japanese).

[6] Iwata, N., Yamamoto, S., Korenaga, M., and Noda, S., "Improved Algorithms of Seismic Parameters Estimation and Noise Discrimination in Earthquake Early Warning," *Quarterly Report of RTRI*, Vol. 56, No. 4, pp. 291-298, 2015.

[7] Yamamoto, S., Noda, S., and Korenaga, M., "An Estimation Method of Epicentral Distance Based on Characteristics of P-wave Initial Envelope," *RTRI Report*, Vol. 26, No. 9, pp. 5-10, 2012 (in Japanese).

[8] Noda, S., Yamamoto, S., Sato, S., Iwata, N., Korenaga, M., and Ashiya, K., "Improvement of back-azimuth estimation in real-time by using a single station record," *Earth Planets Space*, Vol. 64, pp. 305-308, 2012.

[9] Noda, S., and Ellsworth, W. L., "Determination of earthquake magnitude for early warning from the time dependence of P-wave amplitudes," *Bulletin of the Seismological Society of America*, Vol. 107, No. 4, pp. 1860-1867, 2017.

[10] Nakamura, H., Iwata, N., Ashiya, K., "Statistical Relationships between Earthquake Disaster and Seismic Parameters Used for Train Operation Control after Earthquake," *RTRI Report*, Vol. 19, No. 10, pp. 11-16, 2005 (in Japanese).

[11] Odaka, T., Ashiya, K., Tsukada, S., Sato, S., Ohtake, K., and Nozaka, D., "A new method of quickly estimating epicentral distance and magnitude from a single station record," *Bulletin of the Seismological Society of America*, Vol. 93, No. 1, pp. 526-532, 2003.

Authors
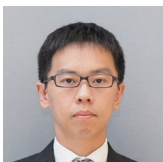
Shunta NODA, Dr. Sci.
Assistant Senior Researcher, Seismic Data Analysis Laboratory, Center for Railway Earthquake Engineering Research
Research Areas: Seismology, Earthquake Engineering

Naoyasu IWATA, Dr. Eng.
Senior Chief Researcher, Head of Seismic Data Analysis Laboratory, Center for Railway Earthquake Engineering Research
Research Areas: Earthquake Engineering

Method for Updating Operational Regulation Standards Considering Seismic Risk of Railway Facilities

Kazunori WADA   Kimitoshi SAKAI

Structural Dynamics and Response Control Laboratory, Center for Railway Earthquake Engineering Research

Akihiro TOYOOKA

Structural Dynamics and Response Control Laboratory, Center for Railway Earthquake Engineering Research (Former)

The regulation values of seismic intensity to suspend a train operation after earthquakes are determined empirically based on past disasters. Therefore, it is difficult to reflect the effects of seismic countermeasures in the operational regulation standards. To resume train operations as quickly as possible after earthquakes, this study proposes a method for updating the operational regulation standards based on risk analysis. In the proposed method, the seismic risk of each facility is evaluated and used to determine the regulation values for suspending train operations. Using this method, the effects of seismic countermeasures can be directly reflected in the operational regulation standards.

Key words: *operational regulation standards, seismic countermeasures, seismic risk*

1. Introduction

Train operation regulations for railways after earthquakes are based on index values observed by seismometers installed on the ground [1]. Here, maximum acceleration, instrumental seismic intensity, SI value, etc. are adopted as seismic motion indices and strength of seismic motion (hereinafter referred to as the operational regulation standards, ORS). The strengths of seismic motion to be regulated differ between railway operators. In some cases [1], ORS are set based on the lower limit of seismic motion strength at which damage occurs, after finding the relationship between seismic damage to facilities and estimated strength of seismic motion. ORS are generally set empirically in this way. Therefore, there are various uncertain factors, such as variations in seismic motion distribution which is determined by the interval between seismometers, and variations in damage distribution due to variations in structural strength. Accordingly, ORS are set according to engineering considerations taking into account these variations.

On the other hand, seismic countermeasures have been introduced based on the experience of large-scale earthquakes that have occurred more frequently in recent years. These seismic countermeasures include, for example, seismic diagnosis and retrofitting of railway structures and electric poles, or installation of seismometers along railway lines. There is no doubt that this has improved the seismic performance of railways and reduced the uncertainty of seismic motion distribution by increasing the density of seismic motion information. However, since ORS are set based on the lower limits causing past earthquake damage, it is difficult to explicitly reflect the effects of various seismic countermeasures when updating ORS. Therefore, this paper proposes a method to update ORS by evaluating the damage risk to each facility due to earthquakes after considering line section information such as the earthquake performance of each facility and the characteristics of seismic motion [2]. This paper introduces the outline of the method and the results of a case study.

2. Proposition of method for updating ORS

2.1 Basic idea

This study proposes a method to reflect the effects of various seismic countermeasures, such as seismic retrofitting of railway facilities and the installation of seismometers, in ORS. Here, the basic idea is to increase ORS based on seismic performance improvements by seismic countermeasures (Fig. 1(a)). On the other hand, as mentioned in the previous chapter, the current ORS are set empirically and based on engineering knowledge, including uncertain factors such as seismic motion information and evaluation of structural damage. Therefore, for example, a deterministic judgment such as "Since it was confirmed by numerical analysis that damage to the structure occurs at 100 gal or more, I set ORS to 100 gal," ignores uncertainties and safety factors that have been implicitly considered so far. As a result, the continuities with the conventional ORS are lost, and there is a concern that safety may be reduced.

In this study, "performance improvements by seismic countermeasures (improvements of yield strength, deformation performance, etc.)" are expressed by the effects of "reducing the possibilities of damage caused by earthquakes (risks of structural damage)." Therefore, the method is "increasing ORS based on the differences in the risks of damage reduced by the seismic countermeasures." Using the above concept, it is possible to explicitly reflect the improvements in the seismic performance of the line sections in the review of ORS, while retaining the engineering advantages of the conventional ORS as shown in Fig 1(b).

As a result, it is possible to "update ORS in a manner that reflects the effects of seismic countermeasures such as seismic retrofitting and the installation of seismometers" (Section 2.2). Furthermore, "updates to ORS due to the equalization of risk of damage in each section" can be realized regardless of whether seismic countermeasures are implemented (Section 2.3).

The above-mentioned method implements operational regulations based on the index values observed by seismometers installed on the ground. On the other hand, the characteristics of seismic motion (periodic characteristics, duration, etc.) are different for each earthquake. Even if multiple earthquakes occur at a certain point and the index values observed by seismometers are the same (e.g.,
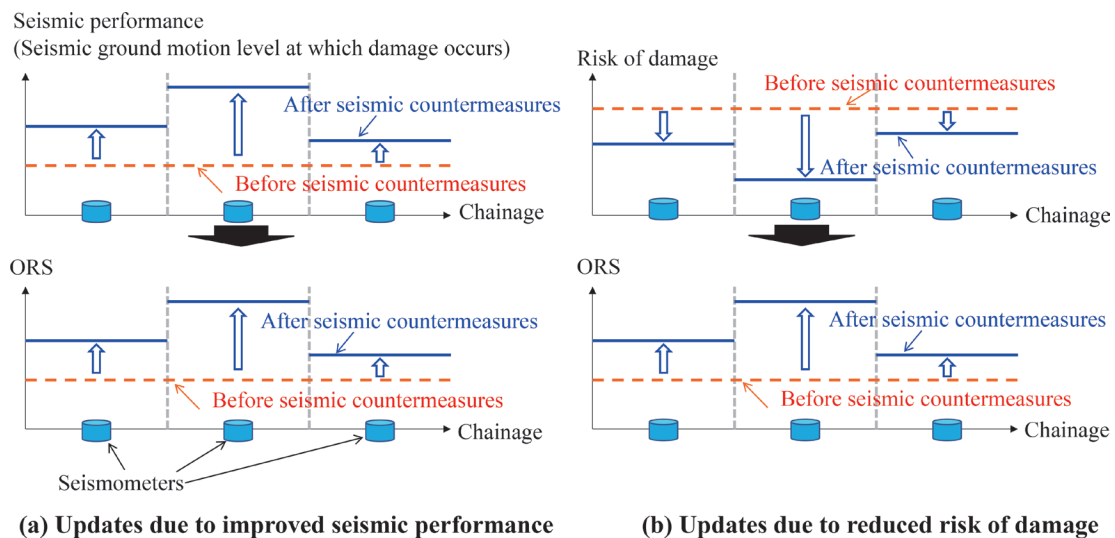
(a) Updates due to improved seismic performance

(b) Updates due to reduced risk of damage

Fig. 1 Outline of method for updating ORS

(a) Seismometer installation position and ORS
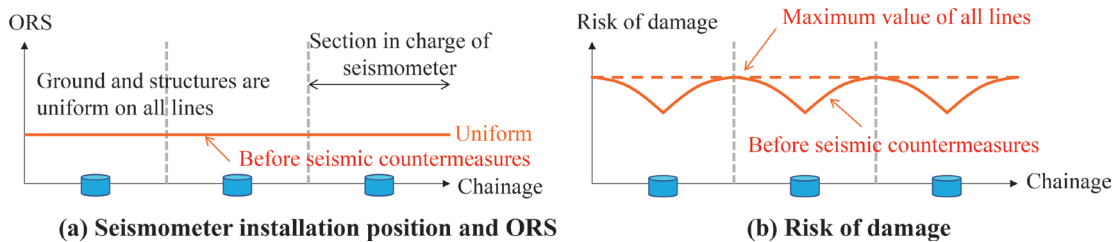
(b) Risk of damage

Fig. 2 ORS and risk of damage before various seismic countermeasures

seismic intensity 5+), it seems that there is a difference in terms of the impact on the structure. Therefore, more rational evaluation can be achieved by performing the operational regulation based on the damage of the structure compared with the operational regulation based on the index values recorded on the ground. Section 2.4 describes "operational regulations using the damage evaluation results of structures."

2.2 Updates of ORS considering the effect of seismic counter-measures

We explain the proposed method for updating ORS by quantitatively evaluating the effects of seismic countermeasures. At first, to mimic the initial situation in which the current ORS are set, we assume that the ground and structures are uniform, and the seismometers are installed at equal intervals over the entire line as shown in Fig. 2(a). ORS at this time shall be the same for all seismometers. The risk of structural damage is evaluated for this line section as shown in Fig. 2(b). The assumed seismic motion for the calculation of the risk of damage is at the same level as ORS in each seismometer. In addition, various uncertainties are considered for the risk of structural damage. When the same ground and structures are lined up, the spatial change in the total amount of uncertainty depends only on the distance from the seismometer, so the uncertainty increases as the distance from the seismometer increases. By considering this uncertainty, the risk of damage increases as the distance from the seismometer increases, as shown in Fig. 2(b). The risk of damage obtained here is "the probability that damage will occur at each railway facility when seismic motion equivalent to the regulation standard of train operations is observed by the seismom-

eter," and we set this as the basic condition.

Next, the risk of damage is calculated for the situation where seismic countermeasures are implemented at each facility. Seismic countermeasures, such as seismic retrofitting of facilities (Fig. 3(a)) and installation of seismometers (Fig. 3(b)) can be considered. Seismic retrofitting of facility can reduce the risk of damage since the seismic motion level at which damage can occur increases. In addition, installing more seismometers reduces the interval between seismometers become thus diminishing uncertainty between seismometers. This reduction in uncertainty may also reduce the risk of damage.

As a result, ORS are increased by the amount of the risk reduction described above. The scale of the increase can be set for sections assigned for seismometers within a range that does not exceed the risk of damage (Fig. 2(b)), which is set before seismic countermeasures are implemented. Therefore, the ORS for each state shown in Fig. 3 can be updated near the location where the seismic countermeasures were implemented, as shown by the blue line in Fig. 4.

2.3 Updates of ORS considering the characteristics of seismic motion, ground, and structures

By evaluating the risks of structural damage of the entire line section, it is possible to make comparisons between the risk of damage for respective sections assigned for seismometers. Railway lines are very long, and seismic motion characteristics, ground characteristics, and structural characteristics differ between sections. In the previous section, it is assumed that the various characteristics are the same for all lines, thus, the risk of damage is simple. However, in reality, change in risk of damage at respective points is complex.
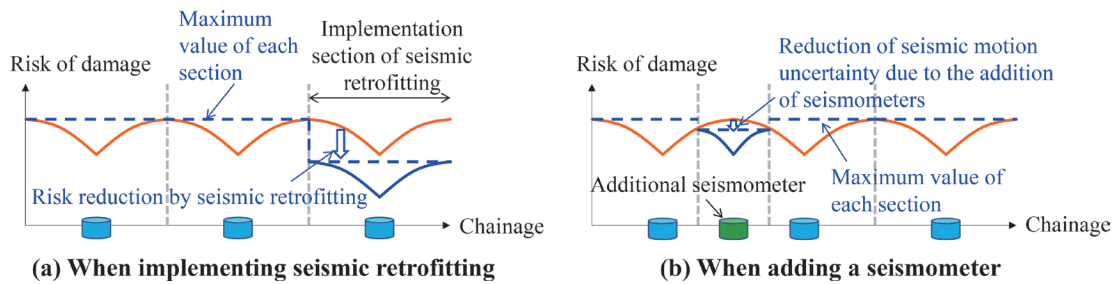
(a) When implementing seismic retrofitting

(b) When adding a seismometer

Fig. 3   Evaluation of the risk of damage after seismic countermeasures

(a) When implementing seismic retrofitting

(b) When adding a seismometer
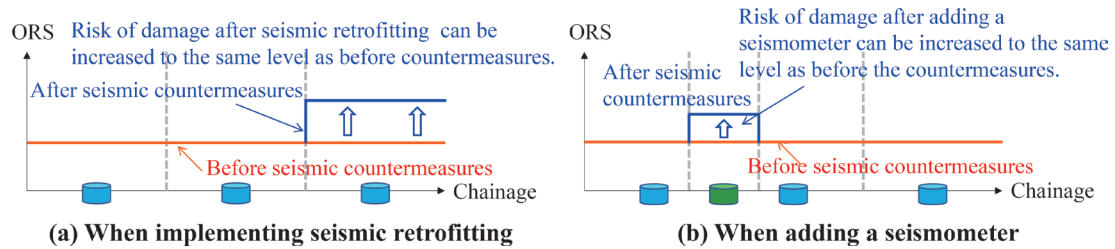
Fig. 4   Update of ORS based on seismic countermeasures
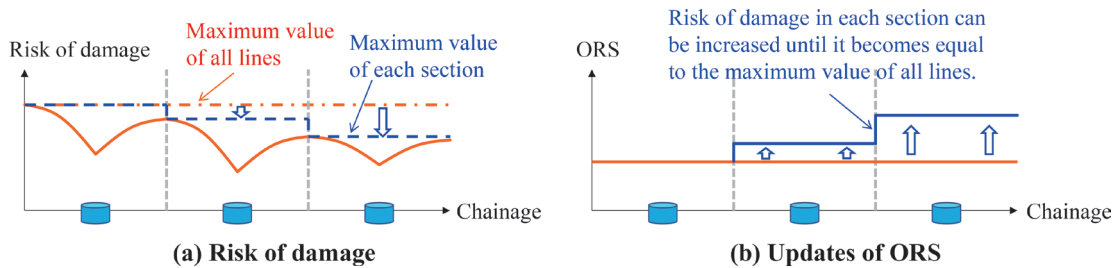

(a) Risk of damage

(b) Updates of ORS

Fig. 5   Updates of ORS considering the difference in seismic characteristics of each section

By considering the difference of the risk of damage at respective points, it is possible to update ORS regardless of the presence or absence of seismic countermeasures.

A concrete image is shown in Fig. 5. For this area, we assume that the risk of damage at the end point is small due to various factors (solid line in Fig. 5(a)). Here, as shown in Fig. 5(b), it is possible to raise ORS based on the difference between the risk of damage in the section assigned for the seismometer (dotted line in Fig. 5(a)) and the maximum value of all lines (dashed-dotted line in Fig. 5(a)). In addition, by combining this idea with the method described in the previous section, it is possible to further rationalize ORS.

2.4 Operational regulations based on damage evaluation results for each earthquake

The evaluations up to the previous section set ORS using a single index (SI value, etc.) obtained from seismometers installed on the ground. Although the method of expressing the damage of railway facilities with a single index is easy to evaluate, it is not possible to explicitly consider the periodic characteristics of seismic motion and the characteristics of structures (the differences in period and strength). As a result, many uncertainties remain for detailed behavior evaluation using the seismic motion index and structural conditions, so the risk of damage is also large. To reduce this uncertainty, we propose a method for evaluating the risk of structural damage by directly considering the seismic motion and the characteristics of the structure for each earthquake.

A concrete image is shown in Fig. 6. We assume that two earthquakes A and B have occurred, and in each of the earthquakes, records slightly exceeding ORS (dotted line in Fig. 6(a)) were observed in the three seismometers installed on the line section. If regulations based on the seismic records on the ground are enforced, the operational regulation will be enforced on all lines for both earthquakes.

ORS obtained by the seismometer include various variations when evaluating the behavior of the structure. It is the risk of structural damage before implementing various seismic countermeasures (Fig. 2(b)). Therefore, it is possible to reduce some uncertainties by performing damage assessment on individual seismic observation records and individual structural information using methods such as those used in seismic design. As a result, the risk of damage is likely to be reduced in many cases.

Therefore, Fig. 6(b) shows the image of the results when the risk of damage is evaluated individually for each earthquake immediately after the earthquake. For earthquake A, we assume that there is a region (dashed-dotted line in Fig. 6(b)) where the risk of damage exceeds the thresholds (dashed line in Fig. 6(b)). On the other hand, in the case of earthquake B, we assume that the risk is under the thresholds in all areas (solid line in Fig. 6(b)). In this case, it is possible to determine that the operation is restricted only in a limited range in earthquake A, and the operational regulation is not required for earthquake B. Therefore, in any case, when operation regulations are enforced based on the index value observed by the seismometers it is possible to rationalize their implementation.
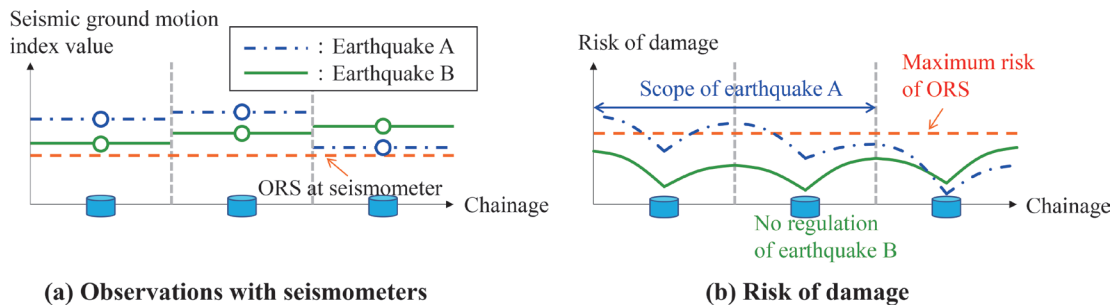
(a) Observations with seismometers

(b) Risk of damage

Fig. 6 Operational regulations based on the risk of damage for each earthquake

3. Updating ORS using the proposed method

3.1 Outline of target line section

A trial calculation was performed using the proposed method. The target line section was a virtual line with an extension of approximately 700 km as shown in Fig. 7. This line section comprised mainly bridges and viaducts, and the behaviors of these respective structures was evaluated by the equivalent single degree of freedom model used in seismic design. Here, the equivalent natural period T_{eq} and yield seismic intensity k_{hy} were set using the database [3] calculated in advance for structures with various specifications. We assumed that steel rod stoppers and steel angle stoppers were used for the bearings of these bridges and viaducts, and 12-40-N9B for electric poles is used for all lines. Furthermore, we assumed that seismometers along the railway line were installed at intervals of 20 km such as location of 0 km, 20 km, and 40 km in distance, and the operational regulation was to be implemented when the SI value exceeds 12 kine [1].

As the input seismic motions for evaluating the risk of damage, seismic observation records (7 typical waveforms observed in recent years) were used. Those waves were adjusted so that all seismometer SI values are at 12 kine. The spatial variations of seismic motion within seismometers were evaluated using the distance attenuation equation [4]. In addition, the risk of damage in the section assigned for each seismmometer was set to the maximum risk of damage for multiple seismic motions.

The behaviors of respective structures and the risk of damage were evaluated based on previous studies [5], [6], [7]. Specifically, for the bridges and viaducts, the ductility factor 1 was set as the limit value, and for the bearings and electric poles, the limit strength was set by converting it into the acceleration response. Although, it was basically necessary to evaluate the risk of damage in consideration of the uncertainties such as the yield strength and natural peri-
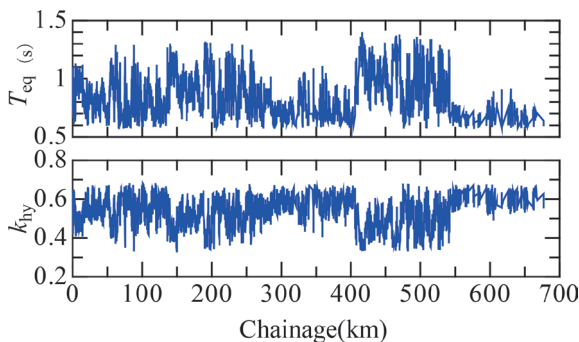
od of each facility [8], in this study, this effect was ignored and we assumed that the information on the structure was deterministically given. The results calculated under the above conditions are shown in Fig 8. This figure shows an index (risk ratio) in which the maximum value is normalized to 1. From this figure, the risks of damage to electric poles are at a maximum in many sections on this line. Therefore, under these conditions, the damage to the electric poles is a bottleneck from the viewpoint of operational regulations. In addition, the maximum value of the risk of damage fluctuates significantly on these sections. Some sections have risks about 0.6. This is due to the difference in ground characteristics and structural characteristics of respective sections.

3.2 Updates of ORS considering the effect of seismic countermeasures

In this section, we set several seismic countermeasure scenarios and make a trial calculation for updating ORS in consideration of the effect of seismic countermeasures. Specifically, we set three scenarios: a) seismic countermeasures for electric poles, b) seismic countermeasures for all facilities, and c) additional installation of seismometers.

The increase in seismic performance of respective facilities due to seismic countermeasures should be evaluated for respective structures, but in this study, it is set uniformly as follows. First, we replace the electric poles with steel pipe columns. For bridges and viaducts, we assume that shear reinforcements increase the seismic intensity to damage level 2 by 30%. For bearings, we assume that the critical seismic intensity increases by 20%. For the installation of seismometers, they are allocated at the midpoint of the conventional 20 km interval so that they are installed at 10 km intervals.

The change in the risk of damage caused by implementing these measures is calculated for each scenario in the following sections. At this time, the change in the risk of damage is normalized by the risk of damage before the installation of seismic countermeasures, and called the "risk change rate."
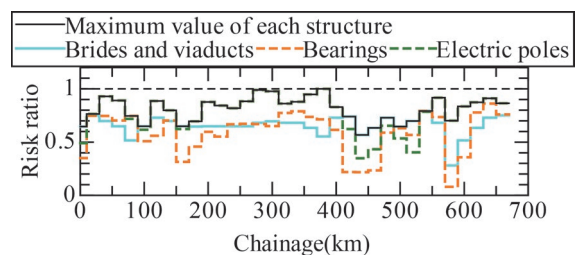

Fig. 7 Information on target line section (vibration characteristics of structures)

Fig. 8 Current evaluation results of the risk of damage

3.2.1 Effect of implementation of seismic countermeasures on electric poles

Figure 9 shows the risk change rate when seismic countermeasures are implemented for the electric poles, which previously had a relatively high risk of damage (Fig. 8). These results show that the risk of damage to the electric poles has been reduced to almost zero, and that the risk of damage has been reduced overall by implementing seismic countermeasures. However, the risk change rate remains at 1 even after the seismic countermeasures in the vicinity of 400 km to 550 km, where the risks of damage other than the electric poles are relatively high before the countermeasures.

Next, ORS are updated based on the risk change rate. Figure 10 shows that ORS can be significantly raised in places where the risk of damage is greatly reduced in Fig. 9, such as around 580 km. On the other hand, in a place where the risk of damage other than the electric poles is maximum (for example, around 450 km) before the installation, the risk of the place is not reduced even if measures are taken for the electric poles. As a result, ORS do not change.

3.2.2 Effect of implementation of seismic countermeasures for all facilities

The risk of damage is evaluated when seismic countermeasures are implemented for all bridges and viaducts, bearings, and electric poles. Figure 11 shows that the risk of damage is significantly reduced over the entire line. Figure 12 shows the results of updating ORS based on the proposed method in this state. This figure shows that it is possible to realize a significant increase in ORS for all lines as the risk of damage is significantly reduced.

3.2.3 Effect of additional installation of seismometers

Additional installation of seismometers leads the reduction of the uncertainty of seismic motion distribution between seismometers, and as a result, the risk of damage should be reduced. Therefore, we evaluate the changes in the risk of damage caused by the installation of seismometers and the updated ORS. Here, the risk

change rate is evaluated based on the state of 3.2.1. (only countermeasures for electric poles).

Figure 13 shows the results of risk change rate when changing the interval from 20 km to 10 km and Fig. 14 shows the results of updating ORS. In this case, installation of seismometers, significantly reduces risk and increases the ORS. In addition, there are differences in the effects of seismic countermeasures depending on the region. This is because the conditions of the structures fluctuate in a complicated manner as shown in Fig. 7. For example, if there is a weak structure near the seismometer, the risk reduction effect associated with the installation of the seismometer will be small, and ORS will not increase by much. On the other hand, if the weak structure is far from the seismometer, the uncertainty of the seismic motion at this location is reduced, and the risk of damage is greatly
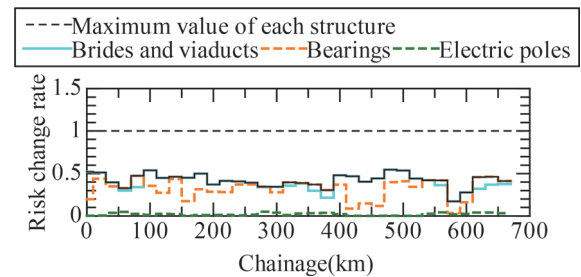

Fig. 11 Changes in risk of damage following implementation of seismic countermeasures to all facilities
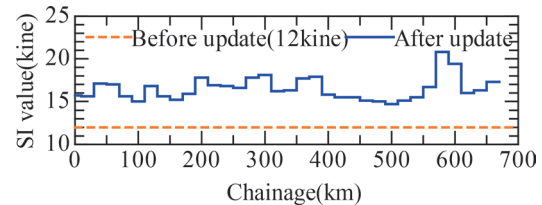

Fig. 12 Updated results of ORS following implementation of seismic countermeasures to all facilities

Fig. 13 Changes in the risk of damage following installation of seismometers

Fig. 14 Update results of ORS following installation of additional seismometers
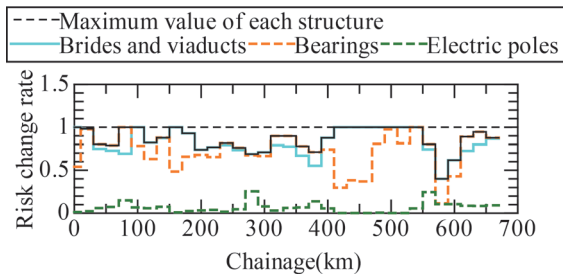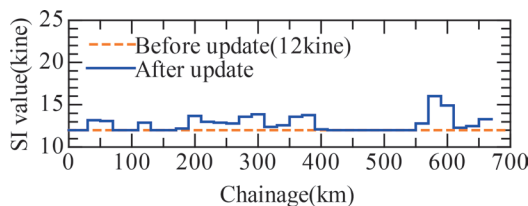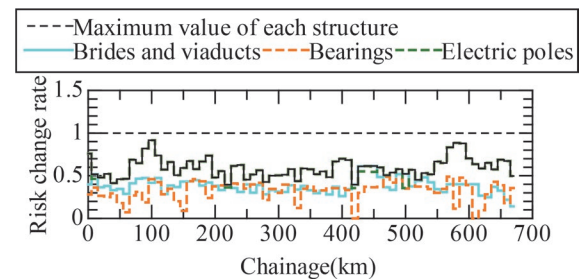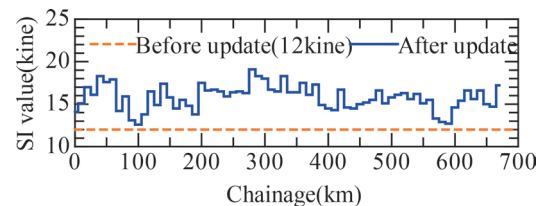

Fig. 9 Changes in the risk of damage due to seismic countermeasures for electrified poles

Fig. 10 Updated results of ORS following implementation of seismic countermeasures on electrified poles

reduced.

In addition, although omitted here due to space constraints, it has been separately confirmed that operational regulations can further be rationalized [2] by considering the seismic motion, ground, and structure characteristics of each section shown in Section 2.3 and the damage evaluation for each earthquake shown in Section 2.4.

In this way, by using the proposed method, the effects of various seismic countermeasures can be quantitatively evaluated in terms of reduced risk of damage. With this method, not only is it possible to evaluate seismic measures for civil engineering structures, but it is also possible using the same index to evaluate measures implemented on other facilities and assess the effect of installing seismometers. Furthermore, it was confirmed that this reduction in the risk of damage can be directly reflected in updated ORS.

4. Conclusions

In this study, we proposed a method for updating ORS to allow early resumption of operations after earthquakes. Specifically, we proposed the method for evaluating the risk of damage caused by earthquakes, considering line section information such as the seismic performance of each facility and the input seismic motion. Then, based on this, we proposed a method for implementing operational regulations and confirmed the effectiveness of the method.

By using the proposed method, it is possible to directly relate the effects of improving the seismic performance of respective facilities and increasing the density of seismic motion information from additional seismometers, to the operational regulations. This method makes it possible to rationalize inspection points. Furthermore, the proposed method makes it possible to quantitatively evaluate the number of implementations of operational regulations, their range, and their economic impact. Therefore, it is possible to evaluate the effects of seismic diagnosis, seismic retrofitting, and the installation of seismometers to improve operational regulation efficiency.

In this estimation, the assumed damage points are limited, but the actual damage points of the railway during earthquakes are wide-ranging. Therefore, when applying the proposed method to actual line sections, it is necessary to make evaluations that can cover various types of damages. To this end, it is important to utilize the various achievements so far and continue to work on the sophistication of earthquake damage prediction methods at respective facilities.

References

[1] Suzuki, H. and Shimamura, M., "Research on Train Operational Regulations for Railways after Earthquakes," *JR East Technical Review*, No. 3, pp. 53-60, 2003 (in Japanese).

[2] Sakai, K., Wada, K., and TOYOOKA, A., "Method for Setting Operation Control Values considering Seismic Risk of Railway Facilities," *Journal of railway engineering*, JSCE, No. 25, pp. 17-24, 2021 (in Japanese).

[3] Onodera, M., Wada, K., Sakai, K. and Murono, Y., "Seismic Damage Estimation of Railway Bridges and Viaducts by Inventory Method," *RTRI Report*, Vol. 33, No. 12, pp. 29-34, 2019 (in Japanese).

[4] Si, H. and Midorikawa, S., "New Attenuation Relationships for Peak Ground Acceleration and Velocity considering Effects of Fault Type and Site Condition," *J. Struct. Constr. Eng.*, AIJ, No. 523, pp. 63-70, 1999 (in Japanese).

[5] Railway Technical Research Institute, *Design Standards for Railway Structures and Commentary (Seismic Design)*, Maruzen co., Ltd, Tokyo, 2012 (in Japanese).

[6] Sakai, K. and Matsumoto, H., "Nomograph for Rapid Estimation of Damage Probability for Railway Structures," *Journal of JSCE*, series A1 (Structural Mechanics and Earthquake Engineering), Vol. 77, No. 4, I_373-I_383, 2021 (in Japanese).

[7] Tanaka, S., Sakai, K., Tanaka, K. and Harada, S., "The Simplified Method for the Evaluation of Seismic Response of Electric Pole Built on Railway Structure," *Journal of railway engineering*, JSCE, No. 22, pp. 201-205, 2018 (in Japanese).

[8] Wada, K. and Sakai, K., "A Study for Improving the Accuracy of Estimating the Probability Distribution of Seismic Nonlinear Response considering the Uncertainty of Structural Characteristics," *Journal of JSCE*, series A1 (Structural Mechanics and Earthquake Engineering), Vol. 77, No. 4, I_47-I_60, 2021 (in Japanese).

Authors

Kazunori WADA
Assistant Senior Researcher, Structural Dynamics and Response Control Laboratory, Center for Railway Earthquake Engineering Research
Research Areas: Earthquake Engineering

Kimitoshi SAKAI, Dr. Eng.
Senior Chief Researcher, Head of Structural Dynamics and Response Control Laboratory, Center for Railway Earthquake Engineering Research
Research Areas: Earthquake Engineering

Akihiro TOYOOKA, Dr. Eng.
Senior Chief Researcher, Head of Structural Dynamics and Response Control Laboratory, Center for Railway Earthquake Engineering Research (Former)
Research Areas: Earthquake Engineering

Proposal of Snowmelt Disaster Warning Criteria Using Effective Rainfall Index Which Reflects Snowmelt

Tsuyoshi TAKAYANAGI
Geo-hazard & Risk Mitigation Laboratory, Disaster Prevention Technology Division

Ryota SATO
Meteorological Disaster Prevention Laboratory, Disaster Prevention Technology Division

Osamu NUNOKAWA
Disaster Prevention Technology Division

In snow-covered areas, slope failures induced by snowmelt water may occur. In this study, we attempted to develop a warning method for snowmelt disasters using the effective rainfall index, which reflects the analyzed snowmelt amount (hereinafter referred to as the effective snowmelt index) and we verified the appropriate half-life of the effective snowmelt index by comparing it with the observation results of groundwater response. As a result, it was confirmed that a strong correlation between them under the conditions that the half-life of the index was set from 24 hour to 96 hour. In addition, through case studies, we found that the warning method using the effective snowmelt index and snow depth as evaluation indices could effectively provide warning of snowmelt disasters.

Key words: snow melting, slope, maintenance, disaster prevention, effective rainfall index, operation regulation

1. Introduction

It is widely known that slope failures triggered by rainwater infiltration (hereinafter referred to as "rainfall disasters") occur during heavy rainfall. Whilst less frequent than rainfall disasters, slope failures triggered by the infiltration of snowmelt water (Fig. 1) do occur and have affected train operations, in regions such as Hokkaido, the Japan Sea coast of Honshu and other regions [2] (Fig. 2). Here, "snowmelt disaster" is defined as a slope failure caused by snowmelt and rainfall during snowy seasons, without the external force of earthquakes. Rainwater and snowmelt permeate into the ground, increasing water content in the ground. However, snowmelt cannot be measured with rain gauges. For this reason, it is difficult to determine warning criteria for snowmelt disasters using operational regulations (warning criteria) based on rainfall only.

Consequently, railway companies operating in snowy regions take measures to ensure train safety, for example, by increasing patrols during snow-melting seasons (generally from March to May), in addition to applying normal operating restrictions when there is rain. However, decisions about when to issue snowmelt disaster warnings and which locations to patrol are often based on empirical judgments. In this study, we focus on warning criteria for identifying times when there is a high risk of a snowmelt disaster.

2. Warning criteria for snowmelt disaster

2.1 Basic policy

The mechanism underlying slope failure in snowmelt disasters is basically similar to that of rainfall disasters. The main causes of the failure are assumed to be increased self-weight and decreased shear resistance of soil due to increasing of water content in the ground caused by water supply from snowmelt (including cases where rainfall is combined with snowmelt). Therefore, we believe
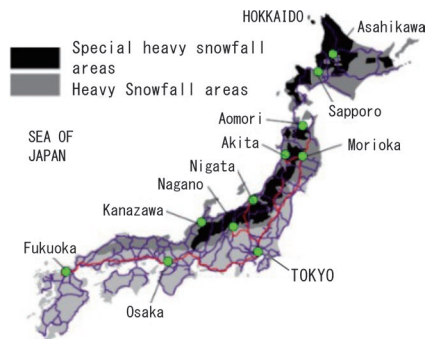

Fig. 1 Major railway network along with snowfall areas and locations where snowfall is particularly heavy [1]

Fig. 2 Example of embankment collapse triggered by infiltration of snowmelt

that a real-time snowmelt disaster warning criteria can be constructed by combining an evaluation index that reflects snowmelt water and an existing system of operating restrictions during rainfall implemented by railway operators.

In order to obtain real-time snowmelt information, this study uses a method of calculating analytical values of snowmelt amounts using data distributed by AMeDAS [3] of the Japan Meteorological

Agency. Details of the analysis methods are described in reference [4].

In this study, the value obtained by dividing the volume of snowmelt water accumulated over a certain period by the area is called "snowmelt amount" (mm), in particular, the accumulated value per hour is called "hourly snowmelt amount" (mm) and the value obtained by converting some instantaneous snowmelt amount to the amount per hour is called "snowmelt intensity" (mm/h).

2.2 Effective rainfall index reflecting snow melt

As an indicator for snowmelt hazard warning criteria, it is reasonable to adopt an evaluation index that is linked to the soil moisture response on slopes subjected to long-term infiltration of snowmelt. In this study, we use an "effective rainfall index" [5], which is an indicator that simulates the response of soil moisture to rainwater infiltration and has been adopted by some railway companies in Japan. Equation (1) shows the formula for calculating the effective rainfall index.

$$R_{c\,(t)} = R_{c\,(t-1)} \left(\frac{1}{2} \right)^{\frac{1}{T}} + w_s \tag{1}$$

T : half-life (h)
w_s : Hourly infiltration water amount
 (= hourly snowmelt amount s + hourly rainfall P_r) (mm)
$R_{c(t)}$: Effective rainfall index (mm)
$R_{c(t-1)}$: Effective rainfall index at 1 hour before

In this study, the effective rainfall index evaluated during the snow accumulation period (defined as the period when a snow depth at a representative meteorological observation point is 1 cm or more) which can be reflected an hourly snowmelt amount s, is called "effective snowmelt index R_{cs}" and is adopted as the main evaluation index for snowmelt disaster warning criteria.

3. Research issues and objectives

The main goal of this study is to develop snowmelt hazard warning criteria, and for this purpose, the following are examined based on the issues discussed in the previous section.

3.1 Issues related to the half-life T of the effective snowmelt index R_{cs}

The first issue is about half-life T, a parameter used to calculate the effective snowmelt index R_{cs}. This parameter controls the attenuation of soil moisture, so it should be set as an appropriate parameter based on data of actual response of soil moisture on slopes along railway lines from the perspective of operating as a disaster warning criterion. In a previous study, Mizoguchi and Katsura [6] compared the effective rainfall index R_c which is added to the amount of snowmelt, with the ground water behavior at large landslide sites. Note that ground water is highly related to slope stability. As the result of the comparison, it is reported that half-life T shows high correlation with ground water behavior. However, there are no previous studies that have examined how to establish an appropriate effective snowmelt index R_{cs} of half-life T to evaluate the stability of embankments, cuts, and natural slopes along railway lines that are vulnerable to snowmelt disasters.

3.2 Issues related to warning criteria using effective snowmelt index

The second issue is that no appropriate method for determining when to issue a snowmelt disaster warning using the effective snowmelt index has been established. In particular, it is necessary to establish a method for setting an effective snowmelt index threshold to determine when a snowmelt disaster warning should be issued. Although we have studied the development of disaster warning criteria using the effective snowmelt index R_{cs} as an evaluation index, the method using only the effective snowmelt index R_{cs} has problems in detecting snowmelt disasters accurately.

The difference between snowmelt and rainfall disasters is the difference in meteorological phenomena that cause moisture supply and the presence or absence of snow accumulation. Although quantitative evaluation of the effect of snow accumulation on slope stability is still at a technical development stage, snow accumulation is assumed to be a risk for snowmelt disasters, as there are many cases where snow accumulation has been reported to be the cause of snowmelt disasters as it obstructs water flow in waterways.

3.3 Research objectives

The main goal of this study is to develop snowmelt disaster warning criteria, and for this purpose, the following are examined based on the issues discussed in the previous section.

The first objective is to understand the actual soil moisture behavior of several embankments and cut slopes along railway lines in snowy areas, to determine the half-life T of the effective snowmelt index R_{cs} which has a strong correlation with soil moisture behavior. The results are used to estimate an appropriate half-life T level to be set for the effective snowmelt index R_{cs}. Secondly, we examine the snowmelt disaster warning criteria that employs the effective snowmelt index R_{cs} and snow depth as evaluation indices, and the method of setting the threshold of the criteria. In addition, the performance of the warning criteria is verified by evaluating their accuracy in recognizing past disasters.

4. Field observation [7]

In order to understand the range of half-life T of effective snowmelt index R_{cs}, which is strongly correlated with soil moisture behavior, we conducted long-term field observations of soil moisture behavior on slopes along a railway line in a snow-covered area. Specifically, three locations with different topographical conditions (Case 1: embankment on level ground, Case 2: cut slope of a terrace cliff, and Case 3: graded embankment on a terrace cliff) were selected from slopes along a railway line in a snow-covered area, and soil moisture behavior (groundwater level and volume water content) was observed for about two years. Slopes in Cases 2 and 3 were locations where snowmelt disasters had occurred in the past. The effective snowmelt index R_{cs} was calculated using meteorological data from nearby *AMeDAS* stations, and compared with the observed soil moisture behavior. This chapter reports the results of Case 3 as a representative example.

4.1 Summary of observations

Case 3 for observation is a graded embankment on a river terrace in Nagano Prefecture, Japan. Slope failure occurred in the past during the snowmelt season (early April) on the embankment. The

collapse area is shown as "old collapse area" on the plan in Fig. 3. The collapse occurred at the embankment of a road and railway alongside the river. The slope gradient of the embankment on the river side was about 25°, the maximum depth of the collapse was about 4 m, the width of the collapse was about 13 m, and the length of the collapsed slope was about 34 m. And Fig. 3 shows installation of measurement equipment (groundwater level meters).

4.2 Observation results

In this case, instruments operated during an observation period between November 11, 2017, and May 16, 2018. Figure 4 shows meteorological data from the nearby *AMeDAS* (*AMeDAS* Nozawa Onsen, elevation EL.576 m, distance from the observation site 7.5 km, elevation difference from the local slope −226 m), hourly water infiltration amount w_s calculated using the meteorological data, data of groundwater level W_l and effective snowmelt R_{cs24} (half-life T is tentatively set to 24 hours).

Figure 5 shows that the groundwater level rises significantly in the latter half of the snow season. These results indicate that the groundwater level W_l rises significantly in the latter half of the snow season, and that the slope stability decreases during the snowmelt season. Furthermore, focusing on the relationship between the 24-hour effective snowmelt index R_{cs24} and the groundwater level W_l, the timing of the increase in both is generally consistent throughout the snow covered and non-snow-covered seasons. These results indicate that a correlation can be expected between the 24-hour effective rainfall and the behavior of the groundwater. These trends were also confirmed in other observation cases.
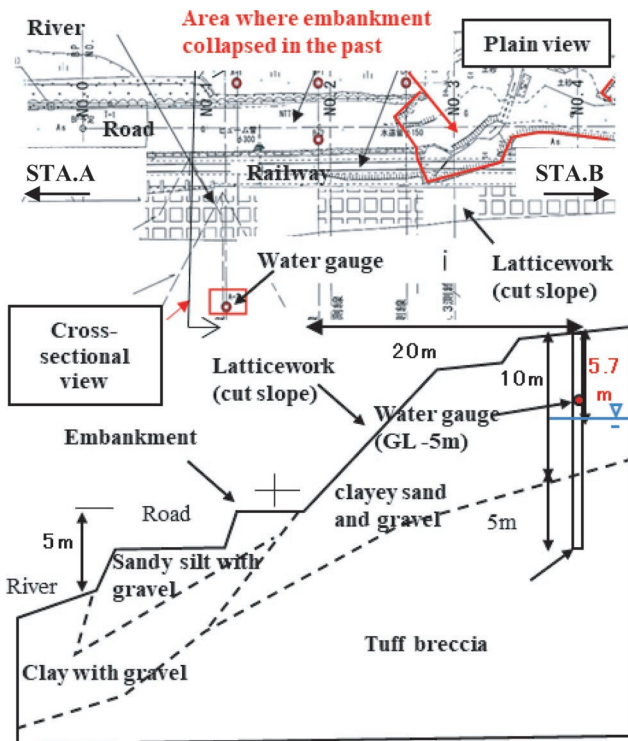
5. Verification of appropriate half-life [8]

5.1 Overview of parameter studies

A parameter study was conducted to obtain an appropriate half-life T to be set for the effective snowmelt R_{cs} from the viewpoint of soil moisture behavior.

The effective snowmelt R_{cs} with different half-life T (half-life T = 1.5 h, 6 h, 12 h, 24 h, 48 h, 72 h, 96 h, 120 h, 144 h, 192 h, 240 h, 336 h, 432 h, 720 h) were calculated for three observation cases of this study by using nearby *AMeDAS* weather data. The correlation coefficients r (Fig. 5) were calculated with the groundwater level W_l and volumetric water content θ to determine the half-life T at which a high correlation coefficient r is obtained.

In this paper, the "optimal half-life T_{opt}" is defined as the half-life T of the effective snowmelt R_{cs} for which the highest correlation coefficient r is obtained in the relationship between the effective snowmelt R_{cs} and variables related to soil moisture status (i.e., groundwater level WL and volumetric water content θ).

5.2 Parameter study results

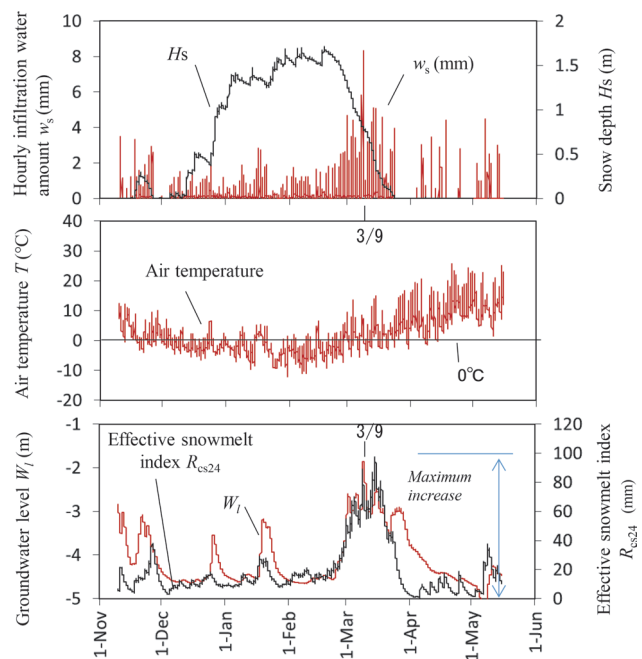As a result of the parameter study, the half-life T of the effective
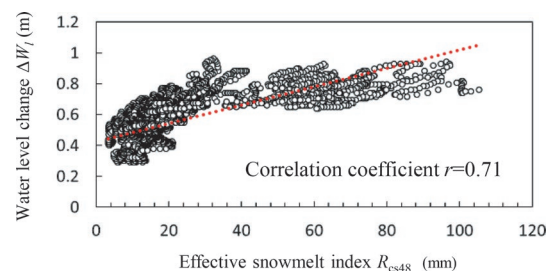

Fig. 4   Field observation results of Case 3

Fig. 3   Installation of measurement equipment in Case 3

Fig. 5   Correlation between effective snowmelt index R_{cs48} and groundwater level change ΔW_l (Observation Case 1, snow season only, 2 years)

snowmelt R_{cs} in each observation case and the correlation coefficient r between the effective snowmelt R_{cs} and soil moisture behavior (groundwater level WL, volumetric water content θ) are shown in Figs. 6 and 7. The representative point for the volumetric water content θ is a sensor located at GL-0.25 m from the ground surface. The groundwater level is assumed to be associated with the risk of relatively deep slope failure, while the volumetric water content measured at shallow depths is assumed to be associated with the risk of relatively shallow surface failure.

The results of the parameter study show that the half-life T of the effective snowmelt index R_{cs}, which is strongly correlated with the groundwater level W_l (correlation coefficient $r \geq 0.7$ in this case), is between 24 h and 96 h (optimal half-life T_{opt} 48 h) in Case 1. Furthermore, the half-life T of the effective snowmelt index R_{cs}, which obtained a strong correlation with the groundwater level W_l ranged from 12 h to 720 h (optimal half-life T_{opt} 432 h) for Case 2 and from 12 h to 432 h (optimal half-life T_{opt} 48 h) for Case 3. The optimal half-life T of the effective snowmelt index R_{cs} with respect to the volumetric water content θ of the surface layer is 24 h for case 1 and 120 h for case 2.

Based on the results of the above analysis, it is judged generally appropriate to set the representative value $T_{rep,}$ of the half-life T of the effective snowmelt index in the snowmelt disaster warning criteria using the effective snowmelt index $R_{cs,}$ to between 24 h to 96 h in terms of soil moisture behavior. Although the optimum half-life of each slope differs as soil moisture behavior, it is not realistic to set an individual half-life for each slope because of the need for simplicity in terms of the actual application of the disaster warning criteria, and it is necessary to adopt a representative half-life T that is highly linked to the average soil moisture behavior.

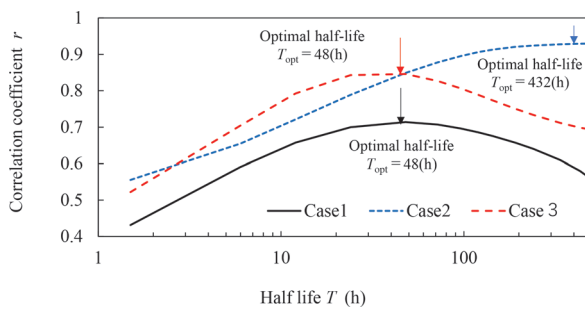If an excessively long half-life T is used, it will take a long time for the effective snowmelt to decrease below the threshold after it exceeds the threshold, which may impose an excessive burden on the field due to the long period of time required to issue the warning.

Considering the above points, in this study, we adopt 24 hours as the representative value of the half-life T of the effective snow-melting amount R_{cs} in the operation of the disaster warning criteria T_{rep}.

6. Snowmelt disaster warning criteria using effective snowmelt and snow depth as indicators

6.1 Summary of warning criteria

The disaster warning criteria we studied in the past adopted the effective snowmelt index R_{cs24} as the only index value used for evaluation and adopted a method of setting a certain threshold value according to the level of effective snowmelt index R_{cs24} experienced in the past.

However, during the first half of the snowmelt season (February to March in JAPAN), when relatively large amounts of snow remained, there were cases where at the time of the disasters, the effective snowmelt index was lower than the effective snowmelt index experienced in the past.

Snow accumulation can have a negative impact on slope stability by acting as a snow load on slopes and obstructing drainage channels. In order to properly assess the risk of snowmelt disasters in such snowy environments, it is better to change the threshold value of the effective snowmelt index according to the snow depth. In this study, we examined a method for setting the threshold of disaster recognition by adding the snow depth H_s to the effective snowmelt index R_{cs24}.

Figure 8 shows an overview of the snowmelt disaster warning criteria examined in this study. Figure 8(a) shows the history of the combination of effective snowmelt R_{cs24} and snow depth H_s (hereinafter referred to as the "snake line") for the past 20 years at locations which have a history of snowmelt disasters. As shown above, when the snow depth H_s is large, the effective snowmelt R_{cs24} experienced in the past tends to be small.

As a basic concept of snowmelt disaster warning threshold, the side of a blank area with no history of past snake lines is judged to be the dangerous side, while the side of an area with a lot of history of snake lines is judged to be the safe side.

The maximum value of the effective snowmelt index R_{cs24} for each year is plotted for each snow depth of 0.1 m for the past 20 years as Fig. 8(b). Using this data of the maximum value of effective snowmelt index R_{cs24} experienced for each snow depth H_s, an extreme value statistical analysis based on the Gumbel distribution was performed to organize the probability years (2-year, 4-year, and 8-year probabilities) of effective snowmelt index R_{cs24} for each snow depth H_s, as shown in Fig. 8(c).

Approximate curves are obtained from the plots of the same probability year groups (2-year, 4-year, and 8-year probabilities). In this study, the approximate curve for the 2-year probability is set as threshold 1, the 4-year probability as threshold 2, and the 8-year probability as threshold 3. Then, when the snake line at the time of evaluation exceeds the threshold of a higher probability year, the risk of a snowmelt disaster is considered to be greater.

Figure 8(d) shows an example of the comparison between the snake line and the threshold value for the evaluation year. In the actual operation of this method, it is necessary to take measures to avoid the snake line exceeding the threshold value due to the deep snow, even though it is a period when snow melting does not occur

Fig. 6 Summary of correlation coefficient and half-life relationship (Relationship between groundwater level and effective snowmelt index)
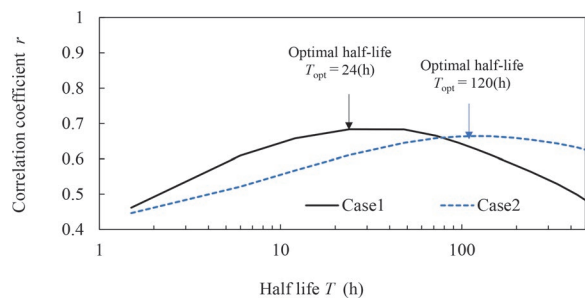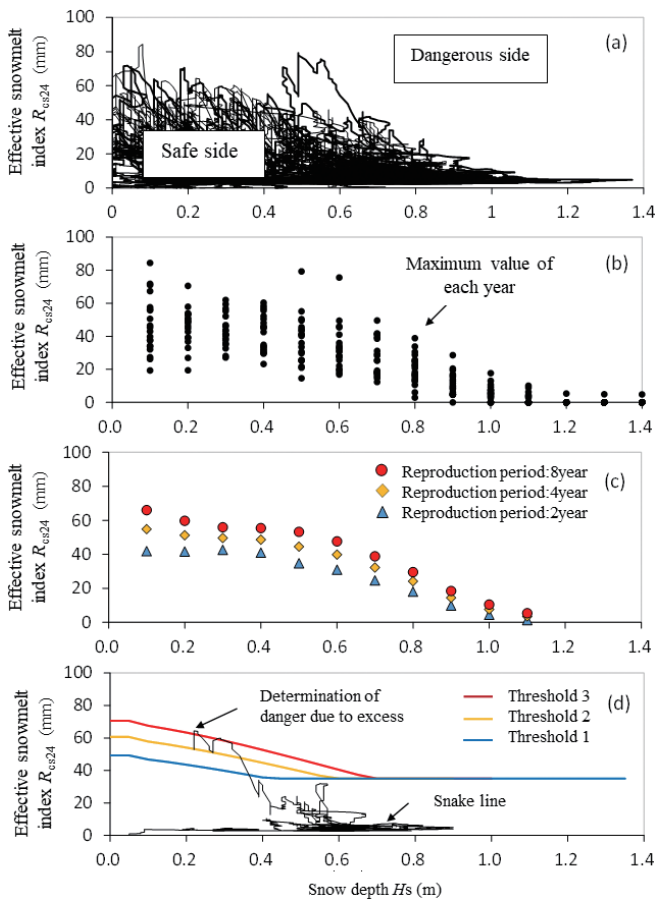

Fig. 7 Summary of correlation coefficient and half-life relationship (Relationship between volumetric moisture content and effective snowmelt index)

Fig. 8 Outline of snowmelt disaster warning criteria using effective snowmelt index and snow depth as indicators
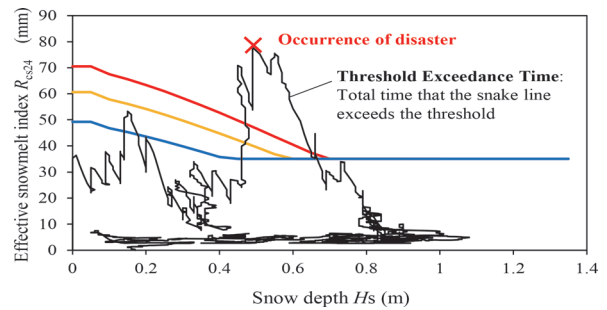

Fig. 9 Concepts related to threshold exceedance time and detectable disaster rate
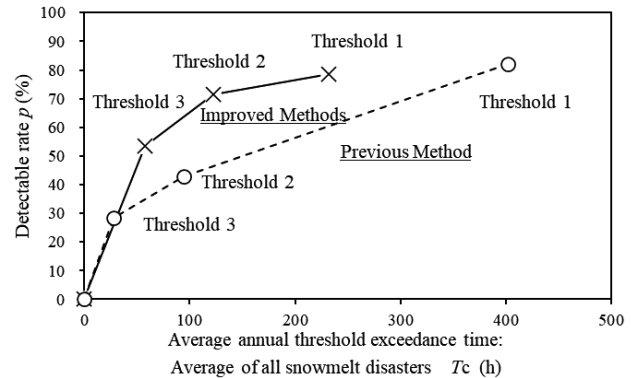
Fig. 10 Relationship between detectable disaster rate and threshold exceedance time

(period when snow cover is thick).

Therefore, a certain lower limit was set for each threshold value (35 mm was set as the lower limit in this study). In addition, since there is a possibility that the snow depth in *AMeDAS* data may rarely deviate from the snow depth at an evaluation site.

Therefore, when evaluating the effective snowmelt index R_{cs24} using *AMeDAS* data, as a safety measure, even if the snow depth in *AMeDAS* becomes zero, it is assumed that there is residual snow at an evaluation site, and the snowmelt amount is added for a certain period (in this study, the period was 14 days from the snow disappearance date in *AMeDAS*).

6.2 Verification through comparison with past disasters

In this section, we report the results of our analysis of 28 cases of past snowmelt disasters collected by JR Hokkaido and JR East, and specifically the results of our comparison of the threshold values with the effective snowmelt index in the year of the disaster to determine the probability of recognizing disasters and the time over which the snake line exceeds threshold values (Fig. 9).

If the effective snowmelt R_{cs24} exceeds the threshold at the same time a past snowmelt disaster is confirmed, then, the threshold is deemed to be appropriate to detect past snowmelt disasters.

Here, the "detectable rate p" is calculated as the ratio of the number of detectable cases to the total number of snowmelt disasters collected in this study (28 cases).

In addition, we calculated an average threshold exceedance time T_c. Time here is the average shown on a scatter plot, consisting of effective snowmelt R_{cs24} and snow depth H_s, which exceed a threshold line on a graph covering the past 20 years.

Figure 10 shows a scatter plot of the relationship between the average threshold exceedance time T_c and the detectable rate p for each threshold value (thresholds 1,2 and 3).

For comparison, the same graph shows the relationship between the average threshold exceedance time T_c and the detectable rate p when using the previous method (a method that evaluates risk only by the effective snowmelt amount index R_{cs24}, and the threshold is set by an extreme statistical analysis of the effective snowmelt amount R_{cs24}).

Figure 10 shows that the relationship between the threshold exceedance time T_c and the detectable disaster rate p changes according to the threshold value set. In particular, it can be seen that the detectable rate p is higher when the threshold value is low, but the threshold exceedance time T_c (regulation time) is longer. In other words, by referring to Fig. 10, an appropriate warning threshold can be set in practice according to the relationship between the detectable rate p and the threshold exceedance time T_c (regulatory time). Figure 10 also shows that this improved snowmelt disaster warning criterion which adapts snow depth into the method, improves the detectable rate p by about 20% for the same threshold exceedance time T_c when compared with the previous method.

7. Conclusion

This study aimed to develop snowmelt disaster warning criteria to evaluate the risk of snowmelt disasters caused by snowmelt water

in early spring. It was found that it is appropriate to set the half-life T of the effective snowmelt index R_{cs} to be approximately 24 hours, based on the actual behavior of soil moisture on several embankments and cut slopes along a railway line in a snowy area. The improved snowmelt disaster warning criteria, which employs the effective snowmelt index R_{cs} and snow depth H_s as evaluation indices, was found to improve the detectable disaster rate p for the threshold exceedance time T_c compared to the previous method.

References

[1] Ministry of Land, Infrastructure, Transport and Tourism: Designation of Heavy Snowfall Zones and Special Heavy Snowfall Zones, http://www.mlit.go.jp/common/001085702.pdf, 2018.

[2] Aviation and Railway Accident Investigation Committee, "East Japan Railway Company Tadami Line between Hayato Station and Aizu Mizunuma Station," *Train Derailment Accident Railway Accident Investigation Report*, Report No. RA2006-2-4, 2006 (in Japanese).

[3] Japan Meteorological Agency, Ministry of Land, Infrastructure, Transport and Tourism: Regional Weather Observation System Public Information, http://www.jma.go.jp/jma/menu/menure port.html, 2019.

[4] Iikura, S., et al., "Development of Estimation Method for Runoff from the Bottom of Snow at Any Point using AMeDAS Data," *RTRI Report*, Vol. 36, No. 4, 2022 (in Japanese).

[5] Shimamura, M., "Improvement of train operation regulation method against rain, wind and earthquake," Doctoral dissertation, *University of Tokyo*, 2008 (in Japanese).

[6] Mizoguchi, M., and Katsura, S., "Analysis of groundwater level fluctuation in landslide areas using effective rainfall method considering snowmelt and evapotranspiration," *Journal of the Landslide Engineering Society of Japan*, Vol. 56, No. 1, pp. 16-24, 2019 (in Japanese).

[7] Takayanagi, T., Yuasa, T., and Keyaki, T., "Maintenance Method for Slope Failure Disaster in Snow Melt Season," *RTRI Report*, Vol. 31, No. 5, 2017 (in Japanese).

[8] Takayanagi, T., Sato, R., and Nunokawa, O., "Various studies on setting conditions for snowmelt disaster warning index using analytical snowmelt and effective rainfall," *Journal of Japan Society of Civil Engineers*, 77(3), 195-212, 2021 (in Japanese).

Authors

Tsuyoshi TAKAYANAGI
Senior Researcher, Geo-hazard & Risk Mitigation Laboratory, Disaster Prevention Technology Division
Research Areas: Slope Stability Analysis, Geo-hazard & Risk Mitigation, Maintenance

Osamu NUNOKAWA, Dr. Eng
Director, Head of Disaster Prevention Technology Division
Division Research Areas: Slope Stability Analysis, Geo-hazard & Risk Mitigation, Maintenance

Ryota SATO
Assistant Senior Researcher, Meteorological Disaster Prevention Laboratory, Disaster Prevention Technology Division
Research Areas: Meteorology

Development of Inverter-less Excitation Method for a Linear Rail Brake

Yasuaki SAKAMOTO   Keigo UKITA

Electrical Machines Laboratory, Maglev Systems Technology Division

Studies have been carried out on rail brakes applying linear induction motor technology. This brake is capable of generating braking force without contact. In addition to the aspect of non-contact brakes, no on-board power supply for energizing this brake is required by using dynamic braking. This dynamic braking is performed with an excitation inverter, however there is a need to have a method which does not use an excitation inverter to reduce cost. Therefore, the authors devised an inverter-less excitation method using the self-excitation phenomenon of induction generators and tested it on a track-wheel testing machine. It was clarified that the method devised is useful as a low-cost excitation system.

Key words: *rail brake, linear motor, excitation system, capacitor self-excitation phenomenon of induction machines*

1. Introduction

Eddy-current rail brakes used in railway vehicles can generate contactless braking force, independent of the frictional force (adhesion force) between wheels and rails. Although the adhesion force decreases with increasing vehicle velocity, the braking force of the rail brake decreases only slightly as vehicle velocity increases. By adding this contactless braking force to the conventional braking force based on adhesion, it is possible to stop a moving vehicle within a shorter distance and in a shorter time. The rail brake is therefore expected to be a means of enhancing safety in emergency situations. However, contactless braking has required until now to have a safeguard against loss of power supply for energization. To solve this issue, the authors devised and are conducting research and development on a linear rail brake applying the principle of regenerative braking technology of linear induction motors (LIM). The main feature of the linear rail brake is that the power required for energization can be generated by the device itself. The desired performance has already been confirmed [1].

A linear rail brake consists of three basic components: armatures, a mounting mechanism, and an excitation system. The armatures generate the power required for energization to generate the braking force. The mounting mechanism elevates and supports the armatures under the bogie. The excitation system in which an inverter is specifically used energizes armatures with AC current. Now, the linear rail brake has several issues, such as an increase in bogie weight, and one of the most important issues to be solved for practical use is the reduction of equipment cost. In this regard, of the above three components, the excitation system is considered to be a potential source of cost reduction through drastic technological replacement. If there is an excitation method other than an inverter that could maintain AC current and self-generation in a desired state, there would be no need to use an expensive inverter.

One possible candidate for an excitation method that does not use an inverter is the application of the "capacitor self-excitation phenomenon in induction machines" [2]. This phenomenon occurs because resonance with power generation occurs between coils and capacitors in the induction machine when capacitors are connected to an externally powered induction machine, resulting in spontaneous AC current flow (self-excitation). Since the linear rail brake is classified as an induction machine in the classification of electrical machines, it is in principle thought that capacitor self-excitation phenomena can occur in linear rail brakes. In the capacitor self-ex-

citation phenomenon in general rotating induction machines, a residual magnetic flux of a rotor is used, when starting from no electrical power source. Residual magnetic flux is weak magnetization remaining in the rotor core with a history of exposure to magnetic fields. In contrast, the linear rail brake is expected to have no residual magnetic flux in the rail corresponding to the rotor. Therefore, the use of capacitor self-excitation phenomenon in the linear rail brake has been considered unsuitable because of the problem of starting during power failure. As far as the authors have investigated, there are no examples of capacitor self-excitation applied to LIMs such as the linear rail brake, except for reciprocating type LIMs that can use the residual magnetic flux.

Therefore, in this paper, the authors investigated an excitation method using the capacitor self-excitation phenomenon in the linear rail brake. Specifically, a new method was devised in which the resonant capacitor is charged with DC in advance and discharged when the excitation starts. In the excitation system in this paper, this discharge is used as a "starting trigger" instead of the residual magnetic flux in rotating induction machines. The basic operational performance of this method, such as starting and stopping, was verified and the velocity characteristics were investigated. These results were evaluated in comparison with those of conventional inverter excitation, and it was confirmed that the devised method is useful as an inverter-less excitation method that realizes a low-cost excitation system.

2. Outline of Linear Rail Brake

2.1 Armature and mounting mechanism

By replacing the DC electromagnets of eddy-current rail brakes with 3-phase AC electromagnets, the linear rail brake is used as the armature of the LIM facing rails. Figure 1 shows an example of the configuration. The armature is installed in the limited space between the wheels at the front and rear of the bogie, and its maximum length is about 1.2 to 1.5 m. Note that the head width of rails used in trunk lines section is 65 mm. These figures limit the size and shape of the LIM, which has to be very elongated. In addition, since the secondary side for LIM is an iron ingot rail, the skin effect makes it difficult for magnetic flux and eddy current to enter the inside of the rail cross section from a low slip frequency. For these reasons, LIM linear rail brakes have large leakage reactance, large secondary re-

sistance, and strong non-linearity impedance with respect to the magnitude of the current.

The mounting mechanism keeps the armature raised just below the bogie frame when the brake is not in operation. There is no electromagnetic interaction between the armature and the rail. On the other hand, when the brake is in operation, the mounting mechanism lowers the armature to maintain the gap with the rail at a predetermined value.
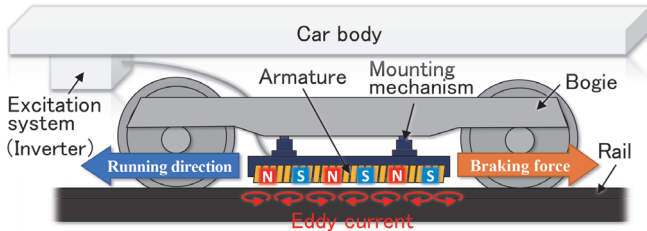

Fig. 1   Example of linear rail brake configuration

2.2 Excitation system

The excitation system is mounted on the car body and performs dynamic braking by energizing the armatures. If the supply of power to an inverter and power consumption of the dynamic braking are managed by a main onboard circuit, feeder system failure or regeneration cancellation may affect the excitation system. This means that such an excitation system would be unreliable as a braking system. Therefore, the excitation system of the linear rail brake is completely separated from the main circuit during braking and is configured to operate independently.

2.3 Excitation operation by inverter

A conventional excitation system uses an inverter. Figure 2 shows an example of an excitation system configuration with an inverter per bogie. First, the smoothing capacitor is charged in advance with a control circuit voltage (DC 100 V) or similar, at vehicle startup. This enables dynamic braking to start even in the event of a power failure. The inverter starts 3-phase excitation with the charged power of the smoothing capacitor at initial excitation. Then the voltage of the smoothing capacitor rises with the power generated immediately after the start of excitation. This increase in capacitor voltage increases the AC voltage output of the 3-phase excitation to increase the braking force. After reaching the prescribed smoothing capacitor voltage, the inverter balances the generated power and overall circuit losses by operating at a higher slip frequency (lower inverter frequency) while maintaining the braking force. In this way, the inverter can maintain a constant smoothing capacitor voltage without using a braking resistor or other devices. This excitation method is called "dynamic braking with zero electrical output." The reason for using a high slip frequency as the operating point is to reduce the inverter capacity for prescribed braking force.

The slip frequency of the "dynamic braking with zero electrical output" described above is very different from the one in vector control used for variable speed control of general induction machines. Therefore, the impedance characteristics of the armature also differ significantly. In particular, velocity dependence and slip frequency dependence of the impedance in a high slip frequency are small in the high-velocity region beyond a predetermined vehicle velocity. Taking advantage of these features, a simple control method is adopted, in which the output current command I^* and the fre-

quency command f_{ref}^* are regarded as the brake force command and the generation power command, respectively. This control method can adjust the brake force and the smoothing capacitor voltage V_{dc} to predetermined values, without using the vehicle velocity information (Fig. 3).

In the high-velocity region, the change in frequency f_{ref}^* for adjusting the capacitor voltage V_{dc} is not large with respect to the change in velocity (Fig. 4). This is based on the aforementioned feature of less velocity dependence of impedance.

In most cases, the brake force is required to be as large as possible. Therefore, the current command I^* is often the maximum value that can be energized by self-generated power. In that case, the inverter outputs an AC voltage fixed at the maximum modulation rate, so that the output current I is approximately proportional to the value obtained by dividing the smoothing capacitor voltage V_{dc} by the frequency f_{ref}^*. Normally, the smoothing capacitor voltage V_{dc} is controlled at a constant command value V_{dc}^*, and the frequency f_{ref}^* is commanded to adjust the generated power. This leads to the behavior that "when the generation performance of the armature decreases (increases), the frequency f_{ref}^* increases (decreases) and the output current I decreases (increases)."
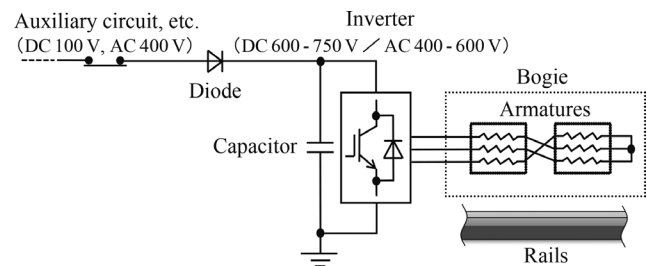

Fig. 2   Conventional excitation system with inverter

3. Study of low-cost excitation system

3.1 Principle of capacitor self-excitation and new starting method

The capacitor self-excitation phenomenon in typical rotating induction machines is as follows:
(1)   Rotor cores in electric motors or generators have a weak residual magnetic flux. When the rotor is turned by external mechanical power, the rotation of the residual magnetic flux induces an AC voltage in the armature circuit.
(2)   The induced AC voltage causes a weak AC current to flow in the armature circuit. This is the same principle as in a permanent magnet synchronous generator.
(3)   When a capacitor is connected to the armature circuit, the above weak AC current flows to excite the induction machine at a resonant frequency of the armature coil and capacitor. This makes the induction machine begin to operate as an induction generator.
(4)   The current gradually increases with the generated power, but eventually magnetic saturation of the iron core occurs. As a result, the increase in generated power is insufficient for corresponding increase in current.
(5)   Eventually, the current converges to a magnitude at which the generated power and the overall circuit losses are balanced and maintained.

"Dynamic braking with zero electrical output" by an inverter in the linear rail brake also balances the generated power and the over-
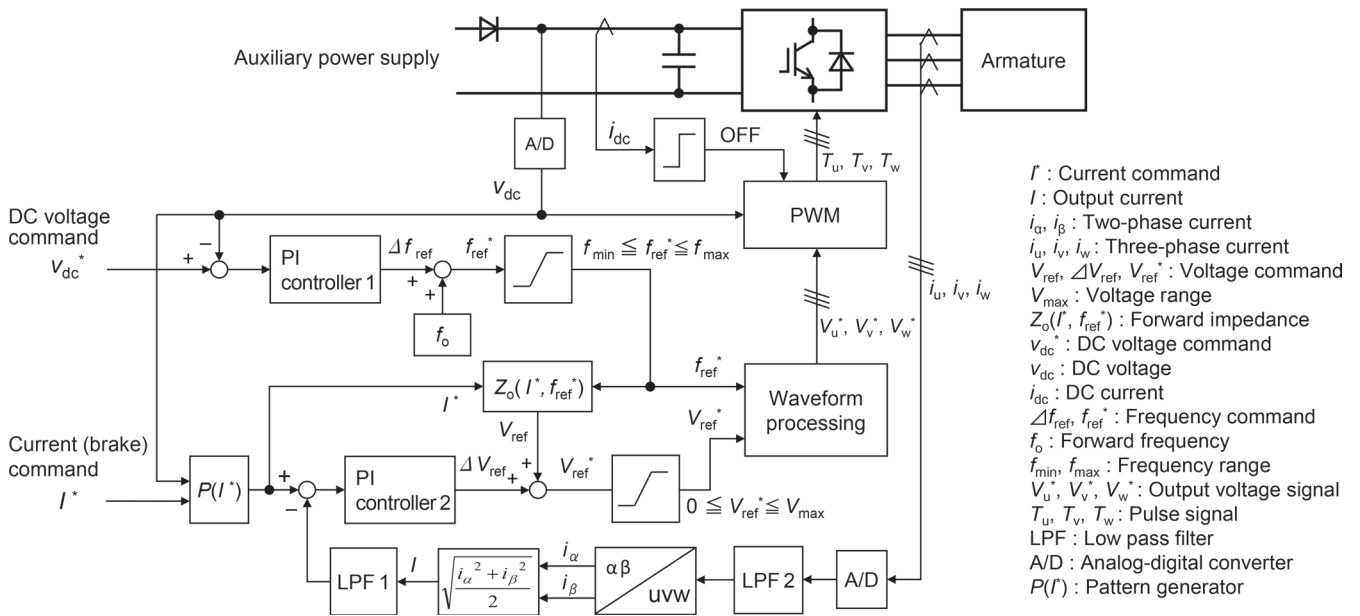
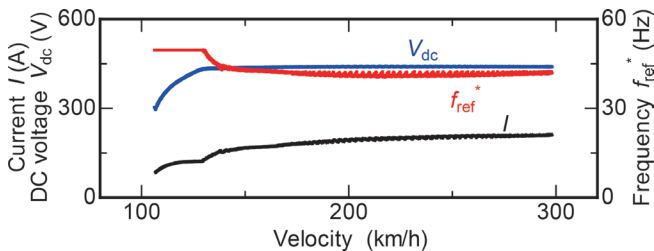**Fig. 3 Basic control block for conventional inverter excitation**

Fig. 4 Example of velocity characteristics of conventional inverter excitation

all circuit losses in the same way as in (5) above. This inverter works to provide reactive power to the armature. This suggests that the inverter can be replaced with a capacitor, which can generate inductive power through the self-excitation phenomenon described above. However, in the linear rail brake, since there is no "residual magnetic flux of the rotor core in LIM, there is no "starting trigger." Therefore, simply connecting a capacitor does not cause a self-excitation phenomenon.

To solve this problem, we devised a starting method to forcible induce a self-excitation phenomenon in the linear rail brake. In the devised method, a resonance capacitor is charged with DC power in advance and the charged power is discharged to armature coils at the start of excitation (Fig. 5). The specific procedure is to charge the capacitor by operating "contactor 1 CLOSE, contactor 2 OPEN" at vehicle startup; then stand by with "contactor 1 OPEN, contactor 2 OPEN" until the start of the excitation. Then, excitation is started by operating "contactor 1 OPEN, contactor 2 CLOSE." The capacitor capacitance should be selected so that the resonance frequency of the capacitor and armature coils coincides with the frequency at which the generated power and the loss of the entire circuit are balanced. This frequency is almost the same as the equilibrium frequency of "dynamic braking with zero electrical output" in inverter excitation.

Immediately after the "contactor 2 CLOSE," a current flows like a single-phase AC on the α-axis in Fig. 5 due to the release of capacitor-charging power. This single-phase AC current generates

an alternating magnetic field, standing waves of N and S poles, in the gap between the armature and the rail (Fig. 6). This standing wave is a superposition of a traveling wave and a backward wave. The traveling wave (positive-phase-sequence component) moves in the same direction as the one of rail travel seen from the armature. The backward wave (negative-phase-sequence component) moves in the opposite direction. Since the traveling wave has a power generation effect, current is also induced on the β-axis, and the three-phase positive-phase-sequence current (UVW) increases. This increasing positive-phase-sequence current is the same as the currents in (3) and (4) above, and finally becomes as described in (5). On the other hand, since the backward wave has no power generation effect, the three-phases negative-phase-sequence currents (WVU) decay and eventually dissipate.

As described above, the devised method does not follow the starting process in (1) and (2), which are the same process as a permanent magnet synchronous generator. On the other hand, the method follows the starting process in (3) with the negative-phase-sequence current superimposed. By increasing the charging voltage of the capacitor, the current flowing immediately after "contactor 2 CLOSE" can be increased, which has the advantage of reducing the time in the current increasing process in (4). Therefore, the devised method is an effective starting method for reducing the idle time in brake devices that use the capacitor self-excitation phenomenon. Then, if the capacitor is charged after the vehicle startup and prevented from discharging, this starting method can be used in the event of a power failure without using a battery or something similar.

3.2 Excitation shutdown and self-protection function

To stop excitation, contactor 2 in Fig.5 is opened. This prevents the current in the α-axis from flowing. On the other hand, the current in the β-axis is still able to flow. However, since the current in the β-axis alone is energized as a single-phase AC current, it does not provide generated power, decays and finally disappears. Thus, the α-axis and β-axis stop excitation separately.

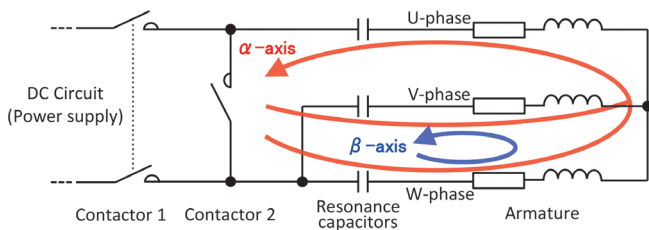When a snubber circuit is attached to contactor 2 (see below),

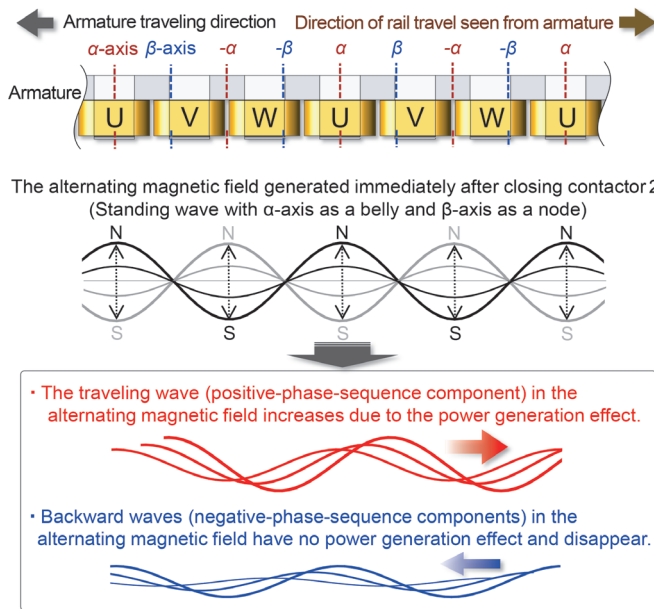**Fig. 5 Devised starting method for capacitor self-excitation**

Fig. 6 Conceptual diagram of magnetic field distribution at start of excitation

the resonant frequency of the current on the α-axis transitions to a different frequency with the addition of the snubber capacitor. Hence, the resonance frequency in the α-axis and that in the β-axis become different. In this case, alternating magnetic fields of different frequencies are generated on the α and β axes, respectively. Since these alternating magnetic fields do not generate power, they eventually decay and disappear (The same thing occurs in the case of the delta connection described below.).

The above describes the case where the contactor is actively operated. Meanwhile, capacitor self-excitation is sustained only when the positive-phase-sequence component in the three-phase circuit flows in the resonant state. Therefore, if resonance state cannot be maintained due to a ground fault or short circuit, the current flow is automatically stopped. That is, capacitor self-excitation has a self-protective function. Particularly for ground faults, if the electrical neutral point of the armature circuit is grounded, the ground fault current always passes through the armature coils until it stops due to self-protection. This gives some current-limiting effect to the ground fault current by the inductance of armature coils.

3.3 Basic circuit configuration

Figure 5 is a simplified diagram explaining the starting method of the devised capacitor self-excitation. In this section, we consider circuit configurations that satisfy the following conditions for the

purpose of reducing costs:

* A minimum of 2 contactors.
* The configuration should be able to use the armature impedance instead of the charging resistance required in the initial stage of capacitor charging.
* Self-excitation can be stopped by opening contactor 2 during self-excitation. In this case, it is best if a snubber circuit is not required, although one can be installed if necessary.

Considering the above conditions, two basic circuit configurations shown in Fig. 7 have been proposed.

Figure 7(a) shows a Y-connected capacitor configuration. The advantage of this configuration is that since the initial charging voltage of the capacitor can be increased up to the rated voltage of the armature, the excitation starting time can be reduced. On the other hand, the disadvantage is that a snubber circuit must be installed because of the possibility of a relatively large arc when contactor 2 is opened while current is flowing.

Figure 7(b) shows a Δ-connected capacitor configuration. The advantage of this configuration is that even if contactor 2 is opened while current is flowing, the arc is kept small because there is a current bypass. Therefore, a snubber circuit is not necessary. Incidentally, only one capacitor is initially charged in this configuration. When contactor 2 is closed as excitation starts, a circulating current flows in the delta-wiring circuit consisting of the three capacitors just before discharging to the armature side. As the result, distribution of the capacitor voltage then occurs. This circulating current is limited only by the parasitic inductance of the delta-wiring circuit. Therefore, it is necessary to limit the initial charging voltage of the capacitor to an appropriate magnitude so that the circulating current does not become excessive. This initial charging voltage limitation gives us the disadvantage of this configuration that it is difficult to reduce the excitation starting time significantly.

As described above, Fig. 7(a) is suitable for the requirement to increase the initial charge voltage of the capacitor to shorten the starting time as much as possible. On the other hand, Fig. 7(b) is suitable for a simple circuit configuration by omitting the snubber circuit.

3.4 Feature comparison of inverter excitation with capacitor self-excitation

Table 1 shows the results of the comparison of the conventional inverter excitation with the devised capacitor self-excitation. This table shows that the "Operation and Behavior at startup" is similar for the two excitations, except for the presence of negative-phase-sequence component in capacitor self-excitation. On the other hand, as for "Operation and Behavior at steady-state," the causal relationships among current, frequency, and generated power differ between the two excitations. In particular, the relationship between the increase/decrease in frequency and the increase/decrease in generated power is reversed for both excitations. That is, the behavior of inverter excitation and capacitor self-excitation will be different when state changes occur that directly affect the power generation capability, such as a significant change in velocity or a change in gap.
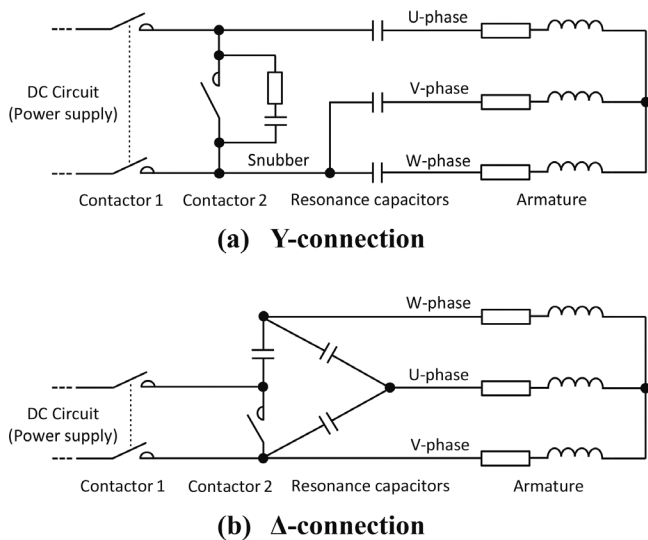
(a) Y-connection

(b) Δ-connection

Fig. 7   Basic circuit configuration examples

4. Verification test

4.1 Test Equipment

The performance of capacitor self-excitation in the previous section was verified in a track-wheel testing machine [3]. A prototype linear-rail-brake armature (Fig. 8(a)) with a circular arc shape was used for the testing machine. This prototype is designed to be the size of a practical machine, including protective covers, etc.

(length of less than 1500 mm, width of less than 125 mm, and height of less than 130 mm when converted to a straight-line shape). The pole pitch is about 200 mm and the nominal gap is about 8 mm. The capacitance of the capacitors used in the tests is 6 mF (Y-connected) or 2 mF (Δ-connected) per phase. These capacitances are matched with the equivalent capacitance of the inverter when the one is used for excitation. Thus, the capacitors are selected so that performance can be compared with "the dynamic braking with zero electrical output" by the inverter. Prototype unit capacitors has been manufactured to configure the above capacitances. These are made to be usable at higher voltages than inverter excitation so that the improvement of braking force and the reduction of capacitance can also be tested on a trial basis. The specifications of the unit capacitor are 0.5 mF per phase (Δ-connection), and the external dimensions of the three phases together are approximately 350 mm × 200 mm × 300 mm, with a mass of approximately 40 kg. The external appearance is shown in Fig. 8(b).

The basic test procedure is as follows: First, the track wheel is rotated at a predetermined velocity by the motor directly connected to the rotating shaft. Then, when the linear rail brake starts braking operation, and at the same time, the track wheel is also decelerated by the motor. During that deceleration, the starting and velocity characteristics of the capacitor self-excitation are obtained.

4.2 Starting characteristics test

Figure 9 shows the current waveforms when contactor 2 is closed after the capacitor is initially charged. They are shown for each of the states in which the track wheel is stopped (0 km/h) and rotated at 300 km/h. In the stopped state, the discharge current flows

Table 1   Comparison of inverter excitation with capacitor self-excitation

		Inverter excitation	Capacitor self-excitation
Operation and Behavior	**Startup**	*The DC charging power of the smoothing capacitor is used to energize positive-phase-sequence current through the 3-phase circuit.*	*The DC charging power of the resonant capacitor is used to energize single-phase AC current with superimposed positive- and negative-phases-sequence through the 3-phase circuit.*
	Steady state	*Frequency is controlled to maintain the smoothing capacitor voltage constant.* *Increasing (decreasing) the frequency increases (decreases) the generated power.* *Increasing (decreasing) frequency decreases (increases) current at maximum modulation factor output.*	*At the resonant frequency, the magnitude of the current naturally converges so that the generated power and losses are in equilibrium.* *As the current decreases (increases), the generated power increases (decreases) relative to the losses.* *As the current decreases (increases), the magnetic saturation state changes and the resonant frequency decreases (increases).*
Advantage		*Advanced control such as braking force control* *Possible to add functions such as trial energization while the train is stopped and armature condition monitoring while the train is running*	*Simplification of system configuration and cost reduction* *Potential for mass reduction* *High reliability due to uncontrolled operation* *No EMC noise due to PWM switching* *Lower loss and higher braking force than inverter*
Disadvantage		*Expensive equipment cost* *EMC noise due to PWM switching*	*Not many things that can be checked by trial energization (discharge from capacitor to armature) while the car is stopped* *Need to devise a method to monitor armature condition.*
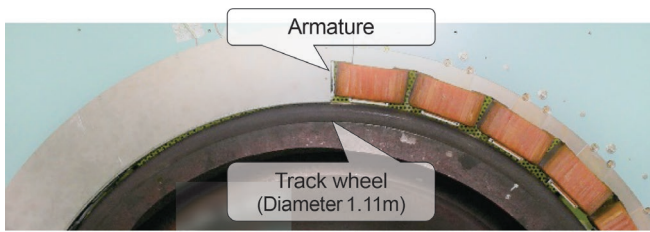
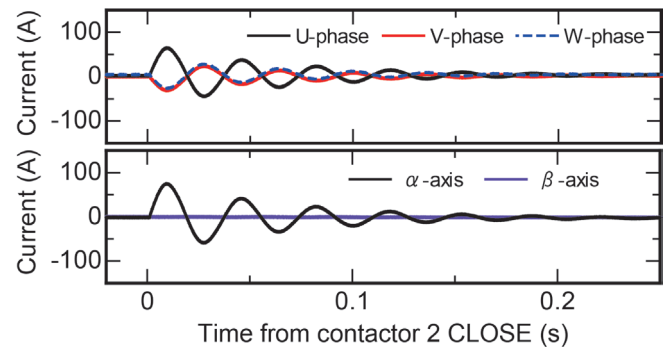**(a) Armature and track wheel**
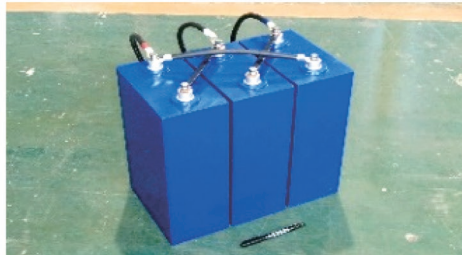
(b) Capacitor

Fig. 8　Appearance of test equipment

(a) 0 km/h

(b) 300 km/h

Fig. 9　Current waveforms at startup (Y-connection, initial charge DC 100V)

Fig. 10　Rise in current at startup (Y-connection, initial charge DC 300 V)

like a single-phase AC current that decays only in the α-axis and is dissipated. On the other hand, at 300 km/h, as for the period immediately after contactor 2 is closed, the current flows like a single-phase AC current on the α-axis. However, it soon begins to flow in the β-axis as well, becoming like a 3-phase AC, and the amplitude is increasing. This confirms that the negative-phase-sequence component is attenuated, and the positive-phase-sequence component is increased, as described above. The rise in current rms in the starting test compared with that of inverter excitation is shown in Fig.10. In this test, the initial charge voltages of the resonant capacitor for capacitor self-excitation and the smoothing capacitor for inverter excitation are aligned. This figure shows that the capacitor self-excitation current rises in about 0.3 seconds (0-90%) and then becomes a constant value. It can be confirmed that the rise in capacitor self-excitation is fast enough for practical use. The speed of the rise in inverter excitation cannot be quantitatively evaluated as a general result since it is related to various conditions such as smoothing capacitor capacitance. Nevertheless, it is certain that the speed of the rise in capacitor self-excitation is generally equal to or faster than that of inverter excitation.

4.3　Shutdown test and self-protection test

Figure 11 shows the current waveforms when contactor 2 is opened while the current is flowing with capacitor self-excitation (Δ-connection) at a velocity of 300 km/h. Immediately after opening contactor 2, the two frequencies are mixed, and the current is attenuated and dissipated in about 0.4 seconds. As mentioned above, the resonant frequencies of the α- and β-axes are different, resulting in two single-phase AC currents with no power generation capability, and the self-excitation becomes unsustainable and stops. Note that several tests have confirmed that the arc at the opening of contactor 2 is small. In addition, a shutdown test with a snubber circuit attached to contactor 2 in the Y-connection capacitor was carried out and obtained the same results as in Fig. 11.

Figure 12 shows the current waveforms when one of the input terminals of the armature (the part with the highest electric potential to ground) is artificially grounded while the current is flowing with capacitor self-excitation (Δ-connection). Contactor 2 is left closed.
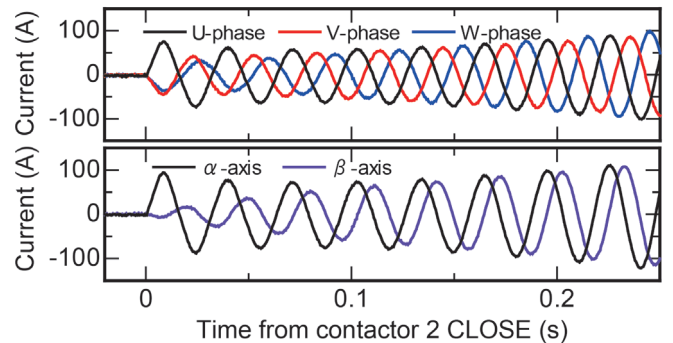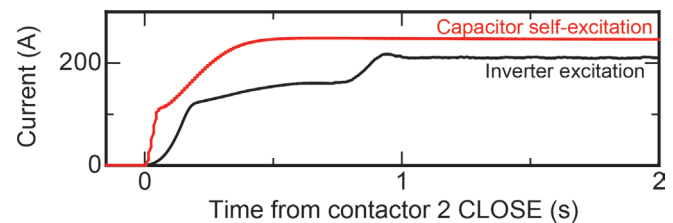
The most severe condition is set as a complete ground fault with direct grounding without any resistance. Figure 12 shows that within three cycles (approximately 20 ms) after the occurrence of a ground fault, a ground fault current of 250% of the steady-state current flows at maximum, it soon disappears. Thereafter, excitation is stopped by approximately 0.3 seconds after the occurrence of the ground fault. This indicates that in the event of a ground fault, this characteristic will quickly stop the excitation as a self-protection function. This is effective when the opening of contactor 2 as an active protective action is delayed for some reason.

4.4　Velocity Characteristics

Figure 13 shows the velocity characteristics of capacitor self-excitation when excitation is started at 300 km/h compared with inverter excitation. Although capacitor self-excitation is uncontrolled, it can be excited at a wider range of velocities than inverter excitation controlled actively. Since the linear rail brake is operated at a high slip frequency, less frequency adjustment is required in adjusting the amount of power generation due to changes in veloci-
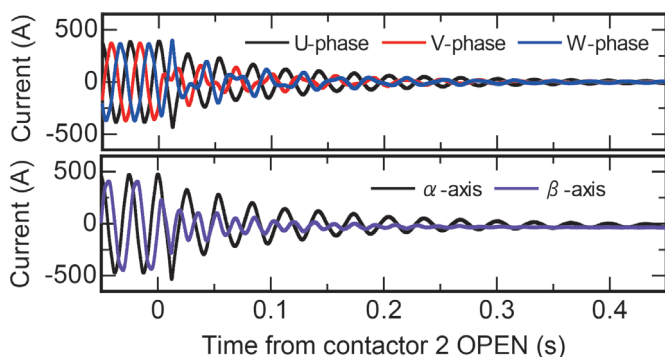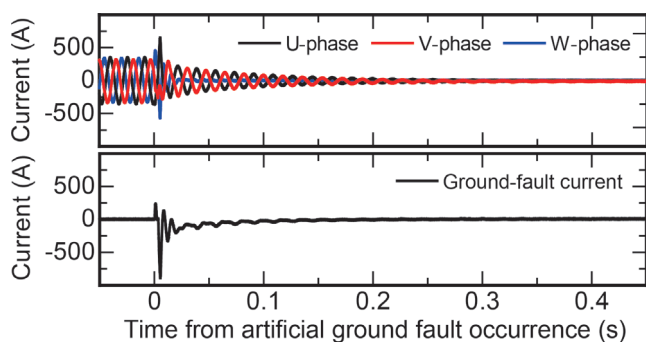
Fig. 11 Shutdown test (Δ-connection)

Fig. 12 Self-protection test against artificial earth fault (Δ-connection)

Fig. 13 Velocity characteristics (Δ-connection, max. AC 300V)

ty. Therefore, capacitor self-excitation, which operates at a resonant frequency that is passively determined and does not change noticeably, is easily applied to the linear rail brake. In detail, as the velocity decreases, the generating capability decreases and the current gradually decreases. However, the degree of current decrease is equivalent to that of inverter excitation in which the decrease in generating capability is compensated by operation to increase the frequency. The resonant frequency is slightly decreased with decreasing current, due to the smaller effect of magnetic saturation. This change in frequency is the opposite of the frequency operation in inverter excitation. It has the effect of preventing the slip frequency from decreasing too much in the low-velocity range (below about 110 km/h). Therefore, it is suitable for continuing excitation down to lower velocities. In addition, the capacitor self-excitation produces a larger current flow and a larger braking force. This is because in capacitor self-excitation, the power loss during energization is small and the generated power can be effectively used as power to energize the system. From the above, it is confirmed that the braking performance of capacitor self-excitation exceeds that of inverter excitation in the entire velocity range where excitation is possible.

5. Conclusion

The authors devised a novel excitation method using the capacitor self-excitation phenomenon to reduce the cost of a linear rail brake, and verified its performance on a track-wheel testing machine. It was confirmed that the devised excitation method is as fast as or faster than conventional inverter excitation in terms of startup and can be used for a wider range of velocity. The devised excitation method also generated a greater braking force than the inverter excitation at all possible excitation velocities. From these results, it was confirmed that all of the starting, stopping, and velocity characteristics of the devised excitation method are applicable to practical use. By replacing inverters in conventional excitation systems with this novel excitation method proposed in this paper, significant cost reductions can be expected.

References

[1] Sakamoto, Y., Kashiwagi, T. et al., "Development of a Rail Brake Derived from Linear Motor Technology," *Quarterly Report of RTRI*, Vol. 55, No. 2, pp. 105-111, 2014.
[2] R. C. Bansal, "Three-phase self-excited induction generators: an overview," *IEEE Transactions on Energy Conversion*, Vol. 20, No. 2, pp. 292-299, 2005.
[3] Sakamoto, Y., Kashiwagi, T. et al., "Performance of Linear Motor Type Rail Brake Using Roller Rig Test Bench," *Quarterly Report of RTRI*, Vol. 53, No. 1, pp. 41-45, 2012.

Authors

Yasuaki SAKAMOTO, Ph. D.
Senior Chief Researcher, Head of Electrical Machines Laboratory, Maglev Systems Technology Division
Research Areas: Electromagnetic Systems, Linear Motors

Keigo UKITA
Assistant Senior Researcher, Electrical Machines Laboratory, Maglev Systems Technology Division
Research Areas: Electrical Machines, Electromagnetic Applications

Fabrication and Characterization of High-temperature Superconducting Materials with High Magnetic Field

Tomoyuki AKASAKA

Superconductivity and Cryogenics Laboratory, Maglev Systems Technology Division

Atsushi ISHIHARA   **Kenji SUZUKI**

Applied Superconductivity Laboratory, Materials Technology Division（Former）

Masaru TOMITA

Maglev Systems Technology Division

Since superconducting bulk material is compact and can generate a strong magnetic field, and has the potential to be used in various devices as a magnetic field generation source. High magnetic field strength, magnetic field uniformity, and magnetic field stability are required to able to used superconducting bulk material in magnets. In order to achieve these demanding characteristics, we produced MgB_2 and RE-based superconducting bulk material to evaluate their properties.

***Key words**: high temperature superconductivity, superconducting bulk, critical current, magnetic field*

1. Introduction

Currently, there are two main specific applications of superconducting materials : electric wires and bulk magnets. The main kind of superconducting bulk magnet developed to date use rare-earth (RE)-based superconductors. A magnetic field generated by a common permanent magnet is less than 1 T. On the other hand, magnetic field generated by a RE-based superconducting bulk magnet can achieve 17 T [1]: a magnetic field capable of lifting one ton of iron per square centimeter. Superconducting bulk magnets have the potential of being applied to and significantly improving the performance of magnetic bearings, current leads, magnetic field sources for analyzers, and magnetic transport of chemicals.

Since a superconducting bulk magnet has a high critical current density even under a high magnetic field, it can trap a high magnetic field. It is more compact and less costly than a superconducting coil magnet and can generate a higher magnetic field than permanent magnets and electromagnets. RE-based superconducting bulk magnets have a high current density even at the liquid nitrogen temperature 77.3 K, the lowest temperature at which superconductivity can be practically maintained, hence, even with non-refrigerator cooling with liquid nitrogen, benefit can be drawn from these characteristics.

However, producing RE-based superconducting bulk is time-consuming due to the crystal growth process. As a new material without such a problem, we have been developing magnesium diboride (MgB_2) [2-4]. The developed material has the highest critical temperature among metal-based superconductors, and possesses a high critical magnetic field and critical current density. In addition, this material is easy to manufacture, is extremely light weight, and can be processed into various shapes, increasing the range of possible applications, especially for magnetic resonance imaging (MRI) and nuclear magnetic resonance (NMR), which require high magnetic field uniformity. This paper reports on the evaluation of MgB_2 bulks and RE-based superconducting bulks and development of high-level properties.

2. Production and characterization of high-temperature superconducting materials

In order to apply a superconducting bulk to a magnet, it is necessary to have superconducting bulk with a high magnetic field and uniform trapped magnetic field. This chapter describes how these high-level properties were developed.

2.1 Production of MgB_2 superconducting bulks

Mg powder and B powder were mixed in an agate mortar, uniaxially pressed into pellets at 9.8×10^7 Pa, and sintered at 850°C for three hours in a flow of Ar. Figure 1 shows an example of produced MgB_2 bulks (20 mm$\varphi \times$10 mm). No cracks were observed on the surface of the fabricated samples.

Fig. 1   A fabricated MgB_2 bulk

2.2 Observation of MgB_2 bulks

In order to evaluate the uniformity of the fabricated MgB_2 bulks, they were observed with an optical microscope, a scanning electron microscope, and X-ray CT. Figure 2 shows optical microscope images before and after the sintering. Before sintering MgB_2 bulk, red-brown boron and silvery magnesium were uniformly mixed. After sintering MgB_2 bulk, only blue-black MgB_2 was observed. Figure 3 shows an electron microscope image of MgB_2. MgB_2 particles with a diameter of several μm were bonded at the

contact surface and these bonds will be superconducting current paths. The voids of about 1 μm were created due to the Mg diffusion during sintering. Figure 4 shows an X-ray CT image. The voids were uniformly dispersed. This result also indicates that the raw materials were sufficiently mixed and fully reacted to form MgB$_2$.
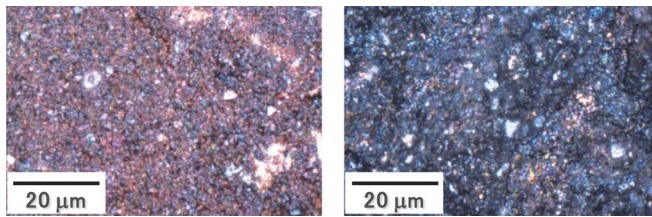

Fig. 2 Optical microscope images
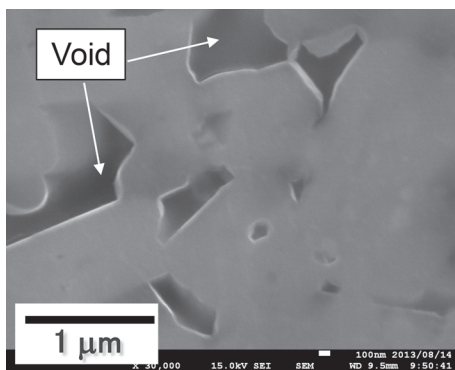**(Left: before the sintering, Right: after the sintering)**
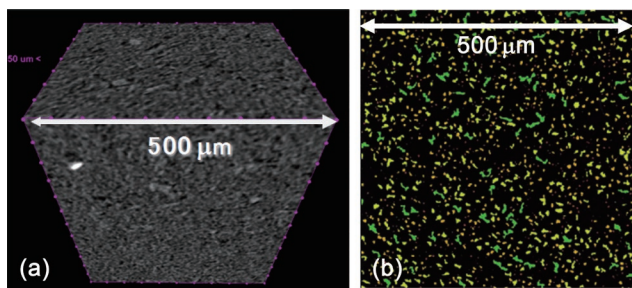

Fig. 3 Electron microscope image of MgB$_2$

Fig. 4 Internal observation image of MgB$_2$
(a): X-ray CT image, (b): Image showing only voids

2.3 Processability of MgB$_2$ bulks

When a superconducting bulk is applied to a device, it must be processed into the desired shape. For instance, a tile shape covering the magnet area is needed when applied to the magnetic separation and a semicircular shape is needed when applied to the angulator. Therefore, the processing properties of MgB$_2$ were examined. Figure 5 (left) shows MgB$_2$ samples processed into square or triangular shapes with the precision cutter. The surface and the corner of the samples were observed with an electron microscope, and no cracks were observed. The reason is probably that its filling rate was 50%, conferring low hardness.

Figure 5 (right) shows the 20 mmφ and 60 mmφ MgB$_2$ samples with 9 mm and 30 mm holes drilled with the drilling machine, respectively. They were observed with a laser microscope and a missing of 150 mm width and 70 mm depth on the surface was found.

However, this small hole does not affect the magnetic properties of the sample. Therefore, MgB$_2$ has excellent processability: an advantage for different applications.
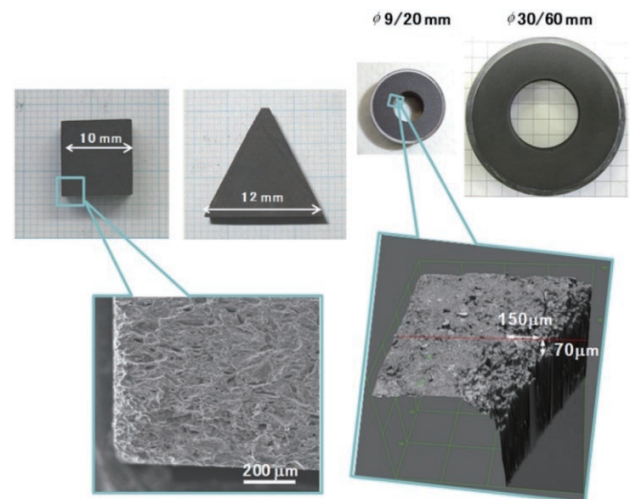
Fig. 5 Processability of MgB$_2$ bulk

2.4 Superconducting properties of the MgB$_2$ bulk

The susceptibility, the critical current density, and the trapped field of MgB$_2$ were measured. Figures 6 and 7 show the temperature dependence of susceptibility and critical current density of samples cut out of various parts of the fabricated 30 mmφ MgB$_2$ bulk. These values were measured with SQUID. There was little difference in the susceptibility and critical current density of each sample. The magnetic and electrical properties of MgB$_2$ were uniform throughout the bulk. Figure 8 shows the temperature dependence of trapped fields at the two points: on the surface of the sample and between the samples measured by hall device following the refrigerator cooling to 10 K and the magnetization in the field of 6 T. The diameter of the samples is 30 mm. The temperature was measured at the bottom of the sample. The trapped fields were about 4 T at 11 K, 3 T at 20 K, 2 T at 25 K. Considering that the trapped field did not saturate at low temperatures, further cooling may increase the trapped field.
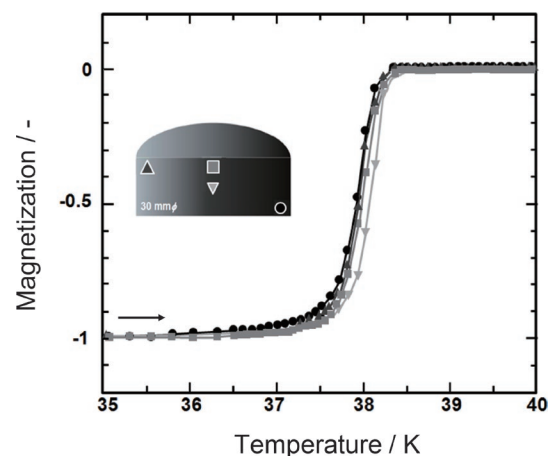

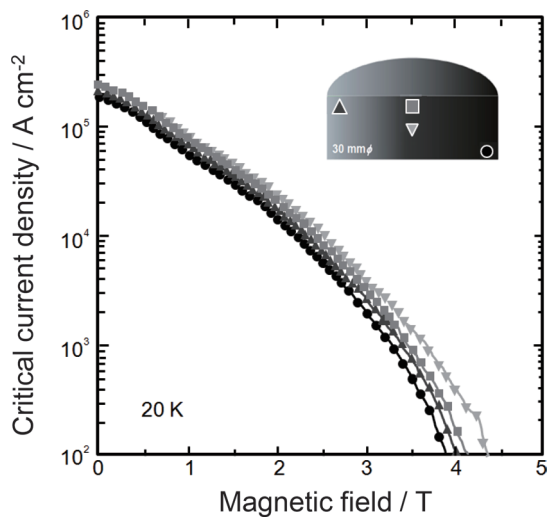**Fig. 6 Magnetization vs. temperature characteristics of MgB$_2$ bulk**

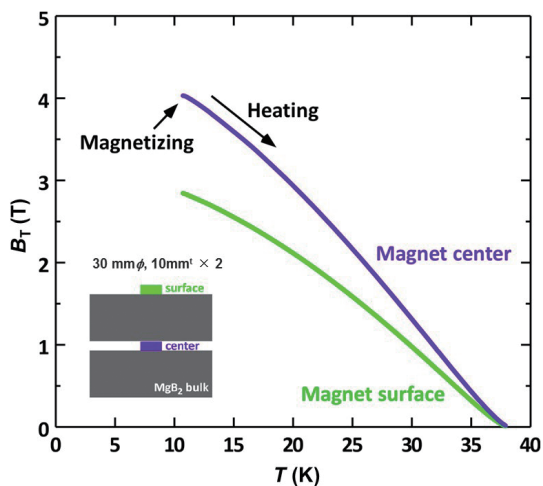**Fig. 7 Critical current density vs. magnetic field characteristics of MgB$_2$ bulk**

Fig. 8 Magnetic field vs. temperature characteristics of MgB$_2$ bulk

2.5 Uniformity of the trapped field for MgB$_2$ bulks

According to the critical state model, the critical current density determines the gradient of the trapped field. Therefore, when the trapped field of a circular sample is measured, if the contours of the trapped field are circular and evenly spaced, there is a uniform critical current density throughout the sample. Two-dimensional scans of the trapped field were performed using a steering Hall probe at a height of 3 mm on a 30 mm diameter MgB$_2$ bulk. Figure 9 shows the position dependence of the trapped field. Figure 10 shows the radial position dependence of the trapped field. The contours are circular and evenly spaced except around the center where the slope of the trapped field becomes gentle. Hence, the critical current density was uniform almost everywhere in the sample.

2.6 Visualization of the magnetic field

A magneto-optical imaging method was applied to visualize the magnetic field of the superconducting bulk [5]. Light rotates its polarization when it passes through a magnetic field. The magneto-optical sensor uses this effect to visualize magnetic fields. Figure 11
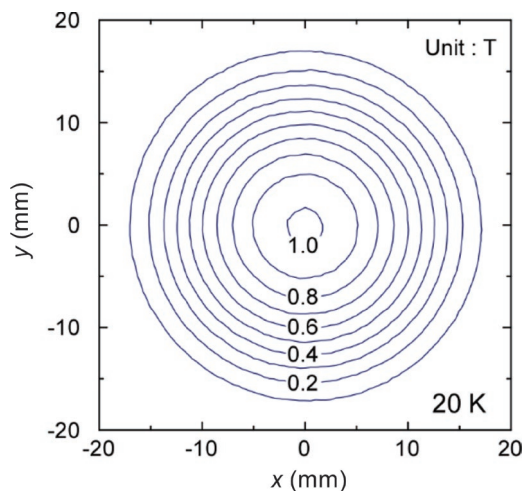
Fig. 9 Position dependence of the trapped field
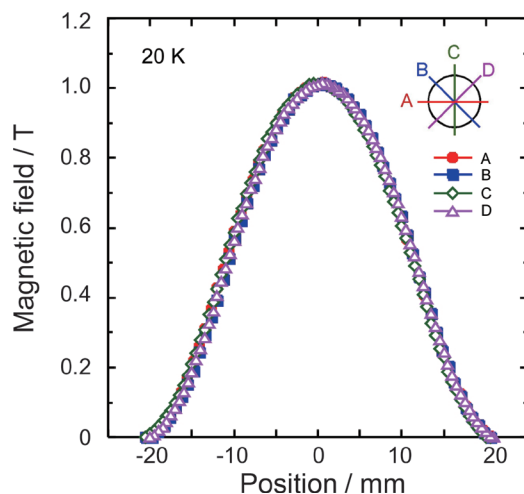
Fig. 10 Radial position dependence of the trapped field

shows a magneto-optical device. It consists of a light source, a polarizer, a magneto-optical sensor, a superconducting bulk, and a refrigerator to cool the bulk. Figure 12 shows the magneto-optical image of ring-shaped RE-based superconducting bulk. The trapped field under a zero field is shown on the left, and the diamagnetism effect under an applied field is shown on the right. The larger the magnetic field is, the brighter the yellow becomes. The magneto-optical images reflect the circular shape of the trapped field and the ring shape of the magnetic field cancelled by the diamagnetism.
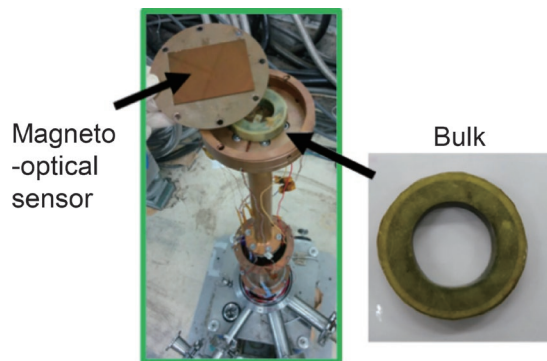
Fig. 11 Magneto-optical device
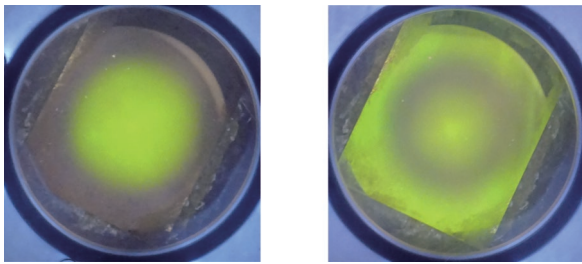
Fig. 12 Magneto-optical image of ring-shaped RE-based superconducting bulk
(Left: Magnetization characteristics, Right: De-magnetization)

2.7 Improvement of heat dissipation property of superconducting bulks

While a superconducting bulk is magnetized, the movement of the magnetic flux causes heat. If this heat is not sufficiently released from bulk, a flux jump occurs and the superconducting bulk is not magnetized. Therefore, it is important to improve the heat dissipation property of superconducting bulk to improve the magnetization property. As methods to improve the dissipation property of the RE-based superconducting bulk, we applied the alloy spraying method and the metal impregnation method. Figure 13 shows the alloy spraying method. The hot melted alloy was sprayed to the room-temperature bulk, was cooled by their temperature difference and solidified on the bulk surface. Figure 14 shows the RE-based superconducting bulk coated with alloy by the alloy spraying method. One face of the bulk was fully coated with the alloy after repeating the alloy spraying method. Figure 15 shows time dependence of temperature of the alloy-coated bulk and the uncoated bulk in liquid nitrogen after the heat was applied. The temperature rise of the alloy-coated bulk is about half of that of the uncoated bulk. The application of the alloy spraying method to the RE-based superconducting bulk may lead to improving its dissipation property in liquid nitrogen.
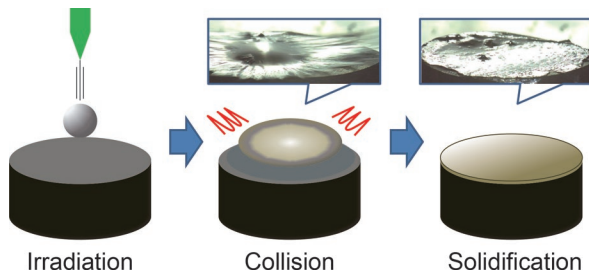
Fig. 13 Alloy spraying method
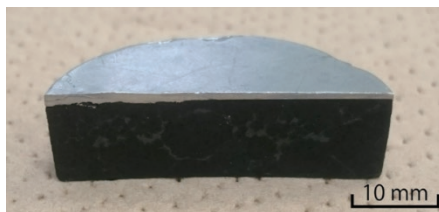
Fig. 14 RE-based superconducting bulk coated with alloy
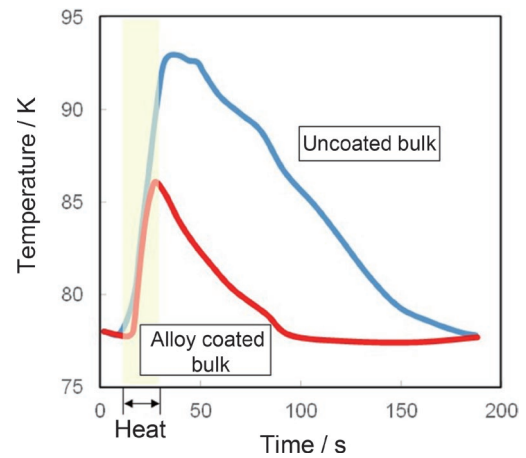
Fig. 15 Heat dissipation characteristics of RE-based superconducting bulk

As another method to improve the heat dissipation properties of a superconducting bulk, a vacuum metal impregnation method was applied. The vacuum metal impregnation method is a method to impregnate a void-rich material with a metal under a vacuum. Figure 16 shows a vacuum impregnation device. The method is applied to the fabricated MgB_2 bulks. Figure 17 shows a cross section
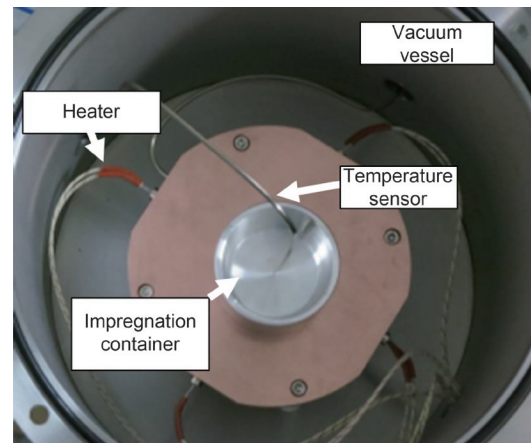

Fig. 16 Vacuum impregnation device

Fig. 17 A cross section of a metal impregnated MgB_2 bulk

of a metal impregnated MgB_2 bulk. The alloy penetrated the sample with which the average void diameter was about 50 μm to a depth of about 2 mm from the surface. This method can also improve the heat dissipation properties.

3. Conclusions

Superconducting bulks have the potential to be applied to various devices as a magnetic source due to their compactness and high trapped field. High magnetic field strength, magnetic field homogeneity, and magnetic field stability are required to apply superconducting bulk materials to magnets. In order to achieve these high-level characteristics, we fabricated a superconducting bulk material and evaluated its microstructure, workability and superconducting properties. We will continue to develop superconducting materials and their various applications.

References

[1] Tomita, M. and Murakami, M., "High-temperature superconductor bulk magnets that can trap magnetic fields of over 17 tesla at 29K," *Nature*, Vol. 421, pp. 517-520, 2003.

[2] Tomita, M. et al., "Development of MgB_2 Superconducting Bulk Magnets," *Abstracts of Cryogenics and Superconductivity Society of Japan Conference,* Vol. 87, p. 180, 2013 (in Japanese).

[3] Akasaka, T. et al., "Processing Properties of MgB_2 Superconducting Bulk Magnets," *Abstracts of Cryogenics and Superconductivity Society of Japan Conference,* Vol. 89, p. 119, 2014 (in Japanese).

[4] Ishihara, A., Akasaka, T., Tomita, M., Kishio, K., "Superior homogeneity of trapped magnetic field in superconducting MgB_2 bulk magnets," *Superconductor Science and Technology*, Vol. 30, 035006, 2017.

[5] Akasaka, T. et al., "Evaluation of trapped field distribution in high-Tc superconducting bulk magnets using MO sensor," *Abstracts of Cryogenics and Superconductivity Society of Japan Conference,* Vol. 94, p. 117, 2017 (in Japanese).

Authors

Tomoyuki AKASAKA
Assistant Senior Researcher, Superconductivity and Cryogenics Laboratory, Maglev Systems Technology Division
Research Areas: Superconducting Technology

Atsushi ISHIHARA, Dr. Eng.
Assistant Senior Researcher, Applied Superconductivity Laboratory, Materials Technology Division (Former)
Research Areas: Superconducting Technology

Kenji SUZUKI
Assistant Senior Researcher, Applied Superconductivity Laboratory, Materials Technology Division (Former)
Research Areas: Superconducting Technology

Masaru TOMITA, Dr. Eng.
Director, Maglev Systems Technology Division
Research Areas: Superconducting Technology

Evaluation of Vibration Resistance of Levitation and Guidance Ground Coils by Electromagnetic Excitation Tests Using a Superconducting Magnet

Ryohei IKEDA
Magnetic Levitation Laboratory, Maglev Systems Technology Division

Katsutoshi MIZUNO
Cryogenic Systems Laboratory, Maglev Systems Technology Division (Former)

Minoru TANAKA
Magnetic Levitation Laboratory, Maglev Systems Technology Division

During superconducting Maglev vehicles running, ground coils vibrate due to the reaction force of levitation force and guidance force. In electromagnetic excitation tests, a ground coil is vibrated under the strong magnetic field of a superconducting magnet. This paper describes an examination of test conditions based on numerical analysis, a processing method for energizing only the unit coil to be evaluated, and the electromagnetic excitation test results of the levitation and guidance coil. The vibration resistance of levitation and guidance ground coils were evaluated by electromagnetic excitation tests.

Key words: ground coils, electromagnetic excitation tests, superconducting magnet, processing method

1. Introduction

Superconducting Maglev vehicles do not have steel wheels and pantographs. They achieve an ultra-high speed of 500 km/h without any contact with the ground. It is ground coils that make this possible. Figure 1 shows the basic configuration of the superconducting Maglev system. Ground coils are electromagnets installed to the side walls of the guideway to provide propulsion, levitation and guidance forces to Maglev vehicles. There are two types of ground coils: propulsion coils and levitation and guidance coils (referred to as LG coils) [1]. Figure 2 shows the structure of molded coils. LG coils interact with superconducting magnets (referred to as SCM) to provide levitation and guidance force to Maglev vehicles. During superconducting Maglev vehicles running, ground coils vibrate due to the reaction force of levitation force and guidance force. Therefore, LG coils are required to have mechanical strength and dynamic durability against vibration.

The electromagnetic excitation test is one of durability tests for ground coils [2] [3]. In electromagnetic excitation tests, a ground coil is repeatedly vibrated under the strong magnetic field of an SCM. Alternating current is applied to the ground coil in electromagnetic excitation tests. The difference from mechanical loading is that the electromagnetic force is applied directly to the conductor of ground coils.

Levitation current is induced when SCMs pass in front of the LG coil. The circuit configuration of the LG coil does not allow the levitation current to flow directly from the cable connection terminals. For this reason, electromagnetic excitation tests have been carried out using specially designed LG coils (test coils) that can be energized separately for the upper- and lower-unit coils. However, it is necessary to use actual LG coils for estimating replacement time. An electromagnetic excitation test must be performed using an actual LG coil to evaluate the remaining life against vibration.

In this study, in order to propose electromagnetic excitation tests for actual LG coils, the condition of the tests was examined by electromagnetic field analysis and structural analysis. In addition, the circuit was changed by machining in order to conduct electricity from the cable connection terminal to only the target unit coil to be
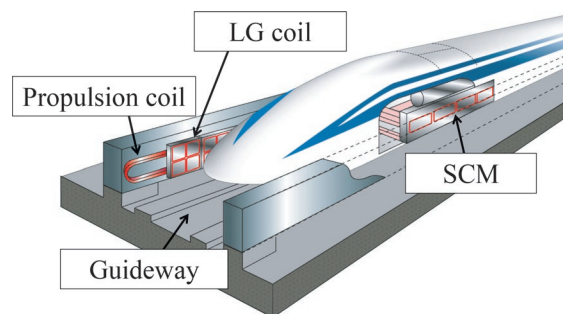

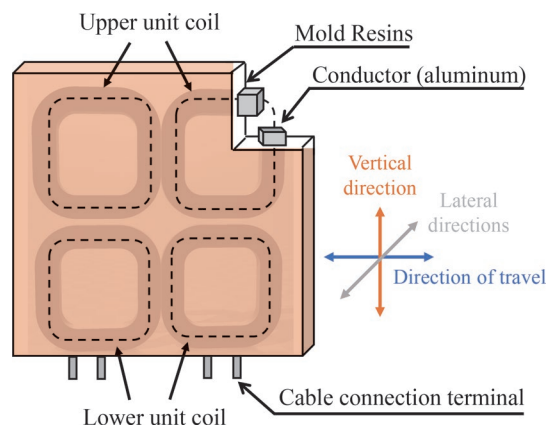**Fig. 1 Basic configuration of superconducting Maglev system**

Fig. 2 Structure of molded coils (contains two LG coils)

evaluated. The vibration resistance of LG coils was evaluated by electromagnetic excitation tests.

2. Levitation and guidance coils

2.1 Structure of levitation and guidance coils

LG coils are air-core coils without iron cores. Upper and lower rectangular unit coils are connected. Two sets of coils are put together on the left and right sides to form a molded coil. The winding coil of the aluminum conductor is integrally formed with molded resin to increase rigidity. This is to bear the electromagnetic force that repeatedly acts between SCMs and the winding coil. LG coils are fastened with nuts and bolts to both side walls of the guideway.

2.2 Electromagnetic force acting on levitation and guidance coils

When a levitation current is induced in LG coils, the reaction force of the levitation force is applied in the vertical direction, as shown in Fig. 2. In addition, electromagnetic force is applied in the lateral direction, with the upper unit coils being pulled away from the side wall of the guideway and the lower unit coils being pressed against the side wall of the guideway. In particular, the upper unit coils are subjected to an attraction force, and since the load is supported only by bolts at fastening points, the stress is concentrated near the fastening points [4]. On the other hand, the repulsive force acting on the lower unit coils can be supported by the back of the molding coil. Therefore, in the actual evaluation of the vibration characteristics of the LG coils, it is necessary to simulate the attraction force acting on the upper unit coils.

2.3 Circuit configuration of LG coils

In an actual LG coil, the upper unit coil and the lower unit coil are connected in parallel. When energized externally, the guidance current flows in the same direction in the upper unit and lower unit coils. Therefore, with the current circuit configuration of test coil, it is impossible to simulate levitation current in which the current flows in the opposite direction in the upper unit and lower unit coils. Therefore, the upper unit coil to which the pull-off force is applied was chosen as the evaluation target. Test conditions and circuit configuration based on numerical analysis were studied to apply the necessary electromagnetic force to the upper unit coil.

3. Examination of test conditions based on numerical analysis

To realize an electromagnetic excitation test on an actual LG coil, it is necessary to reproduce the electromagnetic force acting on the test coil in the lateral direction relative to the upper unit coil. The test conditions under which an actual LG coil is subjected to a load equivalent to the electromagnetic force at 500 km/h were examined. The electromagnetic force and stress were calculated for the case where only the upper unit coil was energized and the case where only the lower unit coil was energized by changing the circuit configuration for the energizing condition of the LG coil. Calculations were also made for the case where the test coils (upper and lower dissimilar poles) were energized with the levitation current. Based on the results, methods to enhance the electromagnetic force were discussed.

3.1 Stress prediction in equilibrium displacement

(1) Electromagnetic field analysis

The analytical model for electromagnetic field analysis is shown in Fig. 3. Only the conductor section of the LG coil and the superconducting coil were modeled. The LG coil and the superconducting coil were calculated using a 1/2 symmetry model with zero displacement in the direction of travel. Energizing conditions were 250 A (700 kA magnetomotive force) for the superconducting coil and 2000 A for the LG coil. The vertical displacement was calculated as 43.9 mm (equilibrium displacement at 500 km/h). The electromagnetic force acting on the LG coil is shown in Fig. 4. The direction of the coil windings (current) is different for the upper unit and lower unit coils. Therefore, looking at the load in the lateral direction, the upper unit coil has an attractive force (negative) and the lower unit coil has a repulsive force (positive). The load of the test coil (upper and lower different poles) is the sum of the loads of the upper unit and lower unit coils.

(2) Structural analysis

In the structural analysis, the stress distribution was predicted by setting the electromagnetic force obtained from the electromagnetic field analysis to each unit coil. The structural analysis model of the LG coils is shown in Fig. 5. In this analysis, not only the coil conductor, but also the molding resin, the support structure on the back, and the fastening bolts are reproduced. In making a mathematical model the fastening bolts were considered as beam elements and the rest as solid elements, and the friction on the contact surfaces of the fastening parts was also taken into account. The number of elements was about 33,000. In a separate modal analysis, the primary resonance frequency of the LG coil was 240 Hz. In contrast, the excitation frequency in the electromagnetic excitation test was
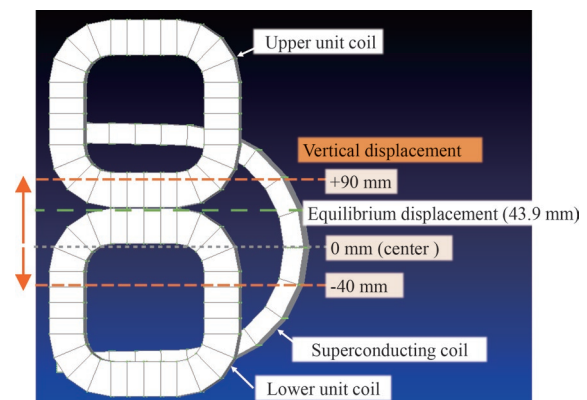
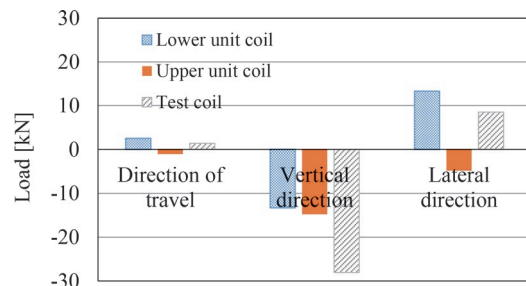**Fig. 3 Analytical model for electromagnetic field analysis**

Fig. 4 Electromagnetic force acting on the LG coil

about 100 Hz, which is sufficiently low, and the amplitude magnification factor is expected to be close to 1. Therefore, the stress distribution predicted by structural analysis is based on static loading. As an example, Fig. 6 shows Mises stress distribution and the deformation shape of the test coil during electromagnetic excitation simulating levitation force. The displacement is shown enlarged. The deformation shape of the upper unit coil is bulging in the direction of the center of the track where the attractive force acts. The deformed shape of the lower unit coil is pushed toward the guideway by the repulsive force from the SCM. Next, stress concentration occurs around the bolt fastening area, and Mises stress is very small in other locations, such as around the unit coil. The maximum Mises stresses for each condition were: upper unit coil 19 MPa, lower unit coil 15 MPa, and test coil 25 MPa. Comparing the maximum Mises stress of the upper unit and lower unit coils, the stress of the upper

unit coil is larger. This is considered to be due to the support structure. This is because the lower unit coil supports the load pressed against it by the back of the coil, while the upper unit coil supports the load pulled off by the bolt heads at the fastening points alone. However, the target electromagnetic force was not reached. In order to reproduce the load equivalent to the electromagnetic force at 500 km/h in the test coil with the upper unit coil as the evaluation target, it is necessary to enhance the electromagnetic force by changing the test conditions.

3.2 Enhancement of electromagnetic force

Only the upper unit coil was subjected to evaluation. Then, the test conditions to provide the load equivalent to the electromagnetic excitation test in the test coil were studied. As shown in Fig. 3, trials were conducted to enhance the electromagnetic force by adjusting the distance between the upper and lower side of the SCM and the upper and lower side of the upper unit coil. Figure 7 shows the electromagnetic force acting on the upper unit coil when the vertical displacement is varied from -40 mm to +90 mm. While the electromagnetic force in the direction of travel and the vertical direction is almost constant, only the lateral electromagnetic force changes in proportion to the vertical displacement. In Fig. 7, the green line shows the equilibrium displacement (43.9 mm) and the red line shows the limit of the test apparatus (-20 mm). If the vertical displacement is reduced to -20 mm, an electromagnetic force of more than 10 kN will be applied in the direction of attraction. Compared to the case of the equilibrium displacement, more than twice the electromagnetic force can be applied. A comparison of the maximum Mises stress in the lateral direction obtained from the structural analysis is shown in Fig. 8. The maximum Mises stress in the upper unit coil was about 25 MPa when the vertical displacement was set to -20 mm. This result is almost equal to the target stress. As for the deformed shape of the LG coil, although the lower unit coil is not vibrated, the stress concentration at the bolted joints is reproduced. From the above, it is considered that the method of energizing only the upper unit coil and setting the vertical displacement to -20 mm is effective as the test condition to apply the load equivalent to the electromagnetic force at 500 km/h to the actual LG coil.
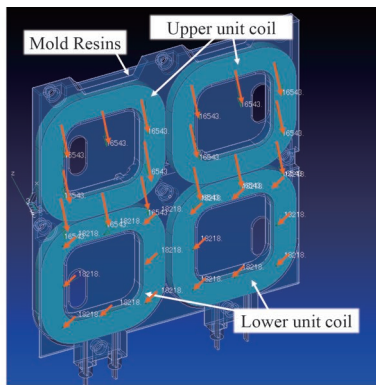
(a) Electromagnetic field analysis model of LG coil and electromagnetic force setting
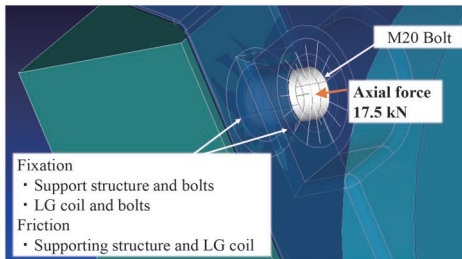
(b) Bolt fastening area

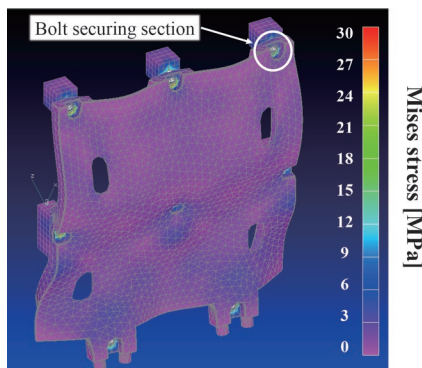**Fig. 5   Structural analysis model of the LG coil**

Fig. 6   Mises stress distribution and deformation shape during electromagnetic excitation
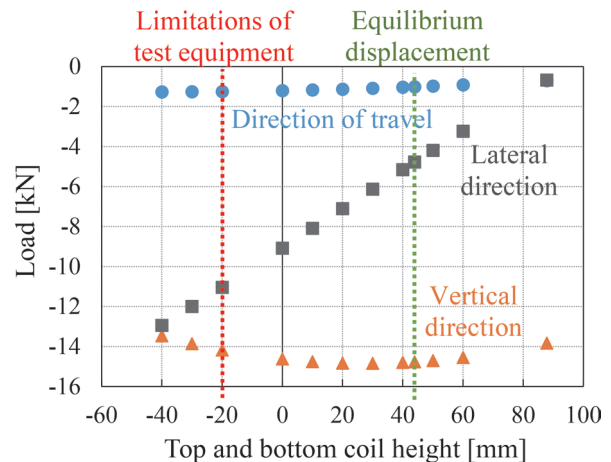

Fig. 7   Electromagnetic force acting on the upper unit coil

4. Machining method for circuit modification

In this test, only the upper unit coils are subject to vibration. A method for changing the circuits to energize only the unit coils which are for evaluation was investigated. Figure 9 shows the machining method for changing the circuits. The circuits were cut by machining a portion of the lower unit coil conductors. A disk grinder was used for machining. Resistance was measured with a milliohm high tester to confirm a disconnection of the circuits. The cutting points by the disk grinder may cause the short-circuit of the conductors during vibration or may have reduced mechanical strength. Therefore, epoxy resin was filled in the slit on the cut areas to provide insulation and reinforcement. The LG coils with the circuit modified by machining were energized through the cable connection terminals. As a result, it was confirmed using a thermal camera that no current flowed in the lower unit coils and only the upper unit coils were energized (Fig. 10). No abnormalities such as localized heat generation due to machining were observed.

5. Electromagnetic excitation tests of LG coil

Electromagnetic excitation tests were carried out on the upper unit coil of the LG coil only, applying a load equivalent to the electromagnetic force at a running speed of 500 km/h.

5.1 Electromagnetic excitation tests methods

Figure 11 shows the test configuration. Figure 12 shows the appearance of the LG coils. The specimens were the LG coils that
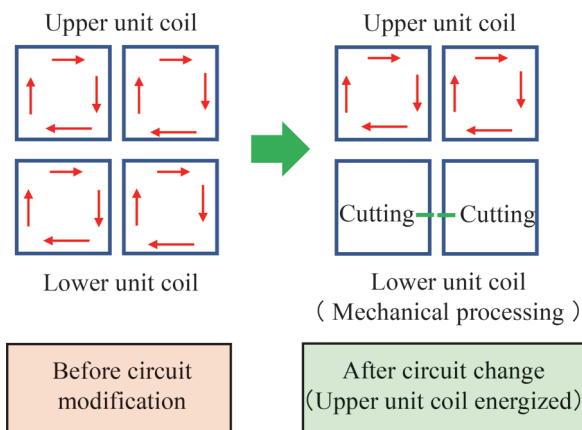
were machined, as described above. The vertical displacement was adjusted in height with the ground coil mounting frame. As shown in Fig. 13, two patterns were used: 43.9 mm (equilibrium displacement) and -20 mm (enhanced electromagnetic force). The SCM [5] was DC excited with a magnetomotive force of 700 kA. The excitation frequency of the Lg coil was set to 100 Hz, and 990 A DC current and 990 A AC current (100 Hz) were energized in the upper unit coil.

5.2 Test result

Figure 14 shows the vibration waveforms of the LG coil observed in the electromagnetic excitation. Figure 12(b) shows the
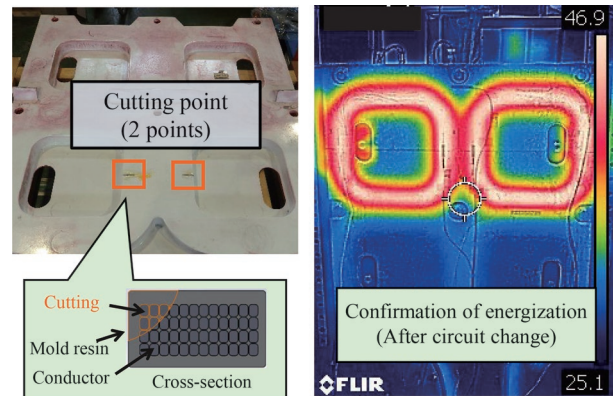

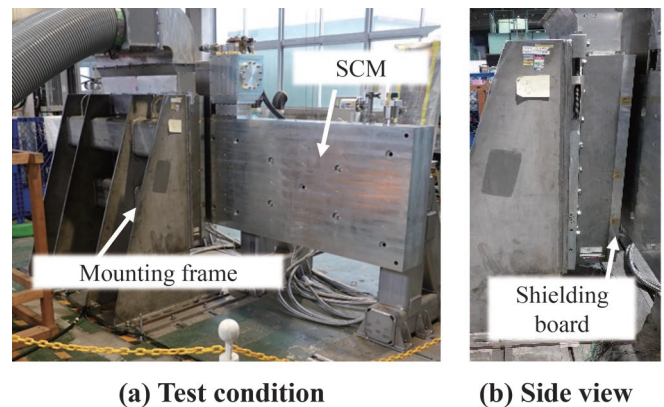**Fig. 10 Confirmation of energization (after circuit change)**

Fig. 8 Mises stress distribution and deformation shape during electromagnetic excitation

(a) Test condition   **(b) Side view**

Fig. 11 Electromagnetic excitation tests configuration

Fig. 9 Machining method for changing the circuit

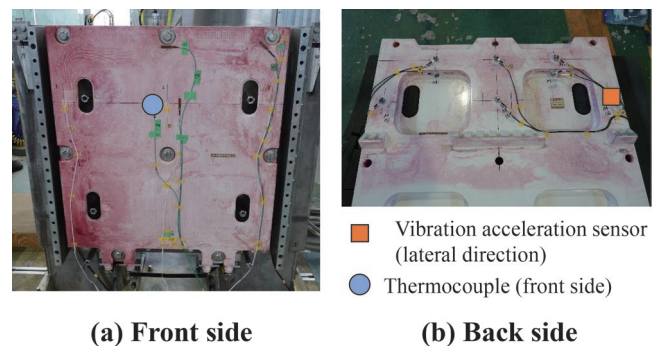**(a) Front side**   **(b) Back side**
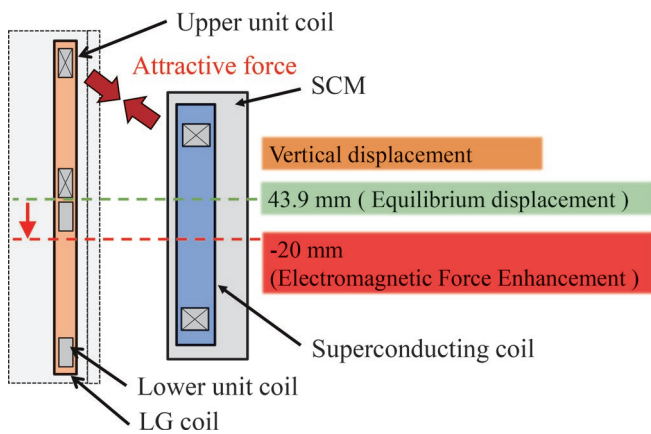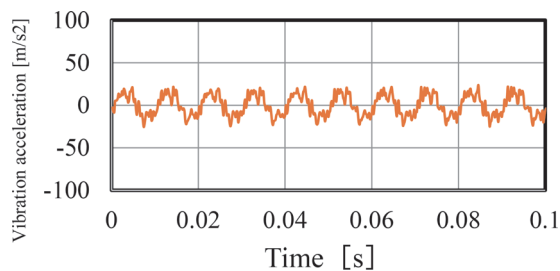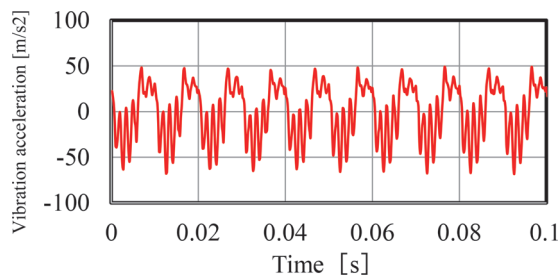
Fig. 12 Appearance of the LG coil

Fig. 13 Height adjustment of vertical displacement (cross-sectional view)

(a) Vertical displacement 43.9 mm (equilibrium displacement)

(b) Vertical displacement -20 mm (electromagnetically enhanced)

Fig. 14 Vibration waveform of electromagnetic excitation test (lateral direction)

installation positions of the vibration accelerometer (position to check the lateral excitation force). It was confirmed that vibratory force was applied to the upper unit coil at both installation positions. Figure 15 shows the comparison of amplitude values of the fundamental wave component of vibration acceleration. The amplitude of vibration acceleration for a vertical displacement of 43.9 mm (balanced displacement) was about 20 m/s². In contrast, a vertical displacement of -20 mm (enhanced electromagnetic force) resulted in an amplitude of 35 m/s². The change in mounting position increased the vibration acceleration by a factor of about 1.7. These results confirmed that the electromagnetic force is enlarged.
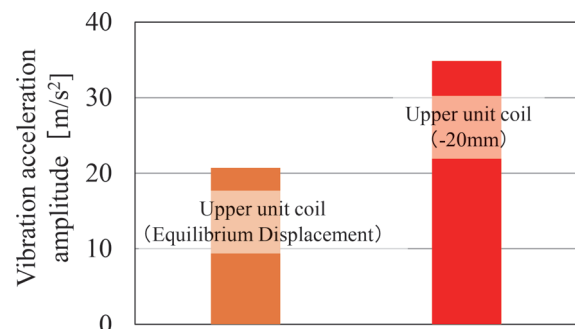

Fig. 15 Comparison of amplitude values of fundamental wave component of vibration acceleration

6. Vibration characteristic evaluation by electromagnetic excitation test

Electromagnetic excitation tests were carried out to evaluate the vibration characteristics of the LG coil which was machined so that only the upper unit coil was energized.

6.1 Test conditions

Vertical displacement was set to -20 mm (enhanced electromagnetic force). The magnitude of the energizing current was the same as in Section 5.1. The current flow energization pattern was decided considering the temperature rise of the coil. The cycle consisted of 6 seconds of energization and 294 seconds of pause within 300 seconds. This cycle was performed for 130 sets. The total number of excitation cycles was 78,000. During the electromagnetic excitation test, data on vibration acceleration and temperature at the positions shown in Fig. 12(b) were obtained.

6.2 Test results

Changes over time of the amplitude values of the fundamental wave component were checked for the acquired vibration waveforms. Figure 16 shows the behavior of vibration acceleration and temperature of the LG coil. As shown in Fig. 16(a), the vibration acceleration changed at the start of the test and at the resumption of the test after a pause. Thereafter, it became a constant value. From the temperature data in Fig. 16(b), the change in vibration acceleration is considered to be due to the effect of temperature change caused by energization. Color checks were also carried out before and after the test to confirm the surface condition of the mold resin. No cracks or other abnormalities were detected during this vibration count. These results provide a prospect for evaluating the vibration characteristics of actual LG coils.

7. Conclusions

In order to establish a method for evaluating the remaining life of actual LG coils against vibration, an electromagnetic excitation test was carried out in which an SCM and the LG coil with a circuit configuration modified by machining were placed opposite facing each other, and only the upper unit coil to be evaluated was energized and vibrated. From the numerical analysis and the vibration data obtained, it was confirmed that the electromagnetic force equivalent to 500 km/h travel could be applied to the upper unit coil by adjusting the vertical position of the SCM and the LG coil. Pros-
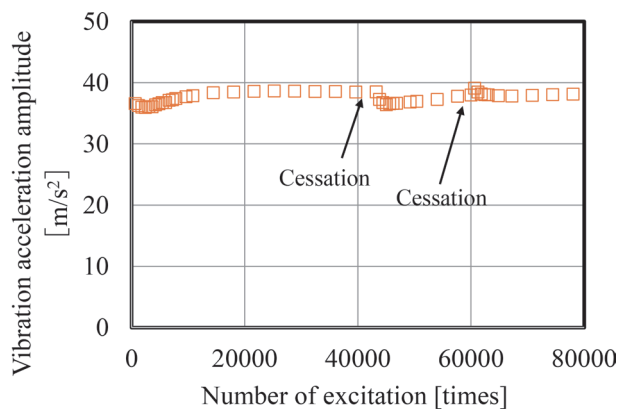
(a) Vibration acceleration amplitude
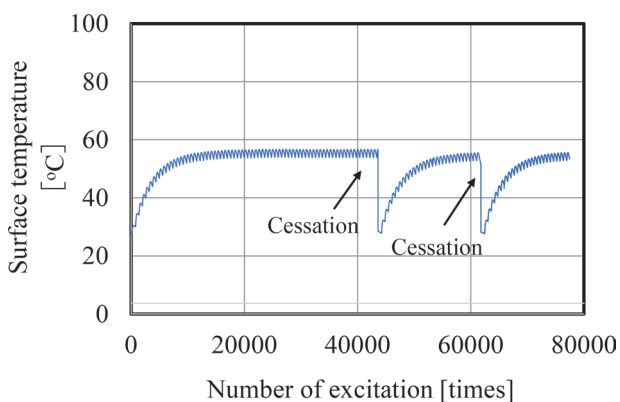
(b) Temperature

Fig. 16   Vibration Characteristic Evaluation

pects were obtained of being able to evaluate the vibration characteristics. Future plans are to conduct a long-term electromagnetic excitation test to evaluate the remaining service life of LG coils against vibration.

References

[1] Fujimoto, T., Aiba, M., et al., "Maglev Technology. Characteristics of Electromagnetic Force of Ground Coil for Levitation and Guidance at the Yamanashi Maglev Test Line," *RTRI Report*, Vol. 13, No. 9, pp. 15-18, 1999 (in Japanese).

[2] Aiba, M., Murai, T., et al., "The Electromagnetic Vibration Test of a Ground Coil by Using the Magnetic Field of Superconducting Magnets," *RTRI Report*, Vol. 14, No. 11, pp. 33-38, 2000 (in Japanese).

[3] Tanaka, M., Aiba, M., et al., "The Electromagnetic Vibration Test of a Ground Coil by Using the Magnetic Field of Superconducting Magnets," *RTRI Report*, Vol. 20, No. 8, pp. 17-22, 2006 (in Japanese).

[4] Matsue, H., Aiba, M., et al., "Stress Evaluation on the PLG Ground Coil with FRP Fastening Devices," *RTRI Report*, Vol. 22, No. 11, pp. 17-22, 2008 (in Japanese).

[5] Mizuno, K., Tanaka, M., et al., "Electromagnetic Vibration Test of a Ground Coil Using a REBCO Magnet," *RTRI Report*, Vol. 34, No. 11, pp. 5-10, 2020 (in Japanese).

Authors

Ryohei IKEDA
Assistant Senior Chief Researcher, Magnetic Levitation Laboratory, Maglev Systems Technology Division
Research Areas: Ground Coils of Maglev

Minoru TANAKA, Dr. Eng.
Senior Chief Researcher, Head of Magnetic Levitation Laboratory, Maglev Systems Technology Division
Research Areas: Ground Coils of Maglev

Katsutoshi MIZUNO, Dr. Eng.
Cryogenic Systems Laboratory, Maglev Systems Technology Division (Former)
Research Areas: Superconducting Magnet

Wireless Power Transfer System for Railway Vehicles with Improved Power Density of Onboard Coil

Hiroshi YODA
Magnetic Levitation Laboratory, Maglev Systems Technology Division

Keigo UKITA
Electrical Machines Laboratory, Maglev Systems Technology Division

To enhance the flexibility of installation of wireless power transfer (WPT) system on railway vehicles, we modified the WPT system to increase the power per unit opposing area of ground and onboard coil up to 150 kW/m² by setting the mechanical gap between coils at 150-mm. In this paper, we describe the design of the improved WPT system capable of collecting 150 kW with a single onboard coil and the results of bench test using a reduced model to verify the system.

1. Introduction

Wireless power transfer (WPT) technology is widely used in small-capacity products such as Qi for charging smartphones and electric toothbrushes. In recent years, international standards are being geared to promote the use of WPT as a charging device for electric vehicles as an application for larger capacity. In the past decade, basic demonstration tests have been conducted in Europe and Korea aiming to apply this technology to conventional railways [1]. Over the same period, in Europe, the EU project Shift2Rail [2] focused on integrating innovative technologies into the railways has also been working in this area. In 2014, we developed a 50 kW-class prototype system and demonstrated power transfer from ground coils installed between rails to on-board coil mounted under a vehicle floor. In this paper, we show the results of design verification and performance evaluation through testing of a modified design system to improve the ease of installing the onboard coils following the basic concept of the prototype system.

2. WPT System for Railway Vehicles

2.1 Inductive type WPT technology

Our system uses induction-type WPT technology. As shown in Fig. 1, this technology can be thought of as a general transformer with a separate iron core, allowing the primary and secondary sides to move freely with respect to each other. Transformers transmit power by magnetic flux between the primary and secondary windings, and the iron core is used to form the path of the magnetic flux and to ensure that the windings are chained to each other. Even if the iron cores are apart, power can be transferred through the gap between the iron cores. However, the magnetic flux that chains the primary and secondary windings, which contributes to magnetic coupling, decreases as the gap between the primary and secondary windings is expanded, resulting in a significant decrease in induced electromotive force. To achieve sufficient power transmission, it is necessary to increase the excitation frequency. In addition, the magnetic flux that does not contribute to the coupling, spreads to the surroundings, resulting in a large reactive power. Therefore, a technique is commonly used, in which capacitors are inserted in the circuit and operated at the LC resonant frequency to adjust the input
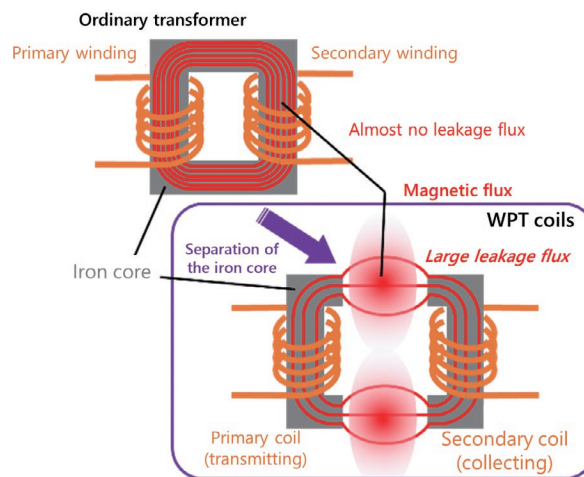

Fig. 1   Principle of inductive-type WPT technology

power factor to unity, thereby minimizing the apparent capacity of the power supply.

In order to transmit high-frequency currents efficiently, we use Litz cable that is stranded cable made by bundling many ultra-fine enameled wires.

When the high-frequency magnetic flux spreading from the coil to the surrounding area chains across the conductor, eddy currents are generated and losses occur. In particular, ferromagnetic materials such as iron used for rails and rolling stock have a strong skin effect, and eddy currents are concentrated in a very shallow area on conductor surfaces, resulting in large losses. Suppression of this loss is one of challenges when WPT is applied to railways where rails exist in the vicinity of the ground coils.

2.2 Configuration of WPT system for railway vehicles

Figure 2 shows an outline of the overall configuration of the WPT system for railways. The system consists of a figure-eight shaped ground feed coil made of Litz cable laid between the rails, and an onboard power collection coil made of Litz cable winding also in a figure-eight shaped, which face each other. The ground coil has a simple, no-core configuration consisting of only one cable strand to reduce the installation cost for long distance installation.
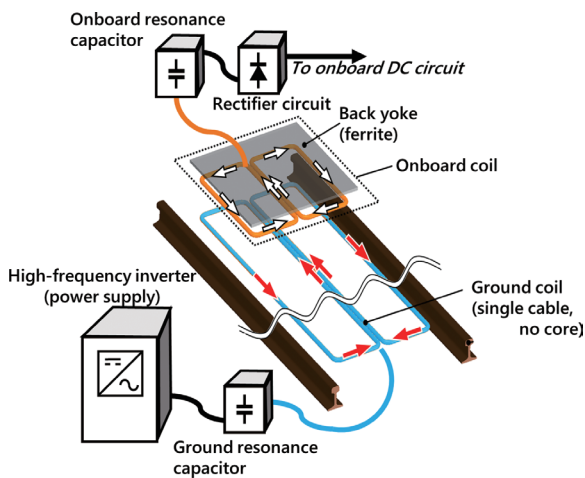
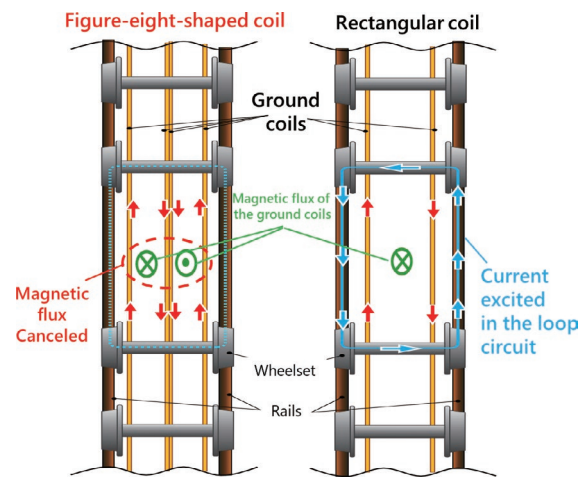**Fig. 2 Overall configuration of the WPT system for railways**

Fig. 3 Superiority of the figure-eight-shaped ground coils in wheel/rail system
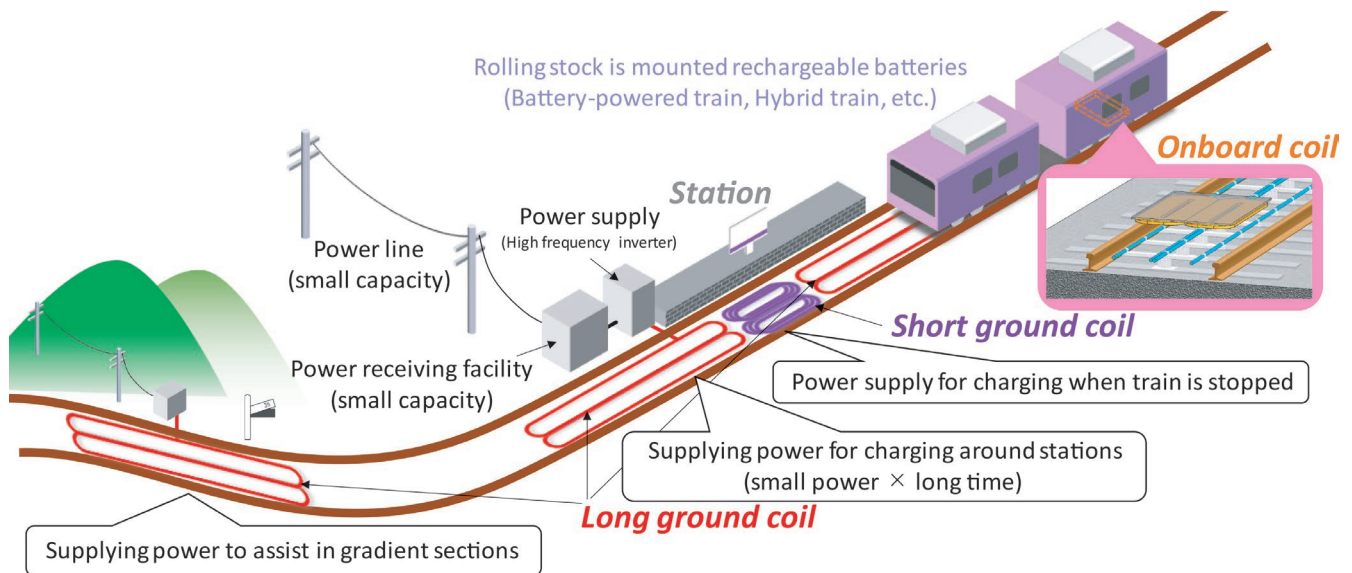

Fig. 4 Concept of a railway application of the WPT system

The figure-eight shaped shape of the coil has an important meaning in its application to railways. When ground coils are installed between rails, as shown in Fig. 3, if they would be simple rectangular coils, they would induce currents in the loop circuit, causing large loss.

On the other hand, in the figure-eight shaped configuration, the magnetic fluxes generated by the left and right coils cancel each other, so, ideally, no current is generated in the loop circuit and no loss occurs. In addition, rail loss due to the interlinkage magnetic fluxes can also be reduced because the strong magnetic field is in the center of the track.

2.3 Application of the WPT system

The WPT system has three features as follows compared to standard catenary systems or third rail systems. Feature 1: the maintenances are reduced because of no abrasion. Feature 2: there is no exposure of electric charging parts. This feature not only improves safety but also eliminates the possibility of accidents caused by fly-

ing objects, and so on. Feature 3: It can be seamless power suppling without mechanical operation, regardless of whether the train is stopping or running.

In recent years, battery-powered trains, hybrid diesel trains, and other vehicles equipped with batteries for running have been introduced one after another. In particular, battery-powered trains introduced in Japan are equipped with pantographs to charge batteries while running on electrified sections or while stopping at electrified turnaround stations. In this type of operation, a large-capacity battery is installed in order to run some distance and to be prepared for long stops in case of an anomalous operation. On the other hand, for example, if frequent small capacity recharging can be performed enroute, the battery capacity consumed by running can be recharged immediately. Furthermore, the battery can be recharged at a nearby recharging facility even when the train is stopped for a long time in case of anomalous operations, thus reducing the amount of battery onboard. Moreover, compared to charging only at turnaround stations, the charging current is smaller, the load on the battery is reduced, which should thereby suppress performance deterioration. In

addition, such recharging facilities can be used to supply power to auxiliary equipment when hybrid vehicles stop for long periods, or to auxiliary power supply in steep sections where the main engine, such as a diesel engine, is running continuously.

Figure 4 shows an image of an application of a WPT system. Since battery-powered trains are expected to be introduced mainly in rural areas, the reduction in maintenance costs resulting from the features 1 and 2 is important. In the case of high-frequency charging by the pantograph system, it may be necessary to extend the stopping time to ensure that the pantograph is raised and lowered, and to introduce measures to prevent deviation from the charging spot while the pantograph is in the raised position. The WPT system with the feature 3 does not require these measures, and charging can be performed simply by installing ground facilities.

3. Development of the WPT system with improved power density of onboard coil

3.1 Overview of prototype system

The improved design of the WPT system follows the basic configuration of the prototype system [3] manufactured in 2014 and aims to improve performance. In the prototype system, the onboard coil was designed for a low-voltage range, and the system was capable of the maximum transfer power of 300 kW by using the entire underfloor of a typical 20-m-long conventional railcar as a mounting space for the onboard coils. The higher the frequency, the more compact and lightweight the system can be. However, considering the AC loss, the withstand voltage of the equipment, and the restrictions imposed by Japan's Radio Law, the basic frequency was set at just under 10 kHz. The mechanical gap of the prototype between the ground coil and the onboard coil was set to the minimum value allowed between the construction gauge and the rolling stock gauge. As a result, the onboard coil was made thinner and the onboard resonance capacitor was smaller, and the onboard system was mounted on the bottom of the underfloor equipment box so that the entire space between the bogies was used without interfering with other equipment. Furthermore, adopting modular design allows for easy adjustment of the total transfer power, by adjusting the number of installed unit panels which can collect 16.7 kW of power per unit. Figure 5 shows a power supply test by using the 50 kW-class system that is composed of three onboard coils and a ground coil.

This prototype system and the results of the test demonstrated the applicability of WPT technology to railways. On the other hand, the following points need to be improved for practical uses. One is since the system requires the entire under-floor space, so the vehicle design must be done assuming that the system is installed. The other is that the gap between ground coils and onboard coils is narrow. The gap in the use of commercial vehicles is to be set much larger than 75 mm, therefore the system performance needs to be improved.

3.2 Redesign and system configuration

In this work, by reducing the space occupied by onboard coils, the system was redesigned to increase the transfer power per unit area, namely the transfer power density, up to 150 kW/m², which is three times larger than the transfer power density of the prototype system. At the same time, we aimed to increase the gap between ground coils and onboard coils to 150 mm, which is twice as large as that of the prototype system. The improved system increases the transfer power density, compensating for the performance loss due to the widened gap, while it retains the basic configuration of the prototype system. This means that the improved system needs to meet more stringent requirements in terms of electrical design. Namely, it is necessary to increase the conductor volume of coils and to improve their withstand voltage.

As a result, the size of the resonance capacitor was increased. Consequently, the integrated capacitor and panel configuration was changed to that adopted for the prototype system where the coil and capacitor are separated. The basic structure of onboard coils is epoxy-molded, and the number of windings and the outer diameter of Litz wires are set to allow the configuration of flat winding to increase the amount of conductor while suppressing the voltage. The current density that could be operated under assumed power supply and cooling cycle conditions in actual train operation was also determined by a heat transfer analysis. Based on the process just described the design of the cross-section of coils on board was determined. Next, the length of coils in the longitudinal direction was determined in consideration of its manufacturability as a molded device and its mechanical strength when subject to onboard vibrations. We designed a coil that can collect power with a rated current of 600 A and 150 kW in a single panel. Table 1 shows the specifications of the improved system and the prototype system. Here, the coil effective area is defined as the rectangular area created by the centerline of a winding with its width. Figure 6 shows the designed onboard coil.
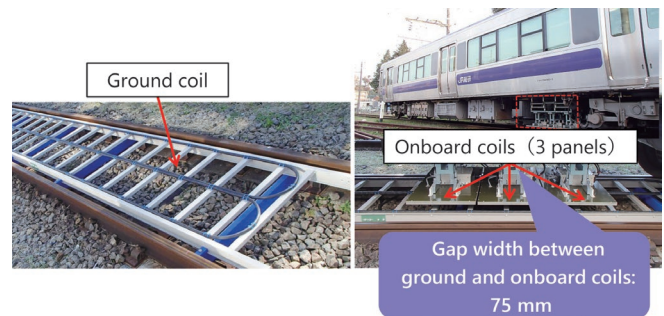

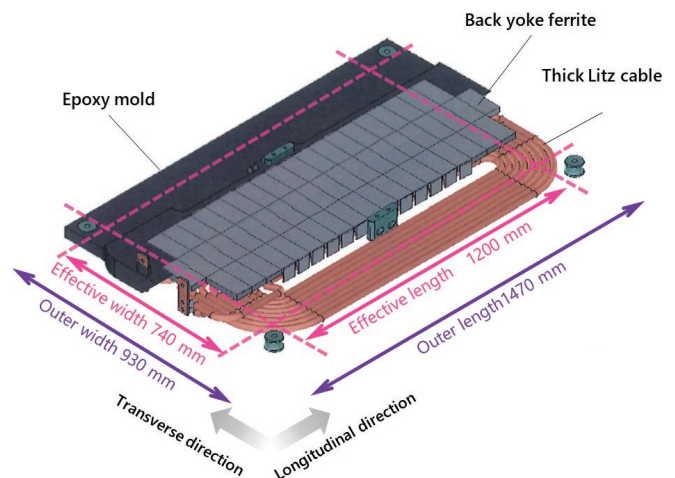**Fig. 5　50 kW-class prototype system**

Fig. 6　Improved 150 kW-class onboard coil design

4. Performance evaluation by scaled-down prototyping and testing

4.1 Overview of the improved system and prototyping

4.1.1 Ground coil

The ground coil was constructed using a high voltage Litz cable with a conductor volume of 100 mm². This cable has the structure of a typical 6.6 kV rated rubber insulating cable but omits the shield layer to avoid generating induced voltage. Figure 7 shows the ground coil laid on the test track.

4.1.2 Onboard coil and onboard resonance capacitor

Since a 50 kW-class high-frequency inverter is used to supply power for the test, the designed 150 kW-class onboard coil is not suitable for the test under rated conditions. Therefore, we made an onboard coil for the test, keeping the basic structure of the 150 kW-class coil but reducing the size to 50 kW by shortening the center section in the longitudinal direction as shown in Fig. 8.

Figure 9 shows the high-voltage molded capacitor made for the test. Two of these were connected in parallel to the onboard coil.

4.2 Thermal load test of the onboard coil

To confirm the temperature rise of the onboard coil in actual train operation, thermal load tests were carried out under cooling conditions created by the running wind in actual use which were taken into account for the design. Figure 10 shows the test environment, wind velocity distribution, and surface temperature measurement points. Cooling with a blower in this test is considered to be equivalent to a running wind of about 40 km/h based on the wind velocity. Figure 11 shows the energization cycle and cooling conditions during the test. The cycle was repeated with the WPT system charging at each station, energizing at 600 A for 90 seconds (assuming charging during station stops and low-speed sections) and standing by for 210 seconds (assuming running between stations).

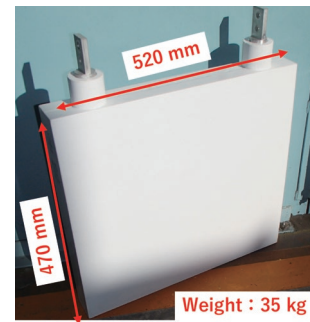Figure 12 shows the temperature measurement results at each

Fig. 7   Ground coil for testing

Fig. 8   50 kW-class onboard coil for testing

Fig. 9   Onboard capacitor for testing

Table 1   Specifications of the improved system and the prototype system

		Prototype system	Improved system
Frequency [kHz]		< 10.0	
Ground coil	**Transverse width [m]**	0.8	0.7
	Cross-section of the conductor [mm²]	80	100
	Excitation current [A$_{rms}$]	400	500
The mechanical gap width between coils [mm]		75	150
Onboard coil (1 unit)	**Rated Transfer power [kW]**	16.7	150
	Effective area of coil [m²]	0.32	0.89
	Transfer power density [kW/m²]	52.2	168.5
	Number of turns	4	8
	Cross-section of the conductor [mm²]	30	82.4
	Rated current [A$_{rms}$]	160	600
	Coil terminal voltage [V$_{rms}$]	440	7850
Onboard output configuration [V$_{dc}$·A$_{dc}$]		600·27.8	250·600

Fig. 10   Thermal load test of the onboard coil

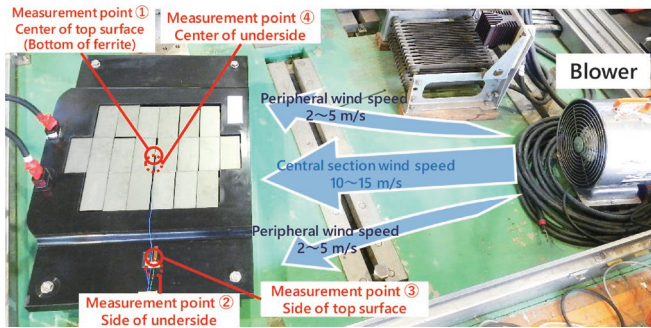Fig. 11   Energization cycle and cooling conditions

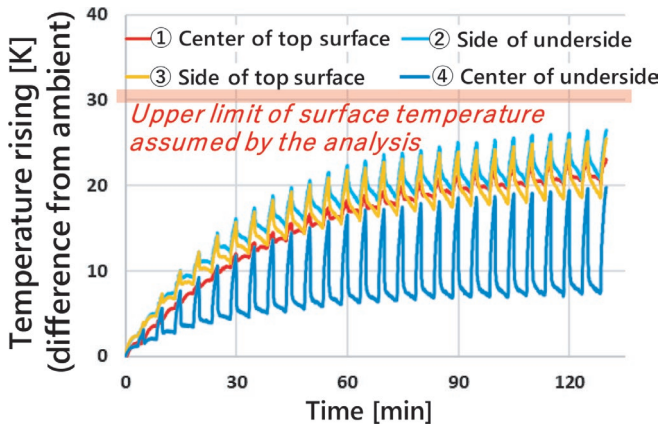Fig. 13   Results of heat transfer analysis

Fig. 12   Measurement of temperature rise in onboard coil

surface point. The results of heat transfer analysis considered at the time of design, as shown in Fig. 13, show that when the temperature rise of inside mold resin saturates about 60 K the surface temperature rise is suppressed less than 30 K. This temperature rising of inside mold resin corresponds to a rise to 100℃, which is the allowable temperature of mold resin, from an initial temperature of 40℃. From above two results, it is confirmed that the inside of the mold resin will tolerate the maximum temperature rise. Therefore, we conclude that the thermal design of the onboard coil is appropriate.

4.3 Bench Test I: Power transfer test with long ground coil and body-mounted onboard coil

To verify the validity of the design using electromagnetic field analysis, a power transfer test was carried out with a test car installed the onboard coil under the floor. The car is placed on our testing track with the ground coil laid as shown in Fig. 7. Figure 14 shows the test conditions and Table 2 shows the test results. Table 2

shows that the measured and analyzed values agreed well under the test conditions, and it was confirmed that the electromagnetic field analysis for the onboard coil design was sufficiently accurate.

4.4 Bench Test II: Power transfer test with multi-turn short ground coil

This system assumes use of long ground coils for power supply during train running. This requires the structure of the ground coils should be simple, which is one of the reasons for difficulties to improve power transfer efficiency. On the other hand, if power is fed only when trains are stopped, the length of the ground coils can be minimized, and more conductors can be used with the reduced current density and losses, which can achieve more efficient power transfer. As shown in Fig. 15, this test was conducted with a 3-turn short ground coil and an onboard coil facing each other at a separation of 150 mm. Table 3 shows the measured power transfer efficiency at maximum power output. In this test, we demonstrated power transfer with inter-coil power transfer efficiency of over 90%, which is higher when compared to 86% in the test using the long ground coil described above, at transfer power density of 150 kW/m².

5. Summary

The wireless power supply system for railway vehicles is simple power supply facilities that can be used while trains are running or stopping, and it can reduce the number of onboard batteries of

Table 2   Actual measurements of bench test I and results of the simulation

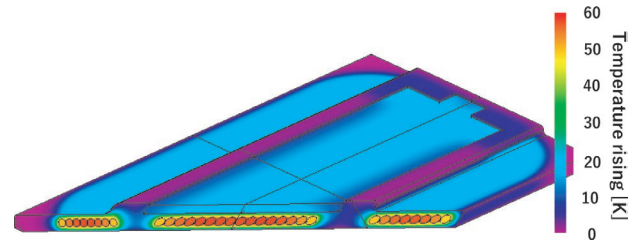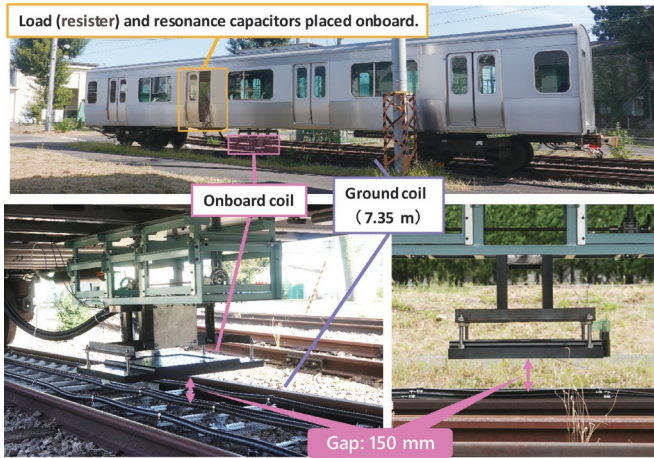|			Measurements of bench test I	Simulation of the testing condition
Ground circuit		Frequency [kHz]	9.5	← (input)
		Current [A$_{rms}$]	559	← (input)
Onboard circuit		Coil terminal Voltage [V$_{rms}$]	2157	2043
		Current [A$_{rms}$]	481	← (input)
		Collection power of the coil [kW]	35.5	35.2
The efficiency between coil-to-coil [%]			86.6	85.7

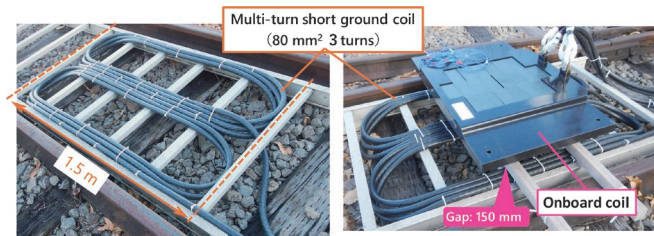**Fig. 14 Bench test I (with long ground coil)**

Fig. 15 Bench test II (with short ground coil)

battery-powered trains by frequently recharging the batteries. In this work, we aimed to reduce the space occupied by the onboard coil and increase the gap between the ground and onboard coils, addressing issues which remained to be solved after the previous development of a prototype system. We redesigned and manufactured a 150 kW-class onboard coil for the modified design system that can increase the power transfer density to more than 150 kW/m², which is three times that of the prototype system, and expanded the gap to 150 mm, which is twice that of the prototype system. The validity of this design was verified by using a test coil that was scaled down to 50 kW-class and fabricated without changing the basic structure of 150 kW-class coil. As a result, the validity of the electrical and thermal design was confirmed. Note that, in order to put the designed

Table 3 Results of bench test II

Frequency [kHz]		9.93
Ground circuit	Coil terminal voltage [V_{rms}]	338.6
	Current [A_{rms}]	1003
Onboard circuit	Coil terminal voltage [V_{rms}]	1002
	Current [A_{rms}]	285.1
	Collection power of the coil [kW]	49.4
Transfer power density [kW/m²]		155.2
The efficiency between coil-to-coil [%]		92.0

coil into practical use, it is necessary that the coil should have a higher withstand voltage and long-term durability in high-frequency excitation. In addition, in a power feed test using the short multi-turn ground coil specially designed for high-efficiency power feed while the train is stopping, power transfer at the target transfer power density was demonstrated with an inter-coil efficiency of more than 90%.

References

[1] Liming Shi, Zhenggang Yin, Longbin Jiang, Yaohua Li, "Advances in inductively coupled power transfer technology for rail transit," *CES Transactions on Electrical Machines and Systems*, Vol. 1, No. 4, pp. 383-396, 2017.

[2] https://rail-research.europa.eu/about-shift2rail/

[3] Ukita, K., Kashiwagi, T., Sakamoto, Y., Kato, Y., "Power Transmission Performance Verification of a Non-contact Power Supply System for Railway Vehicles," *Quarterly Report of RTRI*, Vol. 57, No. 3, pp. 228-233, 2016.

Authors

Hiroshi YODA
Associate Senior Researcher, Magnetic Levitation Laboratory, Maglev Systems Technology Division
Research Areas: Wireless Power Transfer, Numerical Analysis, Maglev Systems

Keigo UKITA
Associate Senior Researcher, Electrical Machines Laboratory, Maglev Systems Technology Division
Research Areas: Electric Machines, Electromagnetic Applications

Summaries of Papers in RTRI REPORT (in Japanese)

R&D Activities and Future Perspectives in Material Technology
Motohide MATSUI
(Vol.36, No.11, 1-4, 2022.11)

Various kinds of materials are used as components of systems not only in railways but also in other industrial fields. So far, advances in material technology for structural and functional materials have contributed greatly to the development of railways. Current R&D activities mostly focus on materials with longer service life, the clarification of material deterioration mechanisms and so on. However, the pandemic of COVID-19 and rapid changes in the environment with climate change will have a significant impact on future railways. It is necessary that material technology will adapt to this drastic transition in order to keep contributing to the sustainable development of railways.

Development of Plastering Geopolymer Mortar
Motoki UEHARA, Takatsune SATO
(Vol.36, No.11, 5-10, 2022.11)

Geopolymer (GP), which does not use Portland cement, has been attracting attention as a new repair material because of its high CO_2 reduction and acid resistance. However, its poor plastering workability has been a issue to be developed for its practical use. Therefore, we developed a prototype GP mortar for plastering work using fly ash and blast furnace slag fine powder without glass water by the original method named "Si component powder addition in-situ dissolution method." As a result, the developed GP mortar showed good workability, high resistance to acid deterioration, and no cracking under the condition of an alkali component/water molar ratio of 0.15 and a Si component/alkali component molar ratio of 0.20. Judging from these results, the developed GP mortar is feasible for practical purposes.

Evaluation Method for Water Penetration Resistance of Concrete Structures Applicable to Horizontal Surface
Sohei NISHIO
(Vol.36, No.11, 11-16, 2022.11)

High durability is required for railway structures constructed on the premise of long-term service as social infrastructure. Technological development that leads to longer life of structures is becoming more important in terms of contributing to decarbonization. A method called WIST (Water Intentional Spraying Test) developed by the author of this paper is becoming widespread as a non-destructive test method that can easily evaluate water penetration resistance that affects the durability of reinforced concrete structures. However, due to the principle of measurement, the application of the WIST was limited to vertical planes. This paper reports a new measurement method developed for applying the WIST to horizontal planes. The new method can be implemented just as easily as the conventional WIST with the same equipment.

Method for Improving Corrosion Protection by Paint Coating over Metal Layer with Plating and Thermal Spraying Materials on Steel Bridges
Tatsuro SAKAMOTO
(Vol.36, No.11, 17-22, 2022.11)

Steel bridges are generally coated to control the progression of corrosion. Since the corrosion resistance of paint coating tends to decrease with age, a method has been proposed in which a metal coating such as plating or thermal spraying is used as a base coat and then painted over metal coating. However, there are few cases in which the long-term durability of cases using this method has been evaluated. Therefore, in order to understand the long-term durability of combination of various metal coatings and paint coatings, we investigated the deterioration of metal coating under the paint coating on specimens exposed for about 40 years. Furthermore, accelerated degradation tests using newly prepared specimens were conducted to evaluate the long-term durability of metal coating with damage reaching bare metal.

Study of Rail Grinding Amount by Surface Layer Analysis Using X-ray Diffraction
Yoshikazu KANEMATSU, Motohide MATSUI, Naotaka UEHIGASHI
(Vol.36, No.11, 23-28, 2022.11)

Rail grinding is so far carried out by many railway companies because of its effectiveness in suppressing squat. However, few studies have examined the amount of grinding required for rails which have never been grinded before. Hence, using a quantitative evaluation method of material state by diffraction X-ray analysis, the depth of surface layer affected by rolling contact was evaluated for rails with cumulative passing tonnage ranging from 100 to 700 million tons. As a result, it was found that the depth affected by rolling contact tends to increase to 0.5 to 1.5 mm with increase in cumulative passing tonnage

Effects of Segment-structured Carbon Film on Fretting Wear Prevention of Axle Journal Bearings
Yoshiaki OKAMURA, Daisuke SUZUKI, Kazuki IKOMA, Takafumi NAGATOMO
(Vol.36, No.11, 29-35, 2022.11)

In an axle journal bearing of railway vehicles, it is necessary to mitigate the fretting wear that occurs between the contact surfaces of the inner ring and the backing ring. In this work, we investigated the preventive effect of segment-structured carbon film on the fretting wear through rotation tests of full-scale railway axle bearings with the backing ring side face coated with the film. As a result, we have found that the film is effective in suppressing the fretting wear generated on the contact surfaces between the inner ring and the backing ring of the axle bearings.

Improvement of Starting Acceleration by use of Gear Oil with Improved Low-temperature Fluidity
Sadayuki KIKAWA, Junichi SUZUMURA, Kazuki IKOMA
(Vol.36, No.11, 37-42, 2022.11)

This study explores effects of gear oil with improved low-temperature fluidity on improvement of starting acceleration of trains running in cold districts. In starting performance tests at -20℃, temperature rise of gearbox in acceleration region was suppressed using the gear oil with improved low-temperature fluidity. Suppressing effects on temperature rise of gearbox using gear oil with improved low-temperature fluidity was also confirmed under condition where starting acceleration was increased up to 2.9 km/h/s. Accordingly, from these results, it is found that the use of gear oil with improved low-temperature fluidity is effective in improving starting acceleration in cold environment. Moreover, it is confirmed that the use of gear oil with improved low-temperature fluidity tends to suppress gear oil temperature rise under conditions of operation at maximum speed.

Autonomous Damage Detection System for Damage of Axle Bearings of Railway Car Bogies

Shogo MAMADA, Tatsuya OHTA, Masashi MIYAMOTO, Yoshiaki OKAMURA
(Vol.36, No.11, 43-48, 2022.11)

Axle bearings of railway car bogies are important parts that support the running of the cars. It is desirable to detect damage to axle bearings at an early state. Therefore, an autonomous damage detection system (ADDS) was developed that does not require a power supply nor wiring and notifies axle bearing damage to the vehicle after detecting. The ADDS utilized an anti-vibration rubber with a built-in piezoelectric element and wireless transmitter; which was installed on the axle box. The damage detection performance of the ADDS was evaluated using a test machine. In the case of a damaged bearing, the power generated by the piezoelectric element built-in the rubber could drive the radio transmitter, and the damage could be notified.

Trend on Research and Development Relating to Information and Communication Technology in Railway Fields.

Mitsuyoshi FUKUDA
(Vol.36, No.12, 1-5, 2022.12)

In various industrial fields, innovation of systems and improvement of business operations through the use of information and communication technology, or so-called digital technology, have become urgent challenges. In railway industries, decline in the working-age population as well as changes in behavior triggered by the COVID-19 have led to stronger demands than ever before for labor and manpower savings and lower costs. To accomplish these tasks, innovation in railway systems using digital technology is expected. This paper presents recent research and development using digital technology, in terms of data analytics, sensing and recognition, and information networks.

Inspection Method of Track Facilities using Image Analysis of Images in Front of Trains

Nozomi NAGAMINE, Yosuke TSUBOKAWA, Wataru GODA, Riho MAEDA, So KATO, Kensuke ITOI
(Vol.36, No.12, 7-12, 2022.12)

Appropriate maintenance of tracks is vital for the safe operation of railways. Properly managing track facilities is necessary to prevent buckling of rails. Due to social backgrounds of a shortage of workers, a decrease in skilled engineers, and a decrease in passenger income, inspection methods with a low-cost and no need of experience are desired. Therefore, we have developed a method that estimates each image's kilometers, rail gaps, wooden sleeper deterioration, and ballast shape using only inexpensive camcorders. This paper describes the outline of the method and its application results.

Proposal for Transmission Media Usage Functions in Transmission Protocol for Railway System

Satoko RYUO, Akio HADA, Daisuke YAMAGUCHI, Kazuki NAKAMURA, Kunihiro KAWASAKI
(Vol.36, No.12, 13-19, 2022.12)

Currently, information utilized through a railway system is being collected in each section, such as rolling stock section, civil engineering section and electricity section, which makes it difficult to share the information beyond sections. Therefore, in a previous study, we proposed an integrated information network for sharing the information of each section and basic functions of the communication protocol in this network. In this paper, we present details of the transmission media usage function among them. Furthermore, we report the results of a communication verification test using a router implementing the proposed functions.

Evaluation Methods of Measures Against Delay based on Propagation Score and Affected Passengers

Taketoshi KUNIMATSU, Aiko KUNISAKI
(Vol.36, No.12, 21-26, 2022.12)

In recent years, train delay is one of the most serious problems in rail transportations in Japan. Although timetable planners try to improve punctuality by modifying a current timetable, there are no clues as to increase of trains or stations running time/ dwell time supplements should be increased. In this research, we developed an evaluation method of train delay based on its propagation range. We also proposed an evaluation method from the viewpoints of passengers. We applied these methods to the timetable change in existing rail lines and confirmed that the proposed methods can pick up critical trains for which taking measures are effective for improving overall punctuality of the railway lines.

Automatic Calculation Method for Rolling Stock Assignment Considering Splitting and Combining of Train

Satoshi KATO
(Vol.36, No.12, 27-33, 2022.12)

Railway operating companies are required to prepare rolling stock assignment for each timetable revision. In some railway lines, splitting and combining of trains are often used to adjust transportation capacity flexibly. However, these operations are labor-intensive and time-consuming, reduction in the number of splitting and combining is desirable. In this paper, we propose a method for automatically creating rolling stock assignment which reduces the number of splitting and combining of trains using a mathematical optimization technology. Computational experimental results targeting real instances of several railway lines show that the proposed method is effective in terms of evaluation criteria.

Convenience Evaluation of Clock-face Local Railway Timetables

Takamasa SUZUKI, Takuya WATANABE, Daiki OKUDA, Noriko FUKASAWA
(Vol.36, No.12, 35-40, 2022.12)

This article aims to reveal convenience evaluation of clock-face (regular interval) timetable for local railways, which provides periodic train services, we conducted a questionnaire survey to collect data on the evaluation of timetables with varying number of trains or periodicity of train services. Using the collected data, a logistic regression model was constructed to quantify the magnitude of the effect of such characteristics on the convenience evaluation. The results obtained by the regression model revealed that both interval regularity and hour-by-hour cyclicity improve passengers' evaluation. This may lead to improving convenience of local railway lines where additions of train services may be impractical.

Evaluation Method for Implementation Effect of Disaster Countermeasures on a Freight Railway Network

Daiki OKUDA, Takuya WATANABE, Shingo NAKAGAWA, Takamasa SUZUKI, Noriko FUKASAWA
(Vol.36, No.12, 41-46, 2022.12)

We developed a method for evaluating the effectiveness of disaster countermeasure implementation using two indexes: the amount of freight transported during the period when an interrupted section due to a natural disaster exists in the freight railway network, and the costs of restoration work and keeping freight transportation during the period, covered by the operator of the freight railway. The method aims to support decision-making of the operator in planning and examination of disaster countermeasures. A case study applying the developed evaluation method, showed that the

method can provide appropriate evaluation results contributing to the decision-making of the freight railway operator.

Quantification of Relationship between Image of Urban Railway Services and Residential Location Preference

Takuya WATANABE, Noriko FUKASAWA, Daiki OKUDA, Takamasa SUZUKI

Railway operators are endeavoring to improve the people's image of their services in order to gain more residents nearby. However, there are no studies focusing on the relationship between image of railway services and residential location preference in urban areas. In this study, a questionnaire survey on urban railways was conducted. We applied factor analysis to the collected data, and aspects of the image were integrated into four categories. Next, we developed a regression model to quantify the relationship between categories of image aspects and residential location preference. The model enables railway operators to improve residential location preference in terms of image of their services.

Equation for Design Strength of Embedded Part of Square Steel Stopper in Railway Bridge

Shuntaro TODOROKI, Yuki MORI, Toshiya TADOKORO, Ken WATANABE

It is required to improve accuracy of design strength of embedded part of stopper to suppress its damages due to earthquakes, which have been difficult to recovered. Therefore, focusing on effects of arrangements of reinforcing bars placed in an embedded part of square steel stoppers at girder, we performed experiments and analysis. The results showed that the strength can be increased by changing the positional relationship between the stopper and the reinforcing bars without increasing the amount of reinforcing bars. In addition, it was also revealed that we have to consider three types of failure modes when evaluating the strength. Finally, based on the failure mechanism of each of these failures, we proposed an equation for design strength of embedded part of stopper.

Prediction Equation for Shrinkage Strain of Concrete Considering the Effect of Mixed Cement

Ken WATANABE, Mami NAKAMURA, Tetsuya ISHIDA, Tadatomo WATANABE

In order to cope with various design conditions of concrete structures, a prediction equation for the shrinkage strain of concrete has been developed, which allows input of the effects of cement types, aggregate shrinkage strain, and the application of liquid water, in addition to the conventionally indicated mix proportion of concrete and ambient relative humidity. The prediction equation is formulated based on the 3D material-structure interaction analysis system (DuCOM-COM3). The prediction equation can explain the phenomena that appear to be caused in part by concrete shrinkage, such as strain of concrete in prestressed concrete (PC) girders in service using blast furnace cement concrete (Class B).

Effects of Impact Loads from Train Wheel Passing Rail Joints on Fatigue at Deck System of Steel Box Girders

Yusuke KOBAYASHI, Taro INOUE

Impact loads from train wheel passing rail joint tend to cause fatigue cracks in steel girders near rail joint. In order to evaluate the effects of impact load on fatigue at the deck system of a steel box girder, we carried out stress measurements of steel girders at an existing bridge. The result showed that the impact loads at rail joints generates two types of high frequency natural mode vibration ; around 40 Hz, and around 350 Hz. It also showed that those vibrations lead to increasing range and cycle of the stress at welding joints of the deck system.

Influence of Structural Details of Beam-to-column Joint in RC Viaducts on Capacity

Yuki NAKATA, Ken WATANABE, Toshiya TADOKORO

RC beam-to-column joint in a railway viaduct is designed to satisfy structural details. However, when overcrowded reinforcement arrangement measures are taken at joint or high strength rebar is applied to members, a relationship between details of reinforcement arrangement and capacity of joint is required. In this study, we carried out cyclic loading tests and 3D FEM analyses to clarify its relationship. The results show that as the inside radius of bend of longitudinal reinforcement decreases, the capacity of joint decreases because of the reduction of compressive strut width, and that the ties in the joint have little effect on the capacity, even though it increases the deformation performance.

Differences in Critical Wind Speed of Overturning Due to Differences in Aerodynamic Force Coefficient Evaluation Methods

Tatsushi OTOBE, Minoru SUZUKI, Yuhei NOGUCHI, Hiroyuki KANEMOTO, Koji NAKADE, Hiroaki NAKANO

Two methods can be considered for a desk-based safety evaluation of a new type of vehicles in strong winds: one method is based on a list of aerodynamic force coefficients from previous studies, and the other method is based on Computational Fluid Dynamics (CFD). However, the differences between the results of each method and wind tunnel test results are not clear. Therefore, the overturning limit wind speeds calculated from the results of three methods were compared.

ANNUAL INDEX	SUBJECTS	QR of RTRI

February 2023 Vol. 64 No. 1

RTRI's Researchers Commended for Their Contribution to Developing Industrial Standards and for Achievement in IEC/TC9 Activities

Dr. Mitsuru Hosoda won the Award for International Standardization Contributor as one of the Year 2022 Awards for Contribution to Industrial Standardization. Mr. Hiroshi Tanaka was given the IEC (International Electrotechnical Commission) 1906 Award for the Year 2022. The award-giving ceremony was held on October 24 in Tokyo.

Dr. Mitsuru Hosoda

QUARTERLY
REPORT of
RTRI